

UNIVERSITY OF CALIFORNIA
SANTA CRUZ

**SEARCH FOR WW AND WZ RESONANCES IN $\ell\nu qq$ FINAL
STATES IN pp COLLISIONS AT $\sqrt{s} = 13$ TEV WITH THE ATLAS
DETECTOR**

A dissertation submitted in partial satisfaction of the
requirements for the degree of

DOCTOR OF PHILOSOPHY

in

PHYSICS

by

Natasha Woods

December 2019

The Dissertation of Natasha Woods
is approved:

Abraham Seiden, Chair

Mike Hance

Bruce Schumm

Quentin Williams
Vice Provost and Dean of Graduate Studies

Copyright © by
Natasha Woods
2019

Table of Contents

List of Figures	vi
List of Tables	xv
Abstract	xvii
Dedication	xviii
Acknowledgments	xix
I Theoretical Motivation	3
1 The Standard Model of Particle Physics	4
1.1 Introduction	4
1.2 Quantum Field Theory	4
1.3 $U(1)_{EM}$ Local Gauge Invariance	5
1.4 Yang-Mills Gauge Theories	8
1.5 Particles in the Standard Model	9
1.6 Higgs Mechanism	14
1.7 Electroweak Theory	15
1.8 Quantum ChromoDynamics	16
2 Standard Model Successes and Limitations	21
3 New Physics Models with Diboson Resonances	24
3.1 Randall Sundrum Bulk Model	24
3.2 Extended Scalar Sector	26
3.3 Simple Standard Model Extensions	27

II Experimental Setup	30
4 LHC	31
4.1 LHC Layout and Design	33
5 The ATLAS Detector	38
5.1 Coordinate System	40
5.2 Inner Detector	41
5.2.1 Pixel Detector	44
5.2.2 Semiconductor Tracker	44
5.2.3 Transition Radiation Tracker	44
5.3 Calorimeters	46
5.4 Muon Spectrometer	50
5.5 Magnet System	54
5.6 Trigger System	55
III Method	57
6 Dataset and Simulated Samples	58
6.1 Dataset	58
6.2 Simulated Samples	61
7 Objects	62
7.1 Electrons	62
7.2 Muons	63
7.3 Jets	64
7.3.1 Small-R jets	66
7.3.2 Large-R jets	67
7.3.3 Variable Radius jets	70
7.3.4 Jet Flavor Tagging	71
7.4 MET/Neutrinos	71
7.5 Overlap Removal	71
8 Event Selection and Categorization	73
8.1 Pre-selection	73
8.2 Trigger	73
8.3 non-VBF/VBF RNN	75
8.4 Topological Cuts	80
8.5 Selection Acceptance times efficiency for Signal Events	90
8.6 Background Estimate	91
8.6.1 Control Regions	91
8.6.2 Fake Lepton Backgrounds	91

9 Systematic Uncertainties	105
9.1 Experimental Systematics	105
9.2 Theory Systematics	108
10 Statistical Analysis	115
10.1 Likelihood Function Definition	115
10.2 Fit Configuration	116
10.3 Best Fit μ	118
10.4 Discovery Test	119
10.5 Exclusion Limits	120
IV Results	122
11 Statistical Interpretation	123
11.1 Discovery Tests	123
11.2 Systematic Profiling and Correlations	129
11.3 Expected and Measured Yields	130
11.4 Limits	144
V Quark and Gluon Tagging	146
12 Prospects	147
13 n_{trk} Calibration	154
14 Application	160
VI Conclusion	165
15 Conclusions	166
Bibliography	167

List of Figures

1.1	The particles of the Standard Model.	11
1.2	Summary of how Standard Model particles interact with other Standard Model particles.	12
1.3	This figure shows the three dominant QCD interactions. From Ref. [16]	18
1.4	Strength of the U(1), SU(2), and SU(3) gauge couplings as a function of the energy scale of the interaction (Q). From Ref. [11] . . .	19
2.1	A comparison of cross section measurements at $\sqrt{s} = 7, 8, 13$ TeV from ATLAS compared to theoretical measurements. From Ref. [5]	23
3.1	Cartoon of RS Bulk Model	25
4.1	Scaling of cross sections with \sqrt{s} . Natasha: write more here . . .	32
4.2	LHC Layout. Natasha write more	34
4.3	LHC Accelerator. Natasha write more	36
5.1	Big picture layout of ATLAS detector. Natasha: write more . . .	39
5.2	Big picture layout of ATLAS detector. Natasha: write more . . .	39
5.3	A simplified schematic of how different particles interact and are detected within ATLAS.	40
5.4	Layout of ATLAS Inner Detector	42
5.5	Layout of ATLAS ID Barrel System.	43
5.6	Overview of ATLAS electromagnetic and hadronic calorimeters. .	47

5.7	Schematic of ECAL	48
5.8	Schematic of HCAL	49
5.9	Schematic of Muon Spectrometer [cite G35]	52
5.10	Schematic of MDT chamber. [cite G35]	53
5.11	Schematic of RPC chamber, which is used for triggering in the central region of the detector [cite G35].	53
5.12	Schematic of TGC chamber, which is used for triggering in the muon end-cap region. [cite G35]	54
5.13	Layout of ATLAS magnet systems.	55
6.1	Integrated luminosity for data collected from ATLAS from 2011 - 2018	59
6.2	Mean number of interactions per crossing for data collected from ATLAS from 2011 - 2018	60
7.1	This figure shows the breakdown of the muon reconstruction efficiency scale factor measured in $Z \rightarrow \mu\mu$ as a function of p_T [4].	64
7.2	[7] This diagram shows the calibration stages for EM jets.	66
7.3	The upper cut on D_2 (a) and jet mass window cut i.e. the upper and lower boundary of the mass (b) of the W -tagger as a function of jet p_T . Corresponding values for Z -tagger are shown in (c) and (d). The optimal cut values for maximum significance are shown as solid markers and the fitted function as solid lines. Working points from $VV \rightarrow JJ$ [ATLAS-HDBS-2018-31-002] is also shown as dashed lines as a reference. Natasha reword?	69
7.4	Natasha write caption	70
8.1	RNN architecture. Natasha add caption	77
8.2	RNN Score distribution for ggF and VBF signals and backgrounds.	78
8.3	ROC curve using k-fold validation for RNN.	79

8.4	Comparison of GGF Z' limits for different RNN score selections. The bottom panel shows the ratio of the upper limits set for different RNN cuts to the cut-based analysis. In this panel smaller numbers, indicate that the expected upper limit is smaller than the cut-based analysis, which is desired.	80
8.5	Event Categorization. Natasha write more.	83
8.6	Data MC comparison for the merged WW HP TCR. The bottom panel shows the ratio of the difference between data and simulation to simulation. The red bands include the all systematic and statistical uncertainties on the background.	84
8.7	Data MC comparison for the merged WW LP TCR. The bottom panel shows the ratio of the difference between data and simulation to simulation. The red bands include the all systematic and statistical uncertainties on the background.	85
8.8	Data MC comparison for the merged WZ HP TCR. The bottom panel shows the ratio of the difference between data and simulation to simulation. The red bands include the all systematic and statistical uncertainties on the background.	86
8.9	Data MC comparison for the merged WZ LP TCR. The bottom panel shows the ratio of the difference between data and simulation to simulation. The red bands include the all systematic and statistical uncertainties on the background.	87
8.10	Data MC comparison for the resolved WW TCR. The bottom panel shows the ratio of the difference between data and simulation to simulation. The red bands include the all systematic and statistical uncertainties on the background.	88
8.11	Data MC comparison for the resolved WZ TCR. The bottom panel shows the ratio of the difference between data and simulation to simulation. The red bands include the all systematic and statistical uncertainties on the background.	89

8.12 Selection acceptance times efficiency for the $W' \rightarrow WZ \rightarrow \ell\nu qq$ events from MC simulations as a function of the W' mass for (a) Drell-Yan and (b) VBF production, combining the merged HP and LP signal regions of the $WV \rightarrow \ell\nu J$ selection and the resolved regions of the $WV \rightarrow \ell\nu jj$ selection.	90
8.13 Selection acceptance times efficiency for the $G \rightarrow WW \rightarrow \ell\nu qq$ events from MC simulations as a function of the G mass for (a) Drell-Yan and (b) VBF production, combining the merged HP and LP signal regions of the $WV \rightarrow \ell\nu J$ selection and the resolved regions of the $WV \rightarrow \ell\nu jj$ selection.	91
8.14 The E_T^{miss} distribution in MJCR for 2017 data in the electron channel(left), muon channel with W-boson pT < 150 GeV (center) and > 150 GeV (right). Multi-jet templates are calculated as remaining data components after excluding known MC	93
8.15 Postfit Data/MC comparison of distributions of E_T^{miss} , m_T^W , lepton and neutrino p_T , $m_{\ell\nu jj}$, lepton- ν angular distance in the WW electron channel. The MJ template is obtained from the pre-MJ-fit.	94
8.16 Postfit Data/MC comparison of distributions of E_T^{miss} , m_T^W , lepton and neutrino p_T , $m_{\ell\nu jj}$, lepton- ν angular distance in the WW muon channel. The MJ template is obtained from the pre-MJ-fit.	95
8.17 Postfit Data/MC comparison of distributions of E_T^{miss} , m_T^W , lepton and neutrino p_T , $m_{\ell\nu jj}$, lepton- ν angular distance in the WZ untag electron channel. The MJ template is obtained from the pre-MJ-fit.	96
8.18 Postfit Data/MC comparison of distributions of E_T^{miss} , m_T^W , lepton and neutrino p_T , $m_{\ell\nu jj}$, lepton- ν angular distance in the WZ untag muon channel. The MJ template is obtained from the pre-MJ-fit.	97
8.19 Postfit Data/MC comparison of distributions of E_T^{miss} , m_T^W , lepton and neutrino p_T , $m_{\ell\nu jj}$, lepton- ν angular distance in the WZ untag electron channel. The MJ template is obtained from the pre-MJ-fit.	98

8.20 Postfit Data/MC comparison of distributions of E_T^{miss} , m_T^W , lepton and neutrino p_T , $m_{\ell\nu jj}$, lepton- ν angular distance in the WZ untag muon channel. The MJ template is obtained from the pre-MJ-fit.	99
8.21 Postfit Data/MC comparison of distributions of E_T^{miss} , m_T^W , lepton and neutrino p_T , $m_{\ell\nu jj}$, lepton- ν angular distance in the VBF WW electron channel. The MJ template is obtained from the pre-MJ-fit.	100
8.22 Postfit Data/MC comparison of distributions of E_T^{miss} , m_T^W , lepton and neutrino p_T , $m_{\ell\nu jj}$, lepton- ν angular distance in the VBF WW muon channel. The MJ template is obtained from the pre-MJ-fit.	101
8.23 Postfit Data/MC comparison of distributions of E_T^{miss} , m_T^W , lepton and neutrino p_T , $m_{\ell\nu jj}$, lepton- ν angular distance in the VBF WZ electron channel. The MJ template is obtained from the pre-MJ-fit.	102
8.24 Postfit Data/MC comparison of distributions of E_T^{miss} , m_T^W , lepton and neutrino p_T , $m_{\ell\nu jj}$, lepton- ν angular distance in the VBF WZ muon channel. The MJ template is obtained from the pre-MJ-fit.	103
9.1 The W/Z+jet systematics for the a) Merged ggF, b) Resolved ggF, c) Merged VBF, and d) Resolved VBF regions. The top subplot shows the nominal and variation distributions/bands, the middle shows the ratio of the two, and the final shows just the shape of the envelope (the final uncertainty).	109
9.2 The two-point generator comparison between Sherpa and MadGraph for the W/Z+jet samples in the a) Merged ggF, b) Resolved ggF, c) Merged VBF, and d) Resolved VBF regions. The normalization of the Madgraph sample is set to the Sherpa value to consider only shape effects. The bottom inlet shows the ratio of the two.	110
9.3 Ratio between the variations of generator (red) and hadronization (blue) variations for the Merged regime for $t\bar{t}$ sample.	111
9.4 Ratio between the variations of generator (red) and hadronization (blue) variations for the Resolved regime for $t\bar{t}$ sample.	111

9.5	Ratio between the variations of ISR up (red) and down (blue) variations for the Merged regime for $t\bar{t}$ sample.	112
9.6	Ratio between the variations of ISR up (red) and down (blue) variations for the Resolved regime for $t\bar{t}$ sample.	113
9.7	Ratio between the variations of FSR up (red) and down (blue) variations for the Merged regime for $t\bar{t}$ sample.	114
9.8	Ratio between the variations of FSR up (red) and down (blue) variations for the Resolved regime for $t\bar{t}$ sample.	114
10.1	The HVT signal mass resolution as a function of mass fit with a straight line in the Resolved ggF region (left) and VBF (right) region.	118
10.2	The HVT signal mass resolution as a function of mass fit with a straight line in the Merged ggF region (left) and VBF (right) region.	118
11.1	These plots show the measured p_0 value as a function of resonance mass for HVT Z' DY production.	124
11.2	These plots show the measured p_0 value as a function of resonance mass for HVT Z' VBF production.	125
11.3	These plots show the measured p_0 value as a function of resonance mass for HVT W' DY production.	126
11.4	These plots show the measured p_0 value as a function of resonance mass for HVT W' VBF production.	127
11.5	These plots show the measured p_0 value as a function of resonance mass for the RS Graviton DY production.	128
11.6	Ranked systematics and their fitted values for WW DY (right) and VBF (left) selections.	129
11.7	Ranked systematics and their fitted values for WZ DY (right) and VBF (left) selections.	130
11.8	Correlations between systematics for WW DY (right) and VBF (left) selections.	130

11.9 This figure shows the distribution of $m_{\ell\nu qq}$ in the DY WW control regions.	138
11.10 This figure shows the distribution of $m_{\ell\nu qq}$ in the DY WZ control regions.	139
11.11 This figure shows the distribution of $m_{\ell\nu qq}$ in the VBF WW control regions.	140
11.12 This figure shows the distribution of $m_{\ell\nu qq}$ in the VBF WZ control regions.	141
11.13 This figure shows the distribution of $m_{\ell\nu qq}$ in the GGF WW signal regions.	142
11.14 This figure shows the distribution of $m_{\ell\nu qq}$ in the GGF WZ Untag signal regions.	142
11.15 This figure shows the distribution of $m_{\ell\nu qq}$ in the GGF WZ Tag signal regions.	143
11.16 This figure shows the distribution of $m_{\ell\nu qq}$ in the VBF WZ Tag signal regions.	143
11.17 This figure shows the distribution of $m_{\ell\nu qq}$ in the VBF WZ Tag signal regions.	144
11.18 This figure shows theory, expected and observed limits for HVT W' DY (left) and VBF (right) production.	144
11.19 This figure shows theory, expected and observed limits for HVT Z' DY (left) and VBF (right) production.	145
11.20 This figure shows theory, expected and observed limits for RS Gravitons via DY production.	145
12.1 PDGID of the truth-level parton matched to the small-R jets passing the Resolved GGF WW Signal Region selections for the (a) Leading (b) Sub-Leading jets . These distributions are shown for 300, 500, and 700GeV Z' signals and the background.	149

12.2 The number of tracks in small-R jets in events passing the Resolved GGF WW Signal Region selections for the (a) Leading (b) Sub-Leading jets. These distributions are shown for 300, 500, and 700GeV Z' signals and the background.	149
12.3 The number of tracks in background small-R jets in events passing the Resolved GGF WW Signal region selection vs. $\ln(p_T)$ for (a)Leading (b) Sub-Leading jets. The best fit line for the distribution is also shown, as well as the percentage of jets that pass a cut of number of tracks $< 4 \times \ln(p_T) - 5$. Note the number of total entries in these plots has been normalized to one.	150
12.4 The number of tracks in small-R jets in 300GeV Z' events passing the Resolved GGF WW Signal region selection vs. $\ln(p_T)$ for (a)Leading (b) Sub-Leading jets. The best fit line for the distribution is also shown, as well as the percentage of jets that pass a cut of number of tracks $< 4 \times \ln(p_T) - 5$.Note the number of total entries in these plots has been normalized to one.	150
12.5 The number of tracks in small-R jets in 500GeV Z' events passing the Resolved GGF WW Signal region selection vs. $\ln(p_T)$ for (a)Leading (b) Sub-Leading jets. The best fit line for the distribution is also shown, as well as the percentage of jets that pass a cut of number of tracks $< 4 \times \ln(p_T) - 5$.Note the number of total entries in these plots has been normalized to one.	151
12.6 The number of tracks in small-R jets in 700GeV Z' events passing the Resolved GGF WW Signal region selection vs. $\ln(p_T)$ for (a)Leading (b) Sub-Leading jets. The best fit line for the distribution is also shown, as well as the percentage of jets that pass a cut of number of tracks $< 4 \times \ln(p_T) - 5$.Note the number of total entries in these plots has been normalized to one.	151

12.7 The number of tracks in leading small-R jets in background events passing the Resolved GGF WW Signal region selection vs. $\ln(p_T)$ for (a)Gluons (b) Quarks jets. The best fit line for the distribution is also shown, as well as the percentage of jets that pass a cut of number of tracks $< 4 \times \ln(p_T) - 5$.Note the number of total entries in these plots has been normalized to one.	152
12.8 ROC Curve for Quark and Gluon Tagging with a cut on the number of tracks that depends on the $\ln(p_T)$	152
12.9 The top panel shows the distribution of m_{lvqq} with and without quark gluon tagging. The middle panel shows the ratio of the signals and backgrounds with and without quark gluon tagging. The bottom panel shows the change in S/\sqrt{B} with quark gluon tagging.	153
14.1 The top panel shows the distribution of m_{lvqq} with and without requiring jets to be true quarks. The middle panel shows the ratio of the signals and backgrounds with and without requiring jets to be true quarks. The bottom panel shows the change in S/\sqrt{B} when requiring jets to be true quarks.	161
14.2 Unfolded and extracted n_C qg dstbs.	162
14.3 PDGID of the truth-level parton matched to the small-R jets passing the Resolved GGF WW Signal Region selections for the (a) Leading (b) Sub-Leading jets . These distributions are shown for 300, 500, and 700GeV Z' signals and the background.	163
14.4 These figures show the impact of the uncertainties on the number of tracks in the leading jet in the sum of the background sample in the Resolved GGF WW SR (a) tracking efficiency (b) fake (c) PDF (d) ME (e) unfolding uncertainties.	164

List of Tables

1.1	Representations of the SM fermions under $SU(3)_C \times SU(2)_L \times U(1)_Y$ gauge symmetry group. $SU(2)_L$ gauge transformations allow one to go between rows and $SU(3)_C$ transformations allow one to go between columns in these fermion representations. [REWORD]	10
8.1	The list of triggers used in the analysis.	74
8.2	Summary of selection criteria used to define the signal region (SR), W +jets control region (W CR) and $t\bar{t}$ control region ($t\bar{t}$ CR) for merged 1-lepton channel.	82
8.3	The list of selection cuts in the resolved analysis for the WW and WZ signal regions (SR), W +jets control region (WR) and $t\bar{t}$ control region (TR).	83
8.4	Definitions of “inverted” leptons used in multijet control region . .	93
8.5	Fit validation result in WCRs for 2015+16 data. The fit is done in various WCRs, in order to obtain the corresponding scale factors for MJ templates: ggF resolved WCR for the $WW \rightarrow lvqq$ selection, ggF resolved untagged WCR for the $WZ \rightarrow lvqq$ selection, ggF resolved tagged WCR for the $WZ \rightarrow lvqq$ selection, VBF resolved WCR for the $WW \rightarrow lvqq$ selection, and VBF resolved WCR for the $WZ \rightarrow lvqq$ selection. Post-fit event yields for electroweak processes and MJ contributions are shown. The SF column shows the corresponding normalization scale factors for electroweak processes from the fit. R.U. stands for relative uncertainty.	104

11.1	Expected and Measured for DY WW $W+\text{jets}$, $t\bar{t}$ control regions and signal regions.	131
11.2	Expected and Measured for DY WZ $W+\text{jets}$, $t\bar{t}$ tag and untag control regions.	132
11.3	Expected and Measured for DY WZ $W+\text{jets}$, $t\bar{t}$ tag and untag signal regions.	133
11.4	Expected and Measured for VBF WW $W+\text{jets}$, $t\bar{t}$ control regions and signal regions.	134
11.5	Expected and Measured for VBF WZ $W+\text{jets}$, $t\bar{t}$ control regions and signal regions.	135
11.6	Fitted background normalizations for $t\bar{t}$ and $W+\text{jets}$ backgrounds for the DY WW analysis region.	136
11.7	Fitted background normalizations for $t\bar{t}$ and $W+\text{jets}$ backgrounds for the DY WZ analysis region.	136
11.8	Fitted background normalizations for $t\bar{t}$ and $W+\text{jets}$ backgrounds for the VBF WW analysis region.	136
11.9	Fitted background normalizations for $t\bar{t}$ and $W+\text{jets}$ backgrounds for the VBF WZ analysis region.	137

Abstract

Search for WW and WZ Resonances in $\ell\nu qq$ final states in pp collisions at

$\sqrt{s} = 13$ TeV with the ATLAS detector

by

Natasha Woods

This thesis presents a search for WW and WZ resonances using data from pp collisions at $\sqrt{s} = 13$ TeV using the ATLAS detector, corresponding to an integrated luminosity of 139 fb^{-1} . Diboson resonances are predicted in a number of Standard Model (SM) extensions, such as Extended Gauge Models, and Extra dimensional models. This search looks for resonances where one W boson decays leptonically and the other W or Z boson decays hadronically. This search is sensitive to diboson resonance production via vector-boson fusion as well as quark-antiquark annihilation and gluon-gluon fusion mechanisms. No significant excess of events is observed with respect to the Standard Model backgrounds, and constraints on the masses of new W' , Z' , and bulk-RS Gravitons are extended to up to 3.3 TeV, depending on the model. As the dominant backgrounds in this search contain gluons, classifying jets as quark-initiated or gluon-initiated would make this analysis more sensitive to new physics. Towards this end, this thesis provides a calibrated quark-gluon tagger based on the multiplicity of charged particles within a jet.

Loving Dedication

å

xviii

Acknowledgments

Proper acknowledgments of everyone else who helped you graduate. Write later.

1 In general, humanity has continually strived to understand the structure and
2 dynamics of reality for widely varying reasons. Each academic field uses a spe-
3 cific set of concepts and models to describe nature. Physics is one such field,
4 that uses mathematical objects to systematically develop testable models about
5 the universe. Currently, the most fundamental types particles are fermions and
6 bosons. Fermions are the particles that make up the "ordinary" matter of the
7 universe, while bosons are the quanta of the fundamental forces. The Standard
8 Model (SM) of particle physics describes the quantum behavior of three of the
9 four fundamental forces: electromagnetic, strong, and weak forces.

10 The Standard Model has consistently described much of reality to an extreme
11 degree of accuracy. It has predicted cross sections for strong and electroweak
12 processes that span over ten orders of magnitude [see Fig. 2.1] and contains no
13 known logical inconsistencies. Despite the strength and reality of the Standard
14 Model, it still fails to describe aspects of reality and suffers from aesthetic is-
15 sues. The SM fails to account for dark matter, dark energy, neutrino masses, the
16 hierarchy of the strengths of the fundamental forces, and other issues that may
17 have not been noticed yet! This incompleteness of the SM may indicate that a
18 more fundamental theory exists. It is hoped that such a theory would address the
19 aforementioned phenomena and explain and motivate the ad-hoc structure and
20 parameter values of the SM. One of the fundamental limitations of the SM is that
21 it does not describe gravity. In the lower energy regime (e.g. electroweak scale),
22 the strength of gravity is negligible in comparison to the other forces. In the higher
23 energy regimes, near the Planck scale, the strength of gravity is non-negligible in
24 comparison to the other forces

25 This thesis presents a search for WW and WZ resonances using data from
26 pp collisions at $\sqrt{s} = 13$ TeV using the ATLAS detector, corresponding to an

27 integrated luminosity of 139 fb^{-1} . Diboson resonances are predicted in a number
28 of Standard Model (SM) extensions, such as Extended Gauge Models, and Extra
29 dimensional models. This search looks for resonances where one W boson decays
30 leptonically and the other W or Z boson decays hadronically. This search is
31 sensitive to diboson resonance production via vector-boson fusion as well as quark-
32 antiquark annihilation and gluon-gluon fusion mechanisms.

33 No significant excess of events is observed with respect to the Standard Model
34 backgrounds, and constraints on the masses of new W' , Z' , and bulk-RS Gravi-
35 tons are extended to up to 3.3 TeV, depending on the model. As the dominant
36 backgrounds in this search contain gluons, classifying jets as quark-initiated or
37 gluon-initiated would make this analysis more sensitive to new physics. Towards
38 this end, this thesis provides a calibrated quark-gluon tagger based on the multi-
39 plicity of charged particles within a jet.

Part I

40

Theoretical Motivation

41

⁴² **Chapter 1**

⁴³ **The Standard Model of Particle
Physics**

⁴⁵ **1.1 Introduction**

⁴⁶ By determining the dynamics of the most elementary degrees of freedom, par-
⁴⁷ ticle physics hopes to uncover the fundamental laws of the universe. The definition
⁴⁸ of elementary has evolved through time and currently refers to matter and force
⁴⁹ mediating particles: fermions and bosons, respectively. The Standard Model of
⁵⁰ Particle Physics (SM) describes the quantum behavior of three of the four funda-
⁵¹ mental forces: weak, strong, and electromagnetic, via boson and fermion interac-
⁵² tions. Gravity is not included in the SM and still under investigation.

⁵³ **1.2 Quantum Field Theory**

⁵⁴ In the SM, forces (and particles) are represented as fields. In this context,
⁵⁵ fields are mathematical objects that define a tensor (e.g. scalar, vector, etc) at
⁵⁶ every point on a manifold, here the manifold is space-time. These fields obey laws

⁵⁷ dictated by Quantum Field Theory (QFT). Particles arise naturally in QFT as
⁵⁸ quantized field excitations localized in spacetime.

⁵⁹ According to Noether's theorem, symmetries of a field give rise to conserved
⁶⁰ quantities (e.g. time-translation invariance leads to energy conservation). Often
⁶¹ in the history of physics, a conserved quantity of a field is found and then the
⁶² underlying symmetry of the field is inferred. Gauge symmetries are symmetries
⁶³ among the internal degrees of freedom of the field (components of the tensor),
⁶⁴ which give rise to quantities associated with fields. By specifying the symmetries
⁶⁵ of a system the dynamics and conserved quantities of the system may be succinctly
⁶⁶ defined.

⁶⁷ 1.3 $U(1)_{EM}$ Local Gauge Invariance

⁶⁸ The Lagrangian of Quantum Electrodynamics (QED) describes the electro-
⁶⁹ magnetic force. QED may be derived by requiring local $U(1)_{EM}$ gauge invariance
⁷⁰ of the free dirac fermion Lagrangian, ψ :

$$\mathcal{L} = i\bar{\psi}\gamma^\mu\partial_\mu\psi - m\bar{\psi}\psi \quad (1.1)$$

⁷¹ This symmetry may be represented as a complex number with unit modulus,
⁷² $e^{i\theta}$. $U(1)$ gauge invariance requires this gauge transformation of ψ will leave the
⁷³ Lagrangian unchanged.

$$\psi(x) \rightarrow \psi'(x) = e^{i\theta(x)}\psi(x) \quad (1.2)$$

⁷⁴ NB: This transformation is a local gauge transformation as θ depends on the
⁷⁵ spacetime coordinate.

⁷⁶ By requiring this symmetry of the free Dirac fermion Lagrangian:

$$\mathcal{L} = i\bar{\psi}\gamma^\mu\partial_\mu\psi - m\bar{\psi}\psi \quad (1.3)$$

⁷⁷ The mass term is unaffected, but the kinetic term is modified due to $\theta(x)$.

$$\mathcal{L} \rightarrow \mathcal{L}' = i\bar{\psi}e^{-i\theta(x)}\gamma^\mu\partial_\mu\psi e^{i\theta(x)} - m\bar{\psi}e^{-i\theta(x)}\psi e^{i\theta(x)} \quad (1.4)$$

⁷⁸

$$= i\psi\gamma^\mu(\partial_\mu\psi + i\psi\partial_\mu\theta) - m\bar{\psi}\psi \quad (1.5)$$

⁷⁹ The $\partial_\mu\theta$ terms breaks the gauge invariance of the Lagrangian. By introducing a
⁸⁰ new field, A_μ we can recover the gauge invariance of the derivative. Now redefining
⁸¹ the derivative as the covariant derivative:

$$D_\mu\psi \equiv (\partial_\mu - iqA_\mu)\psi \quad (1.6)$$

⁸² And letting A_μ transform under $U(1)$ as:

$$A_\mu \rightarrow A_\mu + \delta A_\mu \quad (1.7)$$

⁸³ The transformed covariant derivative becomes:

$$D_\mu\psi \rightarrow D_\mu\psi' = (\partial_\mu - iqA_\mu)\psi' \quad (1.8)$$

⁸⁴

$$= (\partial_\mu - iq(A_\mu + \delta A_\mu))\psi e^{i\theta} \quad (1.9)$$

⁸⁵

$$= e^{i\theta}D_\mu + ie^{i\theta}\psi(\partial_\mu\theta - q\delta A_\mu) \quad (1.10)$$

⁸⁶ The covariant derivative can be made gauage invariant by setting the last term
⁸⁷ to zero.

$$\delta A_\mu = \frac{1}{q} \partial_\mu \theta \quad (1.11)$$

88 So now A_μ transforms as:

$$A_\mu \rightarrow A_\mu + \frac{1}{q} \partial_\mu \theta \quad (1.12)$$

89 Finally, replacing the derivative with the covariant derivative the Dirac La-
90 grangian we have:

$$\mathcal{L} = i\bar{\psi}\gamma^\mu D_\mu \psi - m\bar{\psi}\psi - \frac{1}{4}F_{\mu\nu}F^{\mu\nu} \quad (1.13)$$

$$\quad \quad \quad = \mathcal{L}_{QED} \quad (1.14)$$

92 Here $F_{\mu\nu} \equiv \partial_\mu A_\nu - \partial_\nu A_\mu$. This last term in the Lagrangian is the kinetic
93 energy of the gauge boson field.

94 So we have derived the QED Lagrangian. By requiring the free Dirac La-
95 grangian to be invariant under U(1) transformations we have generated a new
96 gauge boson field, A_μ , which describes the photon. As expected the photon inter-
97 acts with fermions.

98 Stepping back, a global U(1) gauge symmetry of the free Dirac Lagrangian
99 implies we cannot measure the absolute phase of a charged particle. A local U(1)
100 gauge symmetry changes the phase of fields differently across space time. For this
101 type of transformation to leave the Lagrangian invariant, we had to introduce an
102 additional field, A_μ , which "communicates" these phase changes across space-time.
103 In less formal language this effectively means: if the field at one location changes,
104 this change is conferred to other particles via A_μ .

¹⁰⁵ 1.4 Yang-Mills Gauge Theories

¹⁰⁶ Requiring $U(1)_{EM}$ gauge invariance of the free Dirac Lagrangian gave us QED.

¹⁰⁷ Requiring different gauge symmetries we can derive the structure of other interactions.
¹⁰⁸ Any gauge symmetry may be written as:

$$\psi_i \rightarrow \exp(i\theta^a T_{ij}^a) \psi_j \quad (1.15)$$

¹⁰⁹ Here θ is a dimensionless real parameter and T is the generator of the gauge symmetry group. With this the covariant derivative can be written as:

$$D_\mu \psi_i \equiv \partial_\mu \psi_i + ig A_\mu^a T_{ij}^a \psi_j \quad (1.16)$$

¹¹¹ Then the gauge field must transform as:

$$A_\mu^a \rightarrow A_\mu^a - \frac{1}{g} \partial_\mu \theta^a - f^{abc} \theta^b A_\mu^c \quad (1.17)$$

¹¹² Here f is the structure constant of the gauge group. The field strength tensor
¹¹³ is given by:

$$F_{\mu\nu}^a \equiv \partial_\mu A_\nu^a - \partial_\nu A_\mu^a - g f^{abc} A_\mu^b A_\nu^c \quad (1.18)$$

¹¹⁴

$$F_{\mu\nu}^a \rightarrow F_{\mu\nu}^a - f^{abc} \theta^b F_{\mu\nu}^c \quad (1.19)$$

¹¹⁵ This gives the Yang-Mills Lagrangian:

$$\mathcal{L}_{YM} = -\frac{1}{4} F_{\mu\nu}^a F_{\mu\nu}^a + i \bar{\psi}_i \gamma^\mu D_\mu \psi_i + m \bar{\psi}_i \psi_i \quad (1.20)$$

¹¹⁶ 1.5 Particles in the Standard Model

¹¹⁷ The SM consists of fermions (half-integer spin matter constituents) and bosons
¹¹⁸ (integer spin force mediators). Fermions are spinor representations of the Poincare
¹¹⁹ group and can be further separated into leptons and quarks. Bosons are the result
¹²⁰ of requiring a particular symmetry among the spinor fields:

$$SU(3)_C \times SU(2)_L \times U(1)_Y \quad (1.21)$$

¹²¹ $SU(3)_C$ is the symmetry group of the strong force and generates eight gluon
¹²² fields, G_μ . $SU(2)_L$ is the symmetry group of the Electroweak force and generates
¹²³ three electroweak boson fields. The mixing of this $SU(2)_L$ and $U(1)_Y$ gives rise
¹²⁴ to the photon field, where Y is the weak-hypercharge:

$$Y = 2(Q - T_3) \quad (1.22)$$

¹²⁵ Q is the electromagnetic charge, and T_3 is the z-component of the weak isospin.
¹²⁶ Weak isospin is the charge associated with the $SU(2)_L$ symmetry. The correspond-
¹²⁷ ing covariant derivative is then:

$$D_\mu \phi \equiv (\partial_\mu + ig_1 B_\mu Y_{L/R} + [ig_2 W_\mu^\alpha T^\alpha]_L + [ig_3 G_\mu^\alpha \tau^\alpha]_C) \psi \quad (1.23)$$

¹²⁸ It is important to note that the gauge symmetry of the SM yields a particular
¹²⁹ structure of the fermion representations. So for a given fermion to interact with
¹³⁰ a given gauge field it must have a non-zero corresponding Noether charge for
¹³¹ that gauge symmetry. If the corresponding Noether charge is zero, that fermion
¹³² transforms as a singlet and does not participate in that gauge interaction.

¹³³ Fermions are divided into quarks and leptons based on their transformations
¹³⁴ under $SU(3)_C$. Quarks transform as color triplets. Leptons transform as color

singlets and consequently do not interact with gluons. Fermions may be further
 classified by their $SU(2)_L$ interactions. Only the left-chiral part of fermions (denoted by L here) transform as $SU(2)_L$ doublets, the right-chiral part forms singlets under this gauge. Lastly, all these groups of particles come in three generations, each a heavier copy of the previous, but with differing flavor quantum numbers.
 This is summarized in Table 1.1 and shown in Figures 1.1 and 1.2.

SM Fermion Gauge Group	First Generation	Second Generation	Third Generation	$(SU(3)_C, SU(2)_L, U(1)_Y)$ Representations
Left-handed quarks	$\begin{pmatrix} u_L^r & u_L^g & u_L^b \\ d_L^r & d_L^g & d_L^b \end{pmatrix}$	$\begin{pmatrix} c_L^r & c_L^g & c_L^b \\ s_L^r & s_L^g & s_L^b \end{pmatrix}$	$\begin{pmatrix} t_L^r & t_L^g & t_L^b \\ b_L^r & b_L^g & b_L^b \end{pmatrix}$	$(3, 2, \frac{1}{6})$
Right-handed quarks	(u_R^r, u_R^g, u_R^b) (d_R^r, d_R^g, d_R^b)	(c_R^r, c_R^g, c_R^b) (s_R^r, s_R^g, s_R^b)	(t_R^r, t_R^g, t_R^b) (b_R^r, b_R^g, b_R^b)	$(3, 1, \frac{2}{3})$ $(3, 1, -\frac{1}{3})$
Left-handed leptons	$\begin{pmatrix} \nu_e^L \\ e_L \end{pmatrix}$	$\begin{pmatrix} \mu_e^L \\ \mu_L \end{pmatrix}$	$\begin{pmatrix} \tau_e^L \\ \tau_L \end{pmatrix}$	$(1, 2, -\frac{1}{2})$
Right-handed leptons	e_R	μ_R	τ_R	$(1, 1, -1)$

Table 1.1: Representations of the SM fermions under $SU(3)_C \times SU(2)_L \times U(1)_Y$ gauge symmetry group. $SU(2)_L$ gauge transformations allow one to go between rows and $SU(3)_C$ transformations allow one to go between columns in these fermion representations. [REWORD]

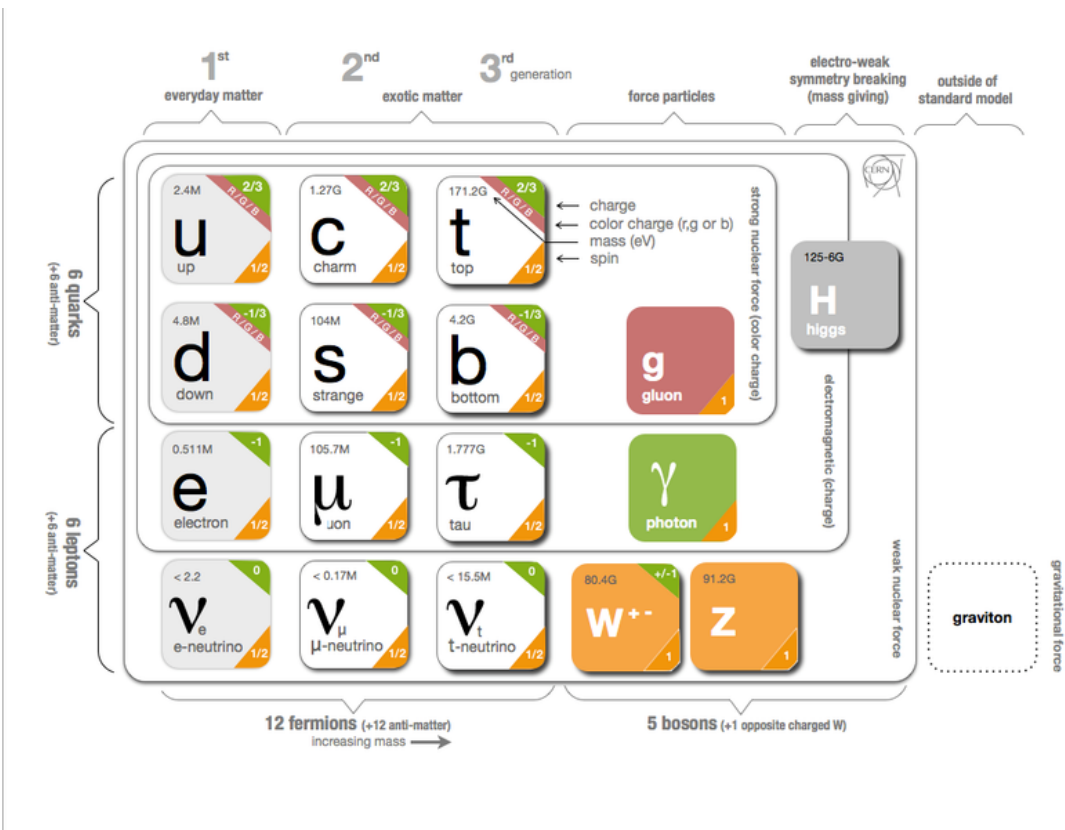


Figure 1.1: The particles of the Standard Model.

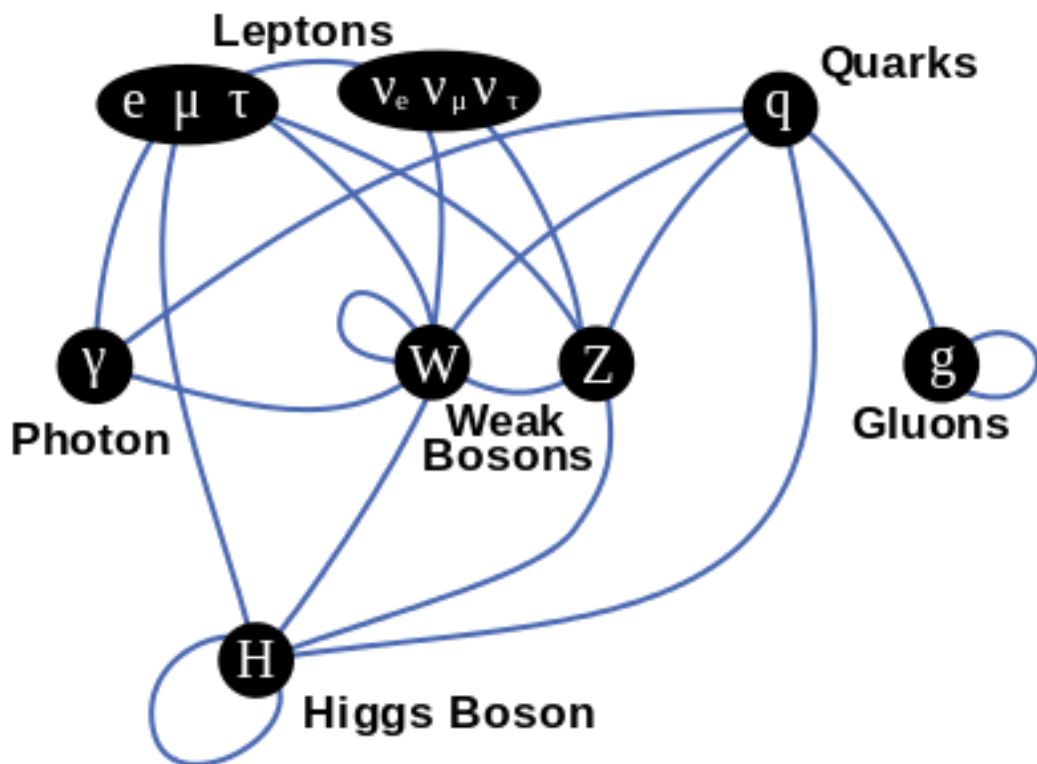


Figure 1.2: Summary of how Standard Model particles interact with other Standard Model particles.

¹⁴¹ Now we can understand the SM Lagrangian density as a Yang-Mills theory
¹⁴² with the gauge group: $SU(3)_C \times SU(2)_L \times U(1)_Y$ with an additional $SU(2)$ complex
¹⁴³ scalar Higgs field doublet that will be discussed later.

$$\begin{aligned} \mathcal{L}_{SM} = & \underbrace{-\frac{1}{4}B_{\mu\nu}B^{\mu\nu} - \frac{1}{4}W_{\mu\nu}^a W^{a\mu\nu} - \frac{1}{4}G_{\mu\nu}^\alpha G^{\alpha\mu\nu}}_{\text{Kinetic Energies and Self-Interactions of Gauge Bosons}} \\ & + \underbrace{\bar{L}_i \gamma^\mu (i\partial_\mu - \frac{1}{2}g_1 Y_{iL} B_\mu - \frac{1}{2}g_2 \sigma^a W_\mu^a) L_i}_{\text{Kinetic Energies and EW Interactions of Left-handed Fermions}} \\ & + \underbrace{\bar{R}_i \gamma^\mu (i\partial_\mu - \frac{1}{2}g_1 Y_{iR} B_\mu) R_i}_{\text{Kinetic Energies and EW Interactions of Right-Handed Fermions}} \\ & + \underbrace{\frac{ig_3}{2} \bar{Q}_j \gamma^\mu \lambda^\alpha G_\mu^\alpha Q_j}_{\text{Strong Interactions between Quarks and Gluons}} \\ & + \underbrace{\frac{1}{2} |(i\partial_\mu - \frac{1}{2}g_1 B_\mu - \frac{1}{2}g_2 \sigma^a W_\mu^a)\Phi|^2 - V(\Phi)}_{\text{Electroweak Boson Masses and Higgs Couplings}} \\ & - \underbrace{(y_{kl}^d \bar{L}_k \Phi R_l + y_{kl}^u \bar{R}_k \tilde{\Phi} L_l + h.c.)}_{\text{Fermion Mass terms and Higgs Couplings}} \end{aligned}$$

¹⁴⁴ Here several abstract spaces are being spanned:

- ¹⁴⁵ – a spans the three $SU(2)_L$ gauge fields with generators expanded in Pauli matrices, $T^\alpha = \frac{1}{2}\sigma^\alpha$
- ¹⁴⁷ – α spans the eight $SU(3)_C$ gauge fields, with generators expanded in Gell-Mann matrices, $\tau^\alpha = \frac{1}{2}\lambda^\alpha$
- ¹⁴⁹ – L/R represent left and right projections of Dirac fermion fields. The Strong interaction is not chiral, so $Q = L+R$

151 – μ and ν are four-vector indices

152 – i, j, k are summed over the three generations of SM particles.

153 1.6 Higgs Mechanism

154 The SM Lagrangian without the addition of a Higgs field does not allow for
155 gauge boson and fermion mass terms: $\frac{1}{2}m_A^2 A_\mu A_\mu$ and $m(\bar{\psi}\psi)$, as these terms are
156 not gauge invariant. By introducing the Higgs field, mass terms for these particles
157 may be included in a gauge invariant way. This field is a complex doublet with a
158 potential $V(\Phi)$:

$$\Psi = \begin{pmatrix} \Phi^\dagger \\ \Phi^0 \end{pmatrix} \quad (1.24)$$

159 $V(\Phi) = \mu^2 \Phi^\dagger \Phi + \lambda |\Phi^\dagger \Phi|^2 \quad (1.25)$

160 The minima of this field occurs for $|\Phi| = \sqrt{\frac{\mu^2}{2\lambda}} \equiv \frac{v}{2}$. This yields degenerate
161 minima, this symmetry is broken by choosing a specific minima (a.k.a. sponta-
162 neous symmetry breaking). By convention $\Phi_{min} = \frac{1}{\sqrt{2}} \begin{pmatrix} 0 \\ v \end{pmatrix}$ is chosen. This means
163 the ground state of the Higgs field (Higgs vacuum) is non-zero, $\sqrt{\frac{-\mu^2}{\lambda}}$. The Higgs
164 Field may now be expanded around this new ground state:

$$\Phi(x) = \frac{1}{\sqrt{2}} \begin{pmatrix} 0 \\ v + h(x) \end{pmatrix} \quad (1.26)$$

165 This non-zero Higgs vacuum now generates mass terms for the gauge bosons
166 from the following term in the Lagrangian:

$$|(-\frac{1}{2}g_1B_\mu - \frac{1}{2}g_2\sigma^aW_\mu^a)\Phi|^2 = \frac{1}{2}m_W^2W_\mu^+W^{-\mu} + \frac{1}{2}m_Z^2Z_\mu Z^\mu \quad (1.27)$$

167 where:

$$W_\mu^\pm \equiv \frac{1}{\sqrt{2}}(W_\mu^1 \mp iW_\mu^2) \quad (1.28)$$

$$Z_\mu \equiv \frac{1}{\sqrt{g_1^2 + g_2^2}}(g_2W_\mu^2 - g_1B_\mu) \quad (1.29)$$

$$m_W = \frac{v g_2}{\sqrt{2}} \quad (1.30)$$

$$m_Z = \frac{v}{\sqrt{2}}\sqrt{g_1^2 + g_2^2} \quad (1.31)$$

171 The Higgs field also generates a mass term for the Higgs boson and self-
172 interactions for the Higgs boson.

173 1.7 Electroweak Theory

174 $SU(2)_L$ generates W^\pm, W^0 gauge bosons, which would be massless if $SU(2)_L$
175 was a perfect symmetry. These bosons are massive as this symmetry is broken.

176 The mass eigenstates, Z and γ given by:

$$\begin{pmatrix} Z_\mu \\ A_\mu \end{pmatrix} = \begin{pmatrix} \cos \theta_W & -\sin \theta_W \\ \sin \theta_W & \cos \theta_W \end{pmatrix} \begin{pmatrix} W_\mu^3 \\ B_\mu \end{pmatrix} \quad (1.32)$$

177 Here θ_W is the Weinberg angle given by:

$$\cos \theta_W = \frac{g_2}{\sqrt{g_1^2 + g_2^2}} = \frac{m_W}{m_Z} \quad (1.33)$$

¹⁷⁸ 1.8 Quantum ChromoDynamics

¹⁷⁹ As mentioned earlier the Strong Force, which binds the proton together, is
¹⁸⁰ mediated by gluons. Quantum Chromodynamics is the QFT which describes the
¹⁸¹ interactions of quarks and gluons via $SU(3)_C$ symmetry. QCD contains features
¹⁸² not present in Electroweak Interactions due to $SU(3)_C$ generators not commuting
¹⁸³ (a.k.a. $SU(3)_C$ is a non-abelian group). For example, in QCD there is color
¹⁸⁴ confinement and asymptotic freedom due to the structure constants being non-
¹⁸⁵ zero. Requiring $SU(3)_C$ local gauge invariance implies:

$$\psi(x) \rightarrow \psi(x)' = \exp[i g_S \alpha(x) \cdot \hat{T}] \psi(x) \quad (1.34)$$

¹⁸⁶ where $\alpha(x)$ is the local phase function, g_S is the strong coupling constant, and
¹⁸⁷ \hat{T} are the eight generators of $SU(3)$ (note $\hat{T}^a = \frac{1}{2}\lambda^a a$, where λ^a are the Gell-Mann
¹⁸⁸ matrices). As the Gell-Mann matrices are 3x3, this means ψ has three degrees of
¹⁸⁹ freedom under these $SU(3)$ rotations. So we represent ψ under $SU(3)$ rotations
¹⁹⁰ as:

$$\psi = \begin{pmatrix} \psi_{red} \\ \psi_{green} \\ \psi_{blue} \end{pmatrix} \quad (1.35)$$

¹⁹¹ Consequently, particle fields transforming under $SU(3)$ rotations have three
¹⁹² components which physicists describe as color components (red, green, and blue).
¹⁹³ A particle's corresponding antiparticle has the corresponding anticolor. This color
¹⁹⁴ is the "charge" of QCD and is conserved under $SU(3)$ rotations. Combining colors,
¹⁹⁵ color neutral states (e.g. red and antired, or red, green and blue) may be created.
¹⁹⁶ For the Free Dirac Lagrangian to remain invariant under $SU(3)$ transformations,
¹⁹⁷ we must again postulate a boson field that modifies the derivative. The gluon

₁₉₈ field tensor is given by ($\alpha = 1, \dots, 8$):

$$G_{\mu\nu}^k = \partial^\mu G_\alpha^\nu - \partial^\nu G_\alpha^\mu - g_S f^{\alpha\beta\gamma} G_\beta^\mu G_\gamma^\nu \quad (1.36)$$

₁₉₉ Here $f^{\alpha\beta\gamma}$ are the structure constants of $SU(3)$. Combining all this gives the
₂₀₀ QCD Lagrangian:

$$\mathcal{L}_{QCD} = \bar{\psi}_q i\gamma^\mu (D_\mu)_{ij} \psi^{qj} - m \bar{\psi}^{qi} \psi_{qi} - \frac{1}{4} G_{\mu\nu}^\alpha G^{\alpha\mu\nu} \quad (1.37)$$

₂₀₁ Here i are the color indices, and q are the quark flavors. It is important to
₂₀₂ note that quarks transform under the fundamental representation of $SU(3)$, while
₂₀₃ gluons transform under the adjoint representation. This means quarks carry a
₂₀₄ single color charge (red, green, blue, antired, antigreen, antiblue) and gluons carry
₂₀₅ a color and anticolor charge.

₂₀₆ Figure 1.3 shows the three dominant QCD interactions. Since gluons carry
₂₀₇ color charge, they interact with one another. This does not occur in QED, as
₂₀₈ photons do not have electric charge and therefore do not interact with each other.
₂₀₉ In QED, a bare electron's effective charge is largest closest to the electron and
₂₁₀ decreases as a function of distance. This is because the QED vacuum fills with
₂₁₁ particle antiparticle pairs spontaneously, which screen the charge of the bare elec-
₂₁₂ tron. The larger the distance from the electron, the smaller the effective charge
₂₁₃ and therefore the weaker the force. So for a pair of electrons, as the distance
₂₁₄ between them increases the repulsive force decreases and they may be observed
₂₁₅ separately.

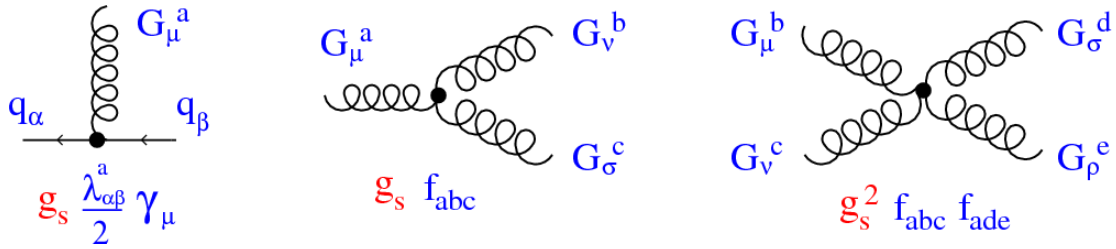


Figure 1.3: This figure shows the three dominant QCD interactions. From Ref. [16]

216 As the distance from a quark increases it's effective color charge increases due
 217 to the vacuum polarization in QCD. Color charge grows as the distance from
 218 the source increases (a.k.a. color is anti-screened in QCD). In this way, strong
 219 interactions become stronger at large distances (low momenta interactions). At
 220 small distances (large momenta interactions) strong interactions are significantly
 221 weaker and considered nearly free. This effect of referred to as asymptotic freedom.
 222 At large distances, a quark's effective charge is large and the strong force is more
 223 significant. This force becomes so strong that quarks form colorless bound states
 224 instead of remaining free particles. This effect is known as color confinement.
 225 This running of all SM fields is shown in Figure 1.4.

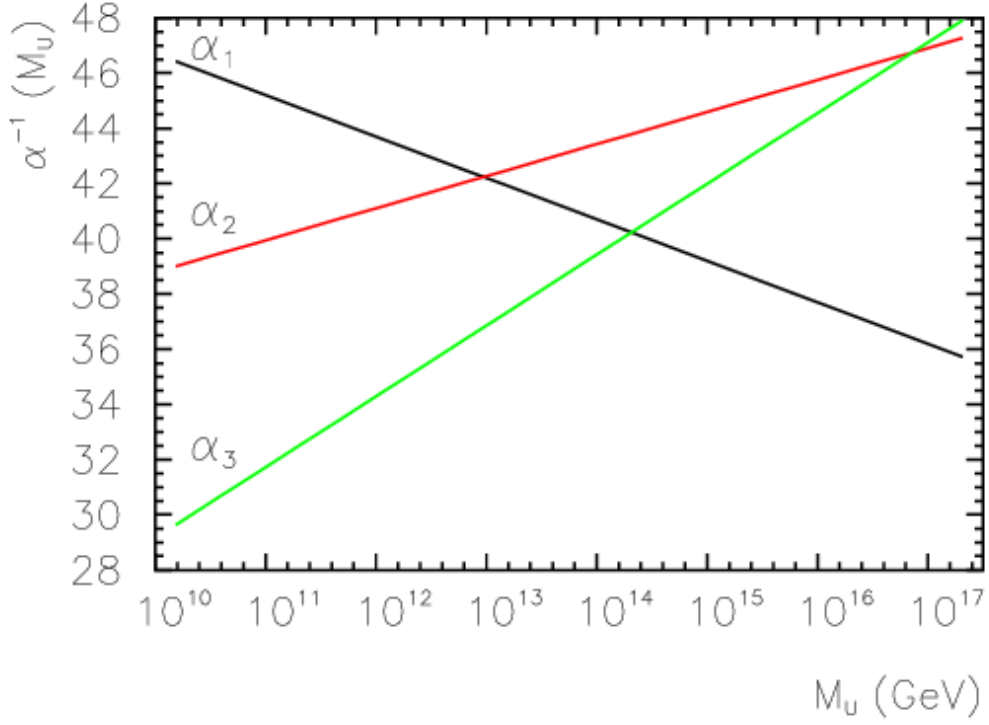


Figure 1.4: Strength of the U(1), SU(2), and SU(3) gauge couplings as a function of the energy scale of the interaction (Q). From Ref. [11]

Commonly the change in a particle's effective charge under a given force is quantified with $\beta(r) \equiv -\frac{de(r)}{d\ln r}$, where $e(r)$ is the effective charge of a given particle under a force. In QED this function is positive but in QCD this function is negative leading to confinement and asymptotic freedom. Moreover, one can calculate how the coupling (α) of a force varies with energies. (More deeply this amounts to incorporating renormalization and vacuum polarization in the boson propagators).

For QCD this is:

$$\alpha_S(x) = \frac{\alpha_S(\mu^2)}{1 + \beta_0 \alpha_S(\mu^2) \ln(Q^2/\mu^2)} \quad (1.38)$$

233

$$\beta_0 = \frac{11N_c - 2n_f}{12\pi} \quad (1.39)$$

234 where Q is the momentum of the the force is probed at, μ^2 is the renormalization scale.

236 As stated previously, quarks and gluons have not been observed in isolation.
 237 Instead they form bound colorless states. Hadronization is the process by which
 238 quarks and gluons form hadrons. The process of hadronization is still an active
 239 area of research. One qualitative description is show in Figure [Natasha add
 240 figure]. In this figure, as two quarks separate the color field between them is
 241 restricted to a tube with energy density of 1GeV/fm. As they separate further,
 242 the energy in the color field increases, until there is enough energy to produce
 243 $q\bar{q}$ pairs, which breaks the color field. This process repeats until quarks and
 244 antiquarks have low enough energy to form colorless hadrons. The resulting spray
 245 of hadrons is called a jet.

246 Since quarks and gluons carry different color charges, their respective jets have
 247 different properties. As quarks carry only a single color charge (vs. gluons which
 248 have color and anticolor charge), so their jets have less constituent particles. More
 249 precisely, the Altarelli-Parisi splitting functions [3] contain a factor C_A for gluon
 250 radiation off a gluon and C_F for gluon radiation off a quark ($C_A/C_F = 9/4$). These
 251 color factors are the prefactor in the Feynman diagrams for these processes [1],
 252 which leads to gluon jets having more constituents and therefore more tracks than
 253 quark jets. Gluon jets also tend to have a larger radius with lower momentum
 254 constituents than quarks. There are many novel techniques to distinguish quarks
 255 from gluons. For this study the number of charged particles will be focused on.

²⁵⁶ **Chapter 2**

²⁵⁷ **Standard Model Successes and
Limitations**

²⁵⁹ The Standard Model has consistently described much of reality to an extreme
²⁶⁰ degree of accuracy. It has predicted cross sections for strong and electroweak pro-
²⁶¹ cesses that span over ten order of magnitude correctly [see Fig 2.1] and contains
²⁶² no known logical inconsistencies. Despite the strength and reality of the Stan-
²⁶³ dard Model, it still fails to describe aspects of reality and suffers from aesthetic
²⁶⁴ issues. To date, dark matter and energy comprise 95% of the universe, but are
²⁶⁵ not accounted for in the SM. Additionally, neutrinos are known to have mass but
²⁶⁶ are massless in the SM. There are mechanisms for introducing massive neutrinos
²⁶⁷ in the SM, but these mechanisms create hierarchy problems.

²⁶⁸ Possibly the most significant aesthetic issue is the hierarchy between the elec-
²⁶⁹ troweak and Planck scales. The electroweak scale is the scale of electroweak
²⁷⁰ symmetry breaking. The Planck scale is the scale where the gravitational force
²⁷¹ is comparable in strength to the other forces. The Planck scale is where the SM
²⁷² breaks down, as there is not an experimentally verified theory of quantum gravity,
²⁷³ and at this scale gravity cannot be ignored (like it can at the electro-weak scale).

274 These scales differ by ~ 30 orders of magnitude. Understanding the difference
275 in these energy scales, may help explain the weakness of gravity at electroweak
276 scales, and possibly a QFT for gravity. (NB: This hierarchy can also be framed in
277 terms of the corrections to the Higgs mass, which depend on the UV cutoff scale -
278 where the SM is suppose to break, which is taken at the Planck scale. This leads
279 the quantum corrections to the Higgs mass to force the Higgs mass to 10^{18} TeV.)

280 These stark contrasts in scales may indicate that a more fundamental theory
281 exists. It is hoped that such a theory would explain and motivate some of the ad-
282 hoc features of the SM. In particular, there currently are no experimentally verified
283 explanations of why there are three generations of fermions, the values of the 19
284 SM parameters (6 quark masses, 3 charged lepton masses, 3 gauge couplings,
285 Higgs parameters (μ^2, λ)), the structure of the fermion representations, etc.

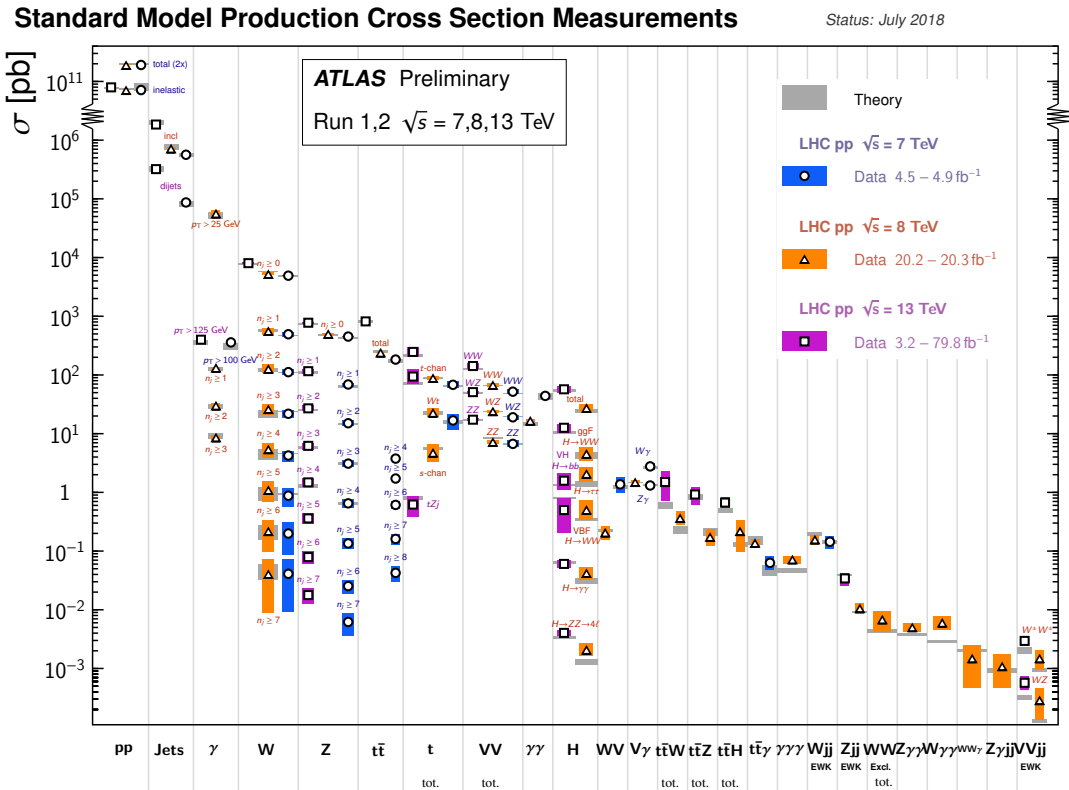


Figure 2.1: A comparison of cross section measurements at $\sqrt{s} = 7,8,13$ TeV from ATLAS compared to theoretical measurements. From Ref. [5]

²⁸⁶ **Chapter 3**

²⁸⁷ **New Physics Models with**
²⁸⁸ **Diboson Resonances**

²⁸⁹ **3.1 Randall Sundrum Bulk Model**

²⁹⁰ The electroweak-planck hierarchy may be explained by the existence of extra
²⁹¹ dimensions, like the 5D Randall Sundrum Bulk Model ([17], [2]). In this model,
²⁹² there is one extra warped spatial dimension, y , with a metric:

$$ds^2 = e^{-2k|y|} \eta_{\mu\nu} dx^\mu dx^\nu + dy^2 \quad (3.1)$$

²⁹³ where $e^{-k|y|}$ is the warp factor of the extra dimension, which is compactified on
²⁹⁴ a S^1/Z_2 orbifold (a.k.a. a circle where $y \rightarrow -y$). This can be visualized as every
²⁹⁵ point in space time having a line extending from it a distance L , representing
²⁹⁶ this fifth dimension. At the end of this line is the Planck brane. This fourth
²⁹⁷ spatial dimension separates two 4-D branes: Planck brane and TeV brane. We
²⁹⁸ live on the TeV brane, as shown in Figure 3.1. The Higgs field (and to a lesser
²⁹⁹ degree the top quark and graviton fields) is localized near the TeV Brane, while

300 the light fermion fields are localized more near the Planck brane. Fundamental
 301 parameters are set on the Planck brane. The warp factor may be scaled away from
 302 all dimensionless SM terms by field redefinitions. However, the only dimensionful
 303 parameter, $m_H^2 = v^2$ is rescaled by $\tilde{v} \sim e^{-kL} M_{Pl} \sim 1\text{TeV}$ for $kL \sim 35$, explaining
 304 why gravity is so weak on the TeV brane. Also, by localizing the light fermion
 305 fields near the Planck brane and top and graviton fields near the TeV brane, the
 306 light quarks will have smaller masses.

307 The two free parameters of this theory are M_{Pl} and k . Based on this RS Bulk
 308 model, all SM particles should have Kaluza-Klein (KK) excitations. In particular,
 309 the graviton would have KK excitations that prefer to decay to WW or ZZ, which
 310 is why this analysis searches for RS Gravitons.

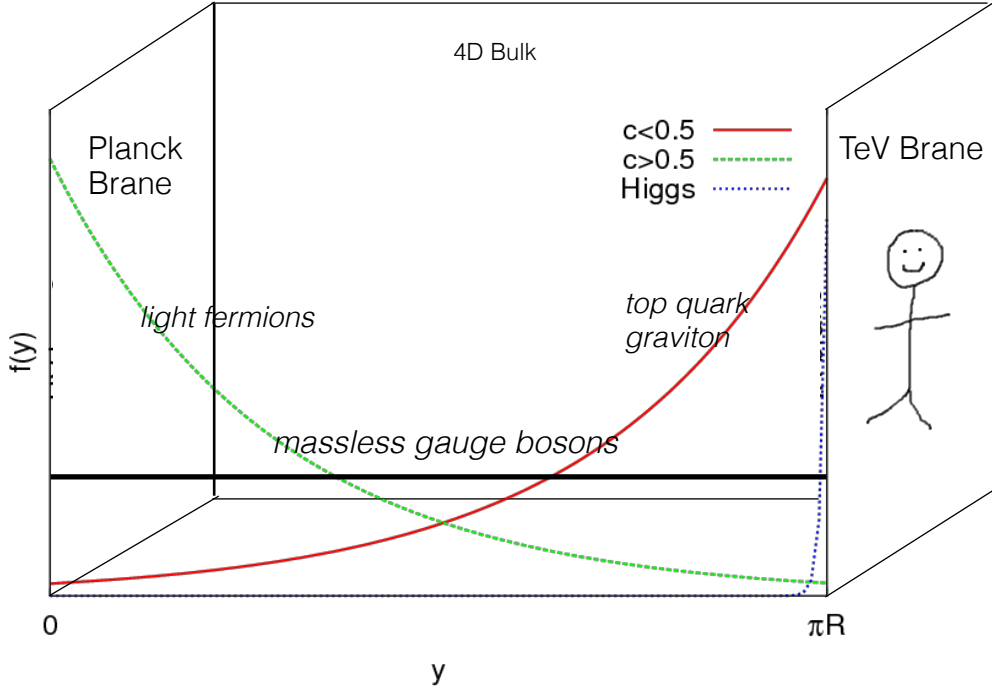


Figure 3.1: Cartoon of RS Bulk Model

311 3.2 Extended Scalar Sector

312 A further striking asymmetry of the SM is the simplicity of the scalar sector in
313 comparison to the boson and fermion sectors. To date, the scalar sector has only
314 one member, the Higgs boson. Therefore, it is natural to posit an extension to the
315 scalar sector. From a theoretical standpoint this could also help generate baryon
316 asymmetry through additional sources of CP violation. This analysis searches for
317 a simple extension to the scalar sector as proposed in Ref. [18]. The extended
318 scalar sector includes a real Higgs singlet (S) and complex $SU(2)_L$ doublet (Φ)
319 (the SM Higgs), where mass eigenstates are mixtures of the fields. S has a vev of
320 v and Φ has a vev of x . This then gives a Lagrangian of:

$$\mathcal{L} \supset (D^\mu \Phi)^\dagger D_\mu \Phi + \partial^\mu S \partial_\mu S - m^2 \Phi^\dagger \Phi - \mu^2 S^2 + \lambda_1 (\Phi^\dagger \Phi)^2 + \lambda_2 S^4 + \lambda_3 \Phi^\dagger \Phi S^2 \quad (3.2)$$

321 The mass eigenstates of the scalar sector are then mixtures of S and Φ and
322 the free parameters of the theory are m_H , $\sin \alpha$, and $\tan \beta = v/x$. The fields are
323 then given by:

$$\Phi \equiv \begin{pmatrix} 0 \\ \frac{\tilde{h}+v}{\sqrt{2}} \end{pmatrix} \quad (3.3)$$

324

$$S \equiv \frac{h' + x}{\sqrt{2}} \quad (3.4)$$

325 Diagonalizing the mass matrix leads to the mass eigenstates h (discovered
326 Higgs boson) and H (the physical particles):

$$\begin{pmatrix} h \\ H \end{pmatrix} = \begin{pmatrix} \cos \alpha & -\sin \alpha \\ \sin \alpha & \cos \alpha \end{pmatrix} \quad (3.5)$$

³²⁷ This suppressed h and H production and SM H couplings:

$$BR_{H \rightarrow SM} = \sin^2 \alpha \times \frac{\Gamma_{SM, H \rightarrow SM}}{\Gamma_{tot}} \quad (3.6)$$

³²⁸ Moreover, in the case that $m_H > m_h$, $H \rightarrow hh$ is possible. This further suppresses
³²⁹ $H \rightarrow VV/ff$. This search is most sensitive to $H \rightarrow WW$.

³³⁰ 3.3 Simple Standard Model Extensions

³³¹ The RS Bulk model is motivated by resolving the hierarchy problem. Ex-
³³² tending the Scalar sector is a natural space to look for new physics due to the
³³³ complexity of fermion and boson groups. There are many other interesting and
³³⁴ well motivated frameworks, but there is a lack of completely predictive models,
³³⁵ due to model flexibility (free parameters). Therefore it is hard for experimentalists
³³⁶ to know which theories to search for in data. However, as seen in [15], a "Simpli-
³³⁷ fied Model" approach may be taken. In the search for reasonably narrow width
³³⁸ particles, as in this search, the search is not sensitive to all the details and free
³³⁹ parameters of the theory. Generally such searches are only sensitive to the reso-
³⁴⁰ nance mass and its interactions. Therefore, a theory's Lagrangian may be reduced
³⁴¹ to only retain this information (mass parameters and couplings). Experimental
³⁴² results using this framework may then be reinterpreted in a given theory.

³⁴³ In the simplified approach, the new resonance searched for is represented as
³⁴⁴ a real vector field in the adjoint representation of $SU(2)_L$ with vanishing hyper-
³⁴⁵ charge. This results in one neutral and two charged bosons. Defined as:

$$V^\pm = \frac{V_\mu^1 \mp iV_\mu^2}{\sqrt{2}} \quad (3.7)$$

³⁴⁶

$$V_\mu^0 = V_\mu^3 \quad (3.8)$$

³⁴⁷ The SM Lagrangian is then augmented with the additional terms:

$$\mathcal{L} \supset -\frac{1}{4}D_{[\mu}V_{\nu]}^a D^{[\mu}V^{\nu]}_a + \frac{m_V^2}{2}V_\mu^a V^{a\mu} + ig_V c_H V_\mu^a H^\dagger \tau^a \overset{\leftrightarrow}{D}^\mu H + \frac{g^2}{g_V} c_F V_\mu^a J_F^{\mu a} \quad (3.9)$$

³⁴⁸ In order the terms represent: the kinetic, V mass, Higgs- V interaction, and
³⁴⁹ V -left-handed fermion interaction terms. Phenomenologically the three physical
³⁵⁰ particles this predicts are degenerate, where V couples most strongly to VV , via
³⁵¹ the g_V coupling factor. The dominant production modes are DY and VBF.

³⁵² Two versions of HVT are considered, Model A and B. Model A is a weakly
³⁵³ coupled model where $g_V \sim 1$, like the extended gauge symmetry discussed in Ref
³⁵⁴ . [16]. Model B is a strongly coupled model, where $1 < g_V < 4\pi$. The width
³⁵⁵ of the resonance grows with g_V so for this narrow resonance search only g_V is
³⁵⁶ chosen to be less than 6 (so $\Gamma/M < 10\%$). More precisely, the coupling of these
³⁵⁷ resonances to fermions scales as $g_f = g^2 c_F/g_V$, where g is the SM $SU(2)_L$ gauge
³⁵⁸ coupling and c_F is the free parameter (expected to be of order 1 for Model A and
³⁵⁹ B). This then means that for Model B the coupling to fermions is more suppressed
³⁶⁰ than for Model A, leading to a smaller DY production rate and BR to fermionic
³⁶¹ final states. The coupling of V to SM bosons scales as $g_H = g_V c_H$, where c_H is
³⁶² a free parameter on the order of 1 for Model A and B. So for small values of g_V
³⁶³ (i.e. Model A - weakly coupled theories) the BR to gauge bosons is smaller than
³⁶⁴ for Model B. So weakly coupled vectors have large production cross sections and
³⁶⁵ decay prominently to leptons or jets, while strongly coupled vectors are produced
³⁶⁶ less and decay predominantly to gauge bosons.

³⁶⁷ Vectors in Model A and B are generally produced via quark-anti-quark annihi-
³⁶⁸ lation. The more rare production via vector-boson-fusion is considered by setting
³⁶⁹ $g_H = 1$ and $g_F = 0$. In Model B diboson final states are enhanced as stated
³⁷⁰ previously due to g_H and moreover the BR to WZ , WH , WW , and ZH are the

³⁷¹ same.

³⁷² In summary, V couples most strongly to left-handed fermions and VV dependent on g_V .

Part II

374

Experimental Setup

375

³⁷⁶ **Chapter 4**

³⁷⁷ **LHC**

³⁷⁸ The Large Hadron Collider (LHC) is the highest-energy particle collider in the
³⁷⁹ world. It was designed to expand the frontier of high energy particle collisions in
³⁸⁰ energy and luminosity. This enables LHC experiments to test the Standard Model
³⁸¹ and search for new physics at higher energies than tested with previous colliders.
³⁸² Collisions at higher energies not only produce more massive particles but also
³⁸³ more weakly interacting particles. Fig 4.1 shows production cross sections for
³⁸⁴ various processes at hadron colliders. The rate for electroweak physics processes
³⁸⁵ including W and Z scale with the center-of-momentum energy, \sqrt{s} .

³⁸⁶ The LHC consists of a 26.7 km (17 miles) ring, approximately 100 m un-
³⁸⁷ derground, outside Geneva, Switzerland. Counter-circulating proton (and occa-
³⁸⁸ sionally heavy ions) beams collide inside four experiments along the beam line:
³⁸⁹ ATLAS, CMS, LHCb, ALICE. ATLAS and CMS are general purpose detectors de-
³⁹⁰ signed to explore the high energy frontier. LHCb is designed to study the physics
³⁹¹ of b -quarks. ALICE specializes in studying heavy ion collisions.

proton - (anti)proton cross sections

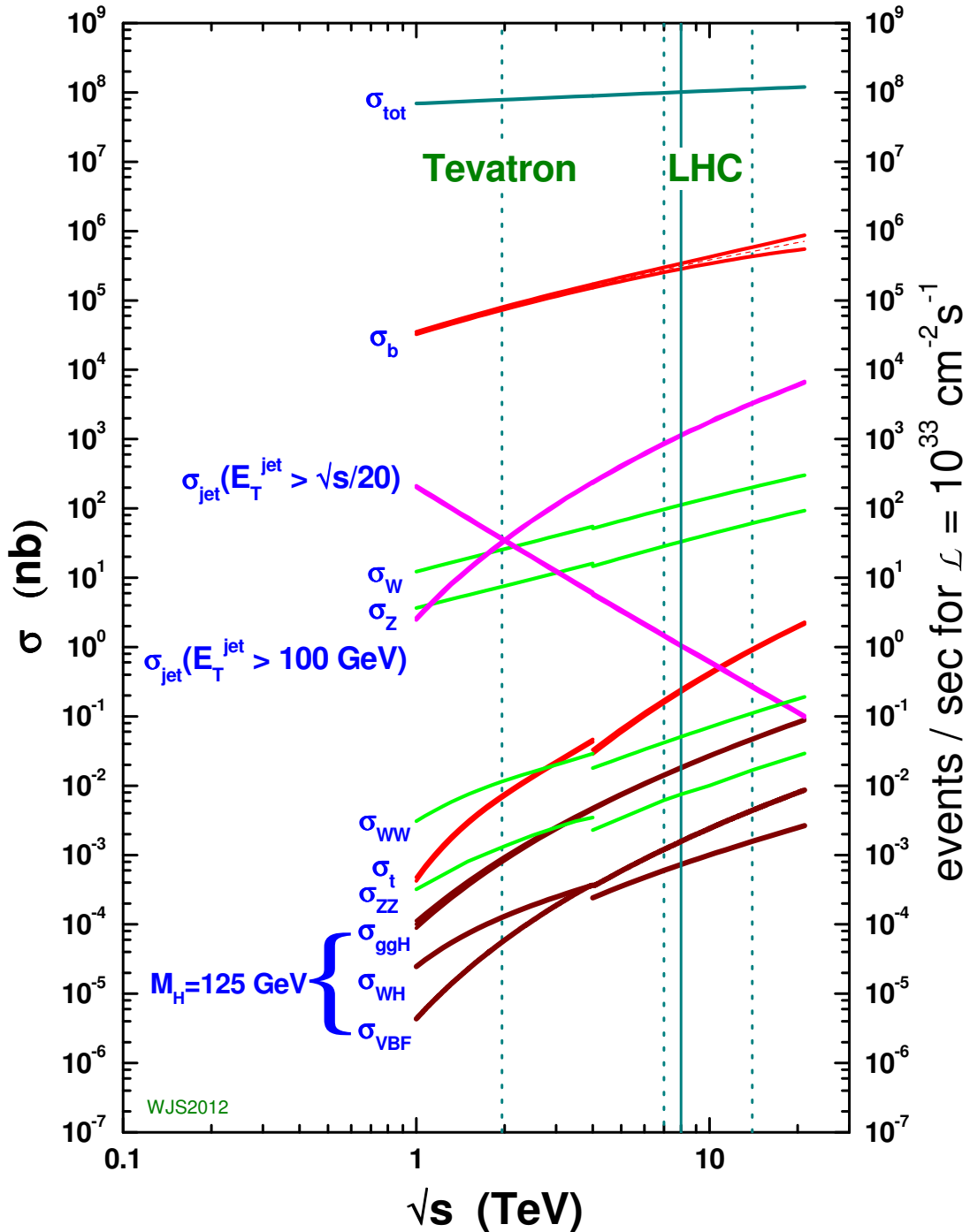


Figure 4.1: Scaling of cross sections with \sqrt{s} . Natasha: write more here

392 The first proton beams circulated in September, 2008. Nine days later an elec-
393 trical fault lead to mechanical damage and liquid helium leaks in the collider. This
394 incident delayed further operation until November 2009, when the LHC became
395 the world's highest energy particle collider, at 1.18TeV per beam. This first oper-
396 ational run continued until 2013, reaching 7 and 8 TeV collision energies. During
397 this run a particle with properties consistent with the Standard Model Higgs bo-
398 son was discovered. The next run began after a two year shutdown after upgrades
399 to the LHC and experiments. This run lasted from 2013 to 2018 reaching 13 TeV
400 collision energies. This analysis uses data from the second operational run.

401 **4.1 LHC Layout and Design**

402 The layout of the LHC is shown in Figure 4.2. The red and blue lines in the
403 figure represent the counter-circulating proton beams. The LHC is divided into
404 eight octants. Octant 4 contains the RF cavities that accelerate the protons and
405 octant 6 contains the beam dump system. Octants 3 and 7 house the collimation
406 systems for beam cleaning. The beams collide inside the four aforementioned
407 experiments. Each octant contains a curved and straight section. The LHC
408 magnets are built with NbTi superconductors cooled with super-fluid Helium to
409 2K, creating a 8.3T magnetic field to bend the proton beams.

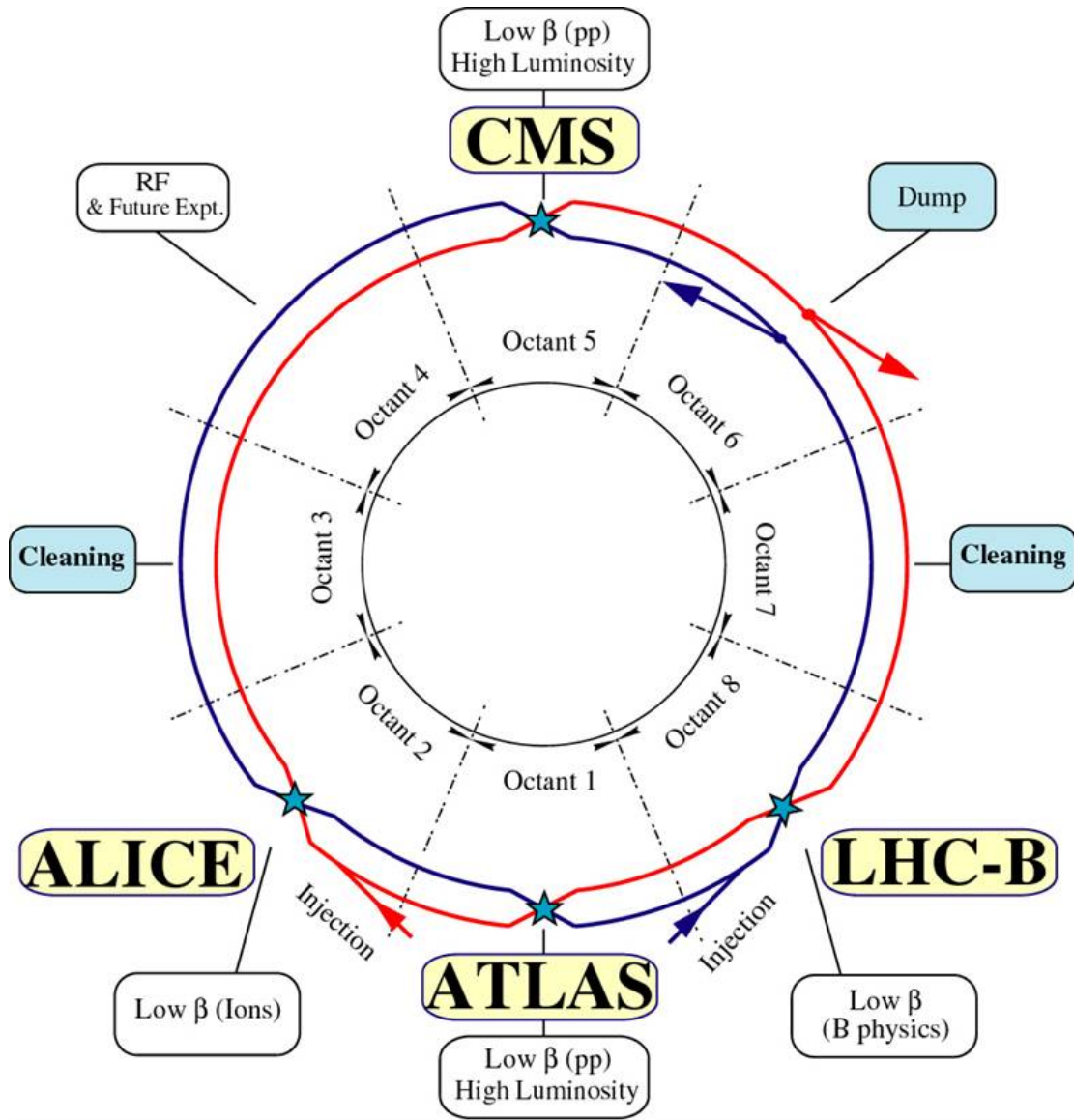
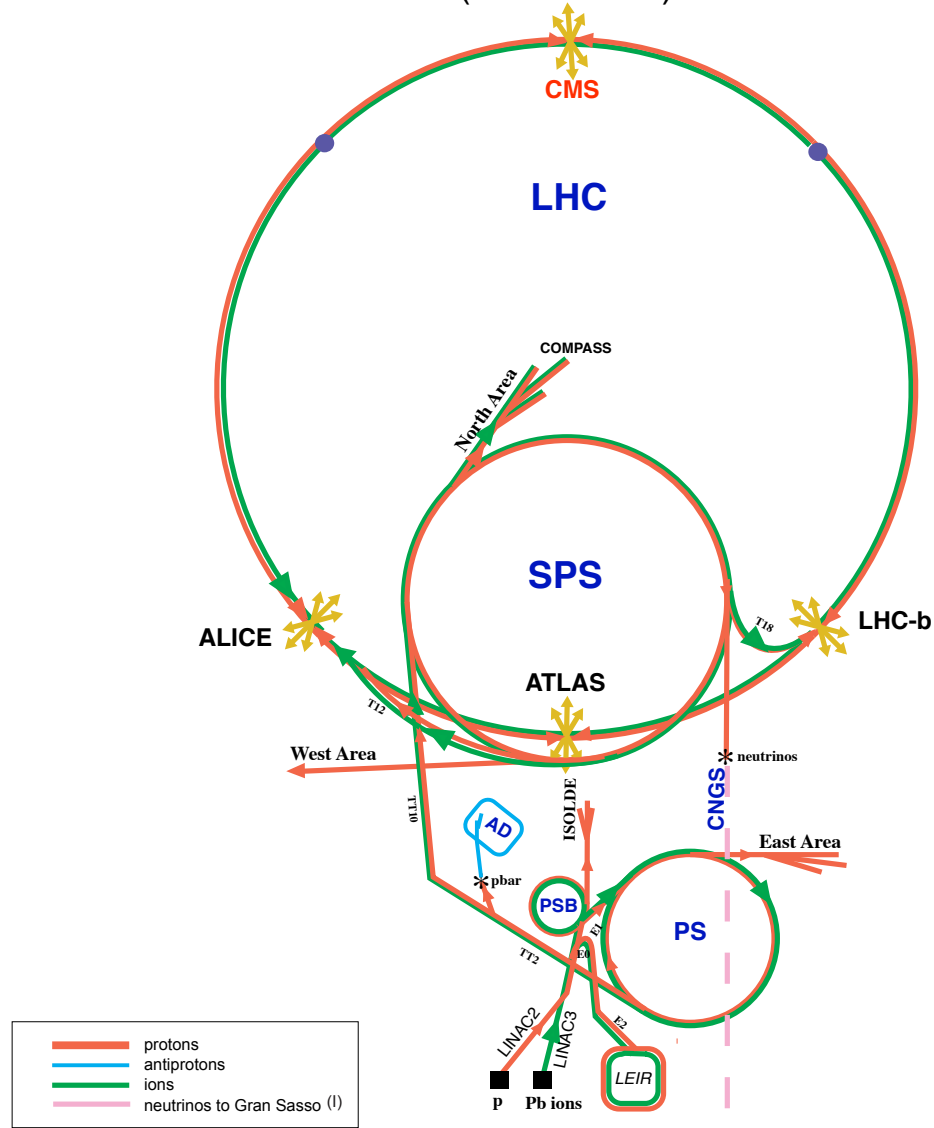


Figure 4.2: LHC Layout. Natasha write more

410 Four sequential particle accelerators are used to accelerate protons from rest
 411 as shown in Figure 4.3. First, Hydrogen gas is ionized to produce protons which
 412 are then accelerated to 50 MeV using Linac 2, a linear accelerator. The result-
 413 ing proton beam is then passed to three circular particle accelerators: Proton
 414 Synchrotron Booster, Proton Synchrotron, and Super Proton Synchrotron (SPS),

415 accelerating protons to 1.4, 25, and 450 GeV, respectively. Once the protons exit
416 the SPS, they are injected into the LHC at octant 2 and 8. Each proton bunch
417 contains $\sim 10^{11}$ protons. The spacing between bunches is 25 ns, which means
418 each beam contains 3564 bunches. However, some bunches are left empty due
419 to injection and safety requirements, yielding 2808 bunches per beam. Once the
420 proton beams are injected they are accelerated to 13 TeV.

CERN Accelerators (not to scale)



LHC: Large Hadron Collider

SPS: Super Proton Synchrotron

AD: Antiproton Decelerator

ISOLDE: Isotope Separator OnLine DEvice

PSB: Proton Synchrotron Booster

PS: Proton Synchrotron

LINAC: LINear ACcelerator

LEIR: Low Energy Ion Ring

CNGS: Cern Neutrinos to Gran Sasso

Rudolf LEY, PS Division, CERN, 02.09.96
Revised and adapted by Antonella Del Rosso, ETT Div.,
in collaboration with B. Desforges, SL Div., and
D. Manglunki, PS Div. CERN, 23.05.01

Figure 4.3: LHC Accelerator. Natasha write more

421 As many new physics models predict cross-sections below the weak scale it was
422 important to design the LHC to be capable of collecting enough data, by running
423 in high luminosity conditions. The machine luminosity depends only on beam
424 parameters:

$$L = \frac{N_p^2 f}{4\epsilon\beta^*} F \quad (4.1)$$

425 where N_p is the number of protons per bunch, f is the bunch crossing frequency,
426 ϵ is the transverse beam emittance, β^* is the amplitude function at the collision
427 point, and F is the geometric luminosity reduction factor due to the beams crossing
428 at an angle (rather than head-on).

429 **Chapter 5**

430 **The ATLAS Detector**

431 The ATLAS detector measures the position, momentum and energy of parti-
432 cles produced in the proton collisions by using magnetic fields, silicon detectors,
433 sampling calorimeters, and gaseous wire detectors. It is located approximately
434 100 m underground at Point-1 around the LHC beam line and weighs 7000 metric
435 tons. The detector is 46 m long, 25 m high, 25 m wide as shown in Figure 5.2.
436 The detector can be divided into three subsystems: the Inner Detector (ID), the
437 Calorimeters, and the Muon Spectrometer (MS). Figure 5.3 shows an overview of
438 how different particles interact in the detector.

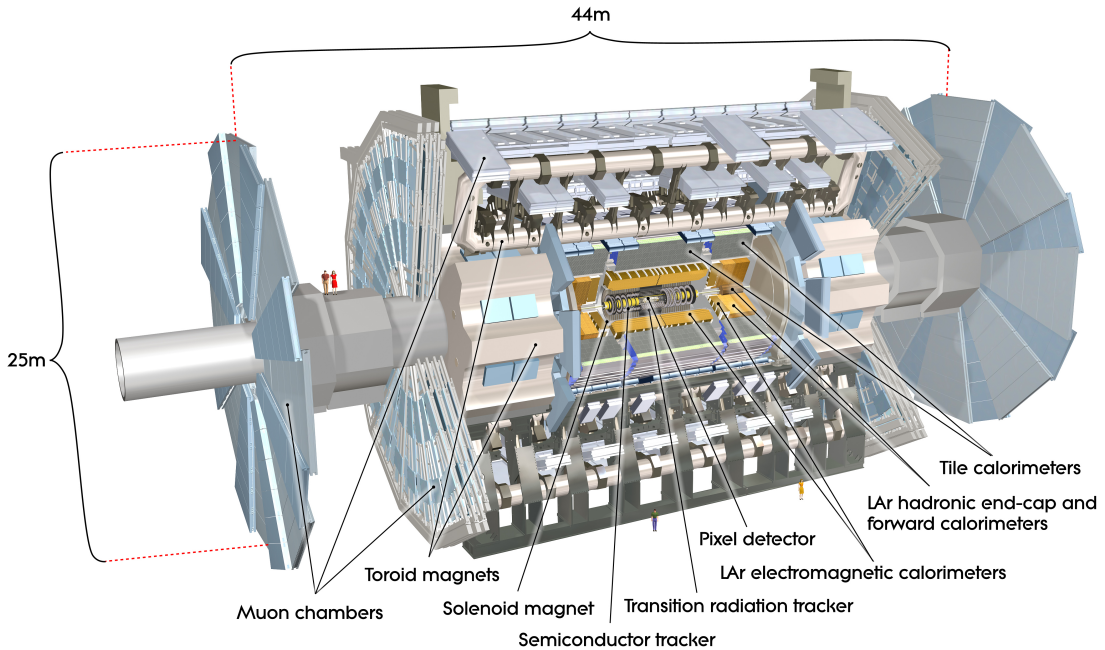


Figure 5.1: Big picture layout of ATLAS detector. Natasha: write more

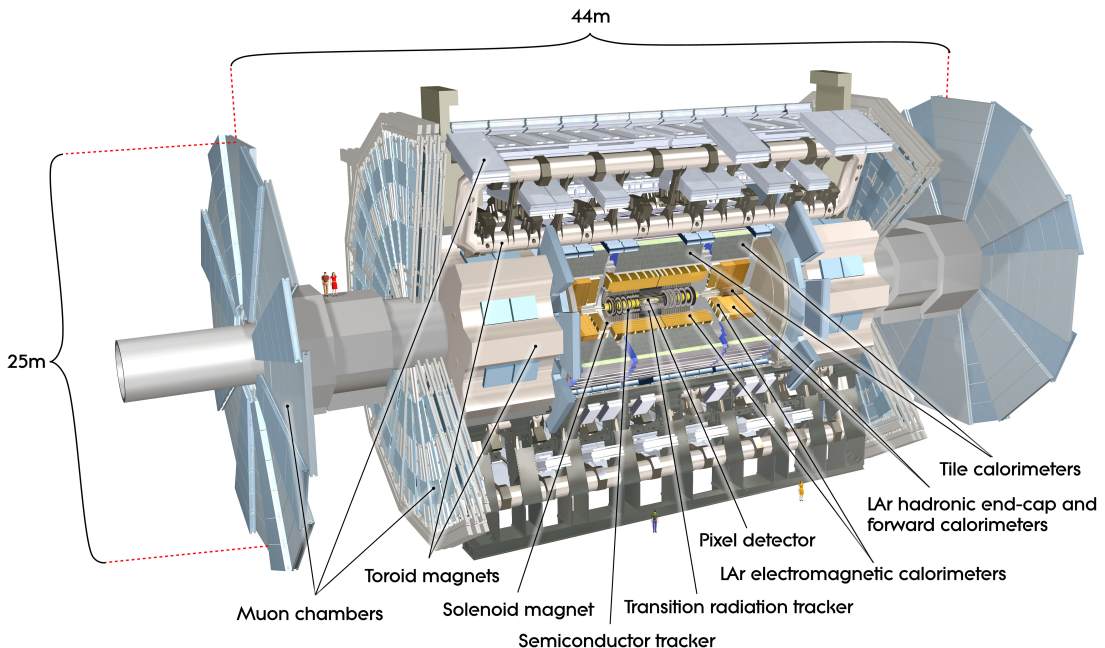


Figure 5.2: Big picture layout of ATLAS detector. Natasha: write more

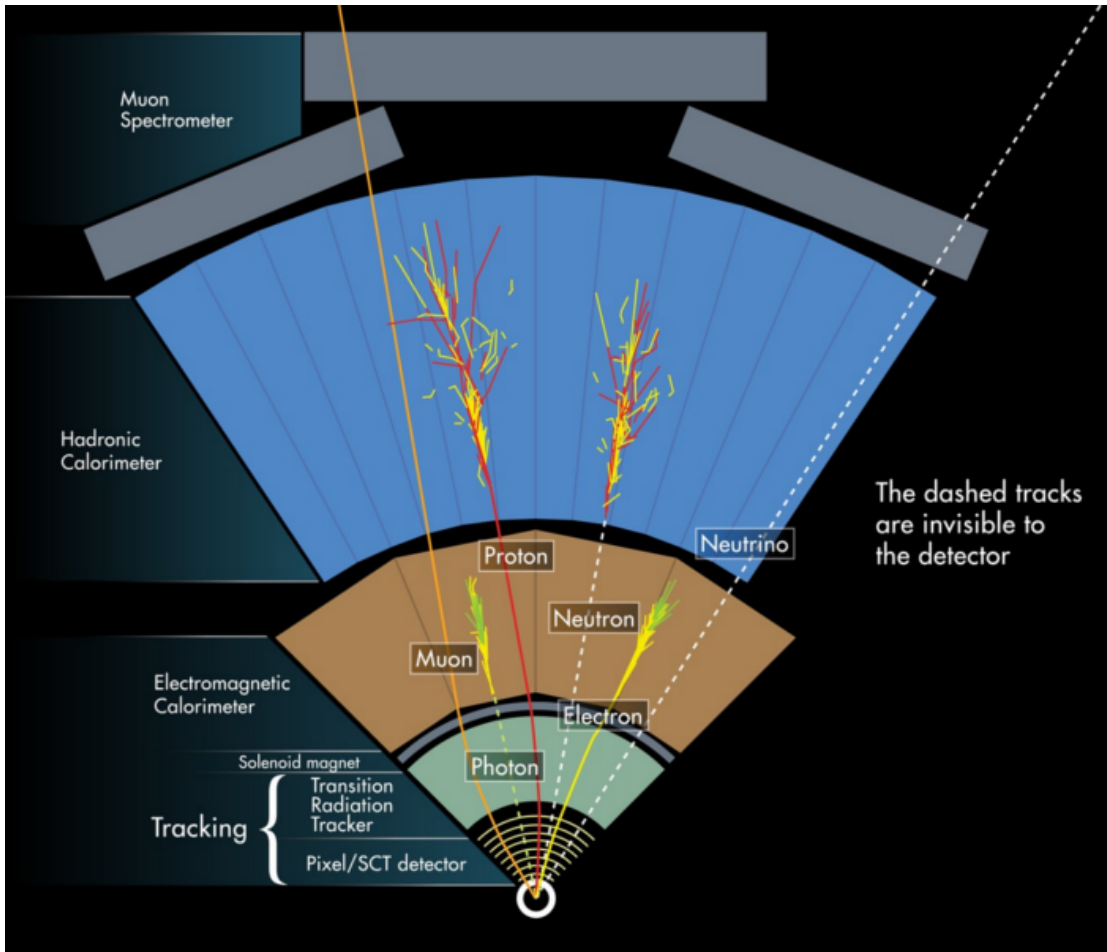


Figure 5.3: A simplified schematic of how different particles interact and are detected within ATLAS.

439 5.1 Coordinate System

440 The trajectory of particles within ATLAS is measured relative to the nominal
 441 interaction point. The z -axis points along the beam line, such that when the
 442 LHC is viewed from above, the counter-clockwise circulating beam points along
 443 the positive- z direction. The $x - y$ plane is transverse to the beam line, with the
 444 positive x -axis pointing towards the center of the LHC ring. The positive y -axis
 445 points vertically upward. The azimuthal angle, ϕ , is the angular distance about

446 the z -axis, with $\phi = 0$ along the x -axis. The polar angle from the z -axis is denoted
447 as θ . However, this quantity is not Lorentz invariant, like rapidity, $y = \frac{1}{2} \ln \frac{E+p_z}{E-p_z}$,
448 where E is the energy of the particle considered, and p_z , is it's momentum along
449 the z -axis. Pseudo-rapidity is preferred as $\Delta\eta$ is invariant under boosts along z
450 and particle production is approximately invariant under η . For massless particles,
451 rapidity and a related quantity, pseudorapidity, are the identical. The pseudora-
452 pidity is defined as: $\eta = -\ln \tan(\frac{\theta}{2})$. This quantity is preferred as it is purely a
453 geometric quantity, independent of particle energy. Angular separation between
454 particles in ATLAS are given by $\Delta R = \sqrt{\Delta\eta^2 + \Delta\phi^2}$. The distance from the
455 beamline is given by $r = \sqrt{x^2 + y^2}$

456 5.2 Inner Detector

457 The Inner Detector (ID) was designed to identify and reconstruct vertices,
458 distinguish pions from electrons, and measure the momentum of charged particles.
459 The ID uses three different technologies for particle reconstruction: the Pixel
460 Detector, Semiconductor Tracker (SCT), and the Transition Radiation Tracker
461 (TRT), shown in Figure 5.4 and 5.5. The entire ID is immersed in a 2T solenoidal
462 magnetic field parallel to the $+z$ -axis, causing charged particles to bend in the
463 transverse-plane, allowing particle momentum measurements.

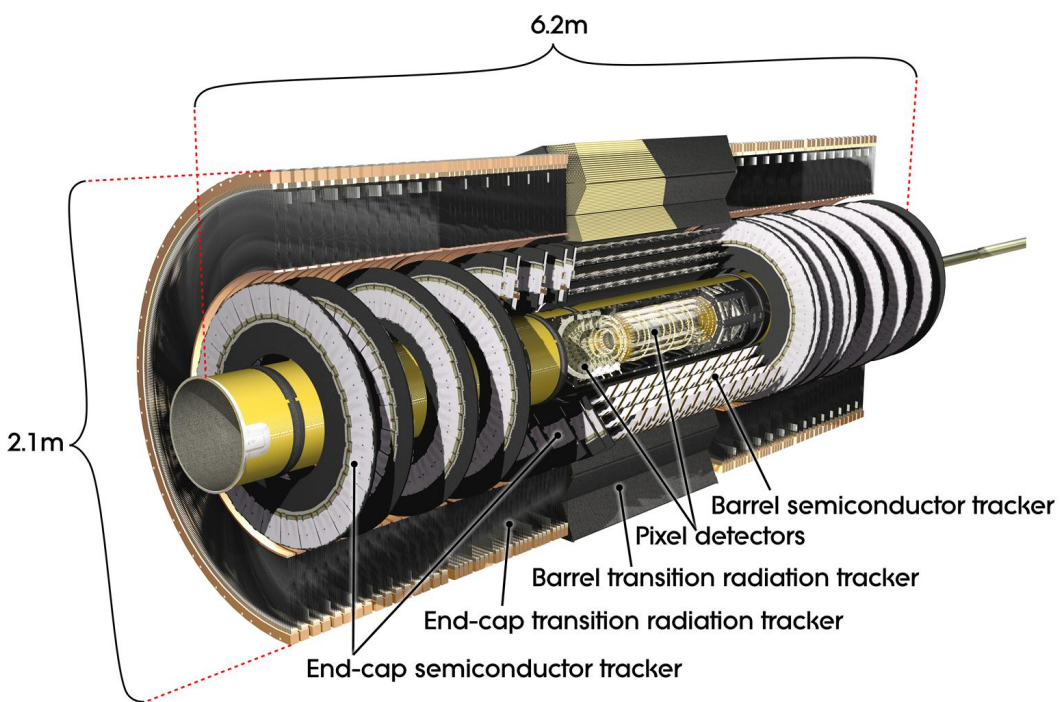


Figure 5.4: Layout of ATLAS Inner Detector

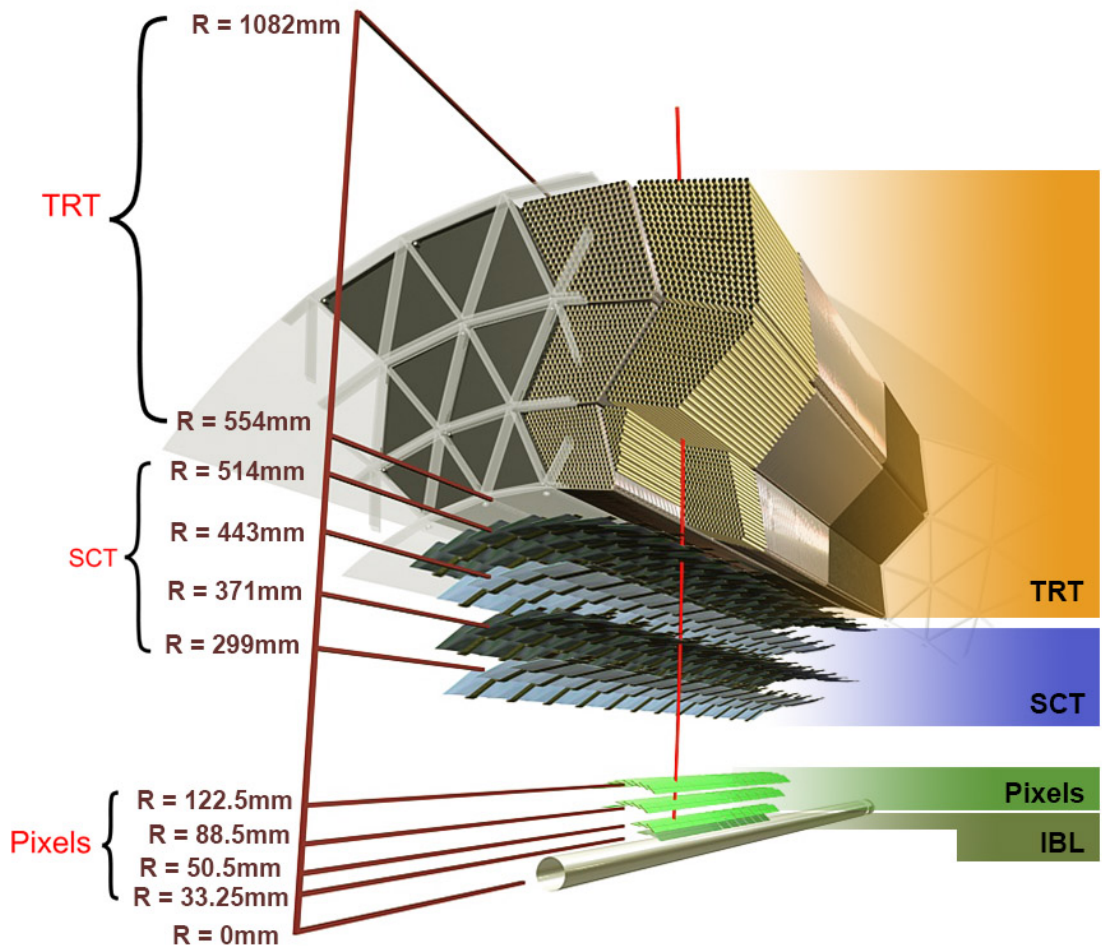


Figure 5.5: Layout of ATLAS ID Barrel System.

464 **5.2.1 Pixel Detector**

465 The pixel detector consists of four barrel layers between $r = 32.7$ and 122.5
466 mm, extending to $|z| = 400.5$ mm. The remaining detectors are arranged in bar-
467 rels and forward and backward rings. The innermost pixel barrel, the Insertable
468 b-Layer (IBL), only extends to $|z| = 332$ mm. The pixel detectors closer to the
469 beam line (larger η values) consists of six parallel cylindrical rings of pixel de-
470 tectors transverse to the beam line. The entire pixel detector consists of 1744
471 identical pixel sensors each with 46080 readout channels, totaling about 80 mil-
472 lion individual pixels. Most of the pixel sensors are $50 \times 400 \mu\text{m}^2$. Each pixel has
473 a position resolution of $14 \mu\text{m}$ in ϕ and $115 \mu\text{m}$ in the z direction.

474 **5.2.2 Semiconductor Tracker**

475 The SCT is located outside the pixel detector and has the same barrel and
476 endcap geometry as the pixel detector. SCT sensors are $80 \mu\text{m} \times 12$ cm with
477 a $80 \mu\text{m}$ strip pitch. In the barrel the strips are parallel to the z -axis and are
478 segmented in ϕ . In the endcaps, the strips extend radially. Sensors are grouped in
479 modules containing two layers of strips rotated 40 mrad with respect to each other.
480 This offset allows for the two-dimensional position of a track to be determined by
481 identifying the crossing point of the strips that registered a hit. SCT modules
482 measure tracks with an accuracy of $17 \mu\text{m}$ in $r - \phi$ and $580 \mu\text{m}$ in $z(r)$ in the
483 barrel (end-cap) region.

484 **5.2.3 Transition Radiation Tracker**

485 The transition radiation tracker (TRT), enveloping the SCT, is a gaseous
486 straw-tube tracker mainly used for electron/pion track separation. Each straw
487 is 4 mm in diameter and filled with a Xe- CO_2 - O_2 gas mixture. An anode wire at

488 the center of the straw is held at ground potential, while the walls of the straw
489 are kept at -1.4kV. When a charged particle passing through the TRT ionizes the
490 gaseous mixture, the resulting ions form an avalanche on the anode wire with a
491 gain of $\sim 10^4$. The signal from the anode wire is then digitized and discriminated.
492 Signals passing a low threshold cutoff are used to distinguish noise from tracks.
493 Signals passing a high threshold cutoff are sensitive to transition radiation (TR).
494 TR photons are emitted when charged particles pass between materials with dif-
495 ferent dielectric constants. The probability that a charged particle with energy E
496 and mass m passing between two materials emits a TR photon in the keV range
497 is proportional to $\gamma = E/m$. In the TRT straws these often then convert via the
498 photoelectric effect, causing a large avalanche triggering the high-threshold. Since
499 electrons have a smaller mass than pions, electron tracks are more likely to trig-
500 ger the high threshold. This then provides discrimination between electrons and
501 charged hadrons.

502 The barrel region of the TRT extends from $r = 563\text{-}1066$ mm and $|z| < 712$
503 mm. Barrel Straws are 144 cm long (divided $\sim \eta \approx 0$) and orientated parallel to
504 the beam direction. End-cap straws extend radially and are 37 cm long. There
505 are 53,544 straws in the barrel and 160,000 straws in the end-caps. Radiator mats
506 of polypropylene/polyethylene fibers in the barrel are aligned perpendicular to the
507 barrel straws (with holes for the straws to pass through). In the end-cap region,
508 radiator foils are layered between the radial TRT straws.

509 The arrival time of the signal pulse is sensitive to the distance between the
510 charged particle track and the anode wire and allows for a hit resolution of $130\mu\text{m}$.
511 The TRT extends to $|\eta| = 2.0$ and provides about 36 hits per track.

512 5.3 Calorimeters

513 The ATLAS electromagnetic and hadronic calorimeters (EMC and HCAL,
514 respectively) absorb and measure the energy of high energy hadrons, photons,
515 and electrons with $|\eta| < 4.9$. Both systems use sampling calorimeters which
516 consist of alternating layers of dense absorbing and active layers. In the absorbing
517 layer particles interact and lose energy, creating showers. These showers are then
518 detected and measured in the active layer. The amount of charge measured in the
519 active material scales with the energy of the incident particle, and thus provides a
520 measurement of the particle's energy. An overview of the layout of the calorimeter
521 system is shown in Figure 5.6.

522 The EMC measures and contains the energy of electromagnetically interacting
523 particles. It consists of layered accordion-shaped Lead absorber plates and elec-
524 trodes immersed in liquid Argon with 170k channels.. Using accordion-shaped
525 electrode and absorbers ensures ϕ symmetry and coverage. The EMC is com-
526 posed of a barrel part ($|\eta| < 1.475$), two end-caps ($1.375 < |\eta| < 3.2$), and a
527 presampler ($|\eta| < 1.8$). The presampler, containing only liquid Argon, corrects
528 for upstream energy losses of electrons and photons. The EMC barrel is segmented
529 into three layers. The first layer has finest segmentation with readout cells ex-
530 tending $\Delta\eta \times \Delta\phi = 0.025/8 \times 0.1$. This provides a precise shower measurements
531 used to separate prompt photons from $\pi^0 \rightarrow \gamma\gamma$ decays. The second layer has
532 coarser segmentation and is approximately 16 radiation lengths long. A radiation
533 length is the average distance an electron travels before losing all but $1/e$ of its
534 energy to bremsstrahlung. The last layer is the most coarse and measures the tail
535 of the electromagnetic shower. A schematic of the ECAL is shown in Figure 5.7.

536 The hadronic calorimeter located outside the EMC and is used to contain
537 and measure the energy of hadronically interacting particles. It consists of a tile

538 calorimeter (TileCal), hadronic end-cap calorimeter (HEC), and liquid Argon for-
 539 ward calorimeter (FCAL). TileCal is located behind the LAr EMC and uses steel
 540 absorbers and liquid Argon as the active material. TileCal consists of three barrel
 541 layers in the central and forward regions, extending up to $|\eta| < 1.7$. Photons
 542 generated from hadronic interactions are collected via wavelength-shifting fibers
 543 connected to photomultiplier tubes, as shown in Figure 5.8. The HEC lies behind
 544 the EMC endcap wheels. It uses copper absorbers and liquid Argon as the active
 545 material and covers $1.5 < |\eta| < 3.2$. Finally, the FCAL covers $3.1 < |\eta| < 4.9$
 546 and consists of three modules all using liquid Argon as the active material. The
 547 first module uses copper absorber and was designed for electromagnetic measure-
 548 ments. The second and third modules consist of tungsten absorber and are used
 549 to measure the kinematics of hadronically interacting particles. A schematic of
 550 the HCAL is shown in Figure 5.8.

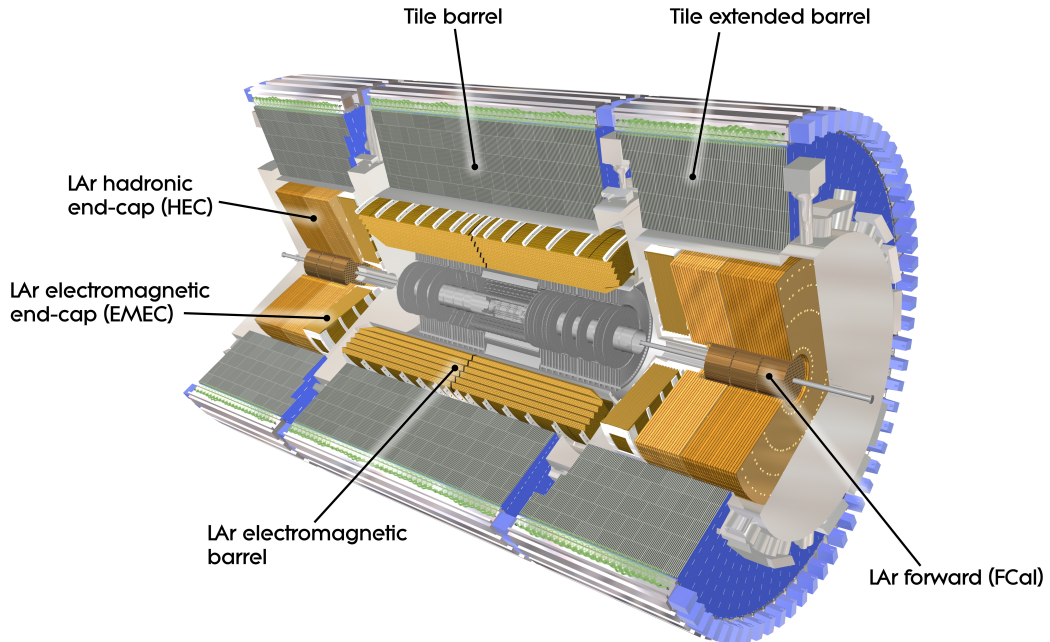


Figure 5.6: Overview of ATLAS electromagnetic and hadronic calorimeters.

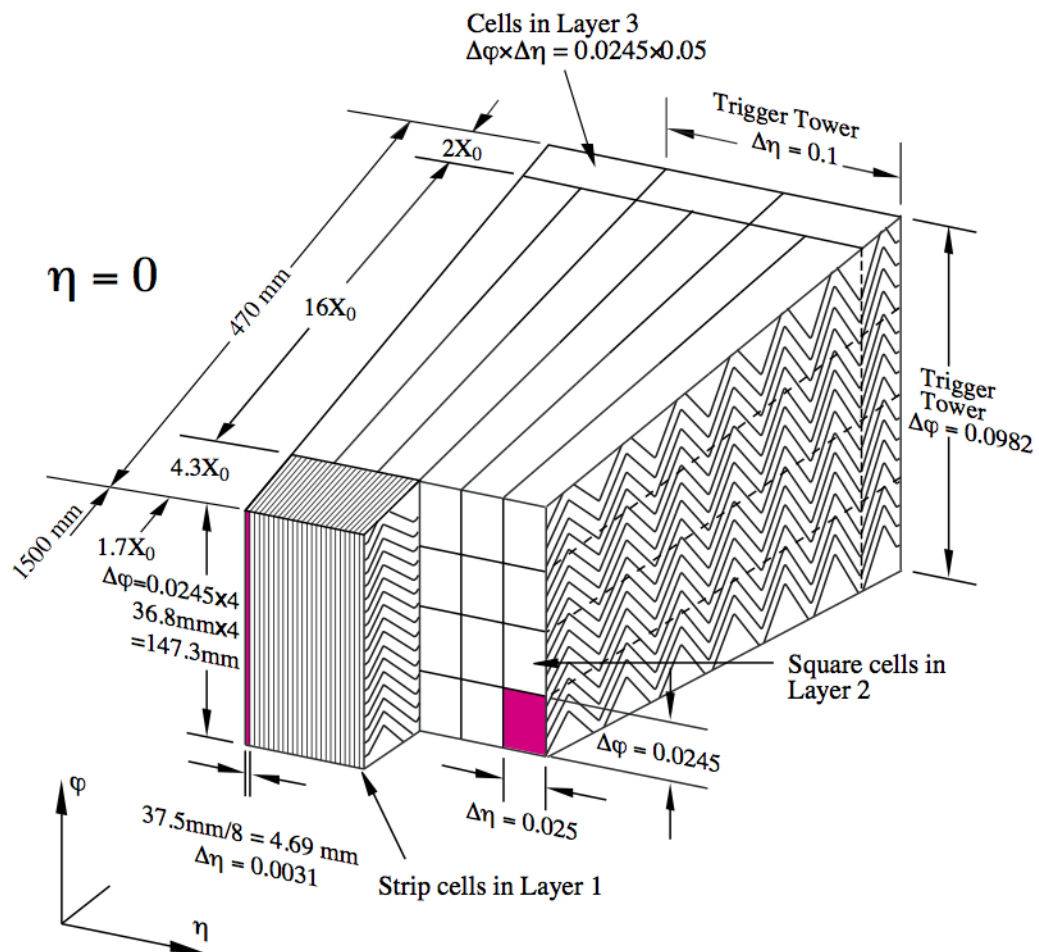


Figure 5.7: Schematic of ECAL.

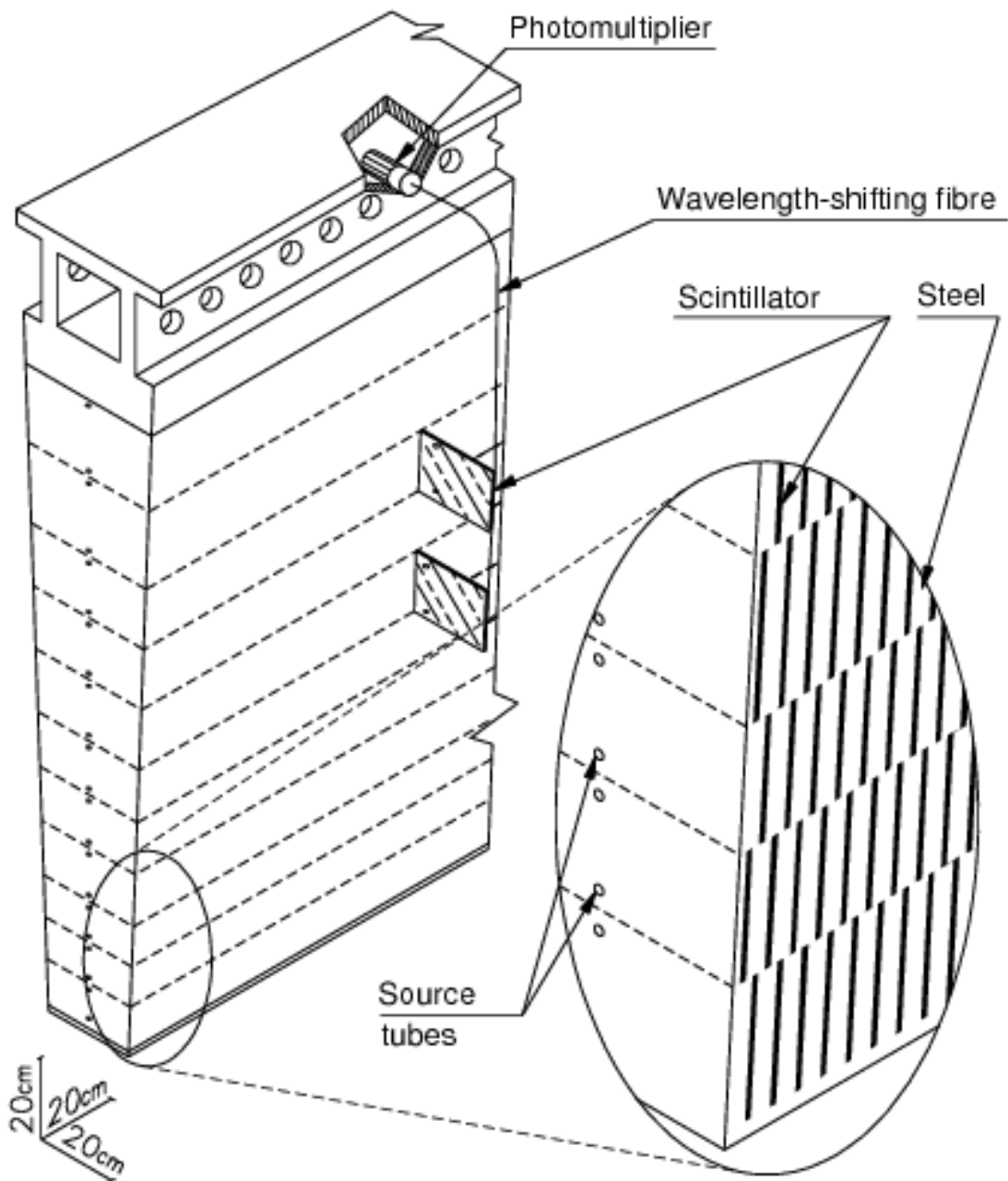


Figure 5.8: Schematic of HCAL.

551 The energy resolution of the calorimeter subsystems are:

552 $\frac{\sigma_E}{E} = \frac{10\%}{\sqrt{E}} \oplus 0.7\% \text{ EMC}$

553 $\frac{\sigma_E}{E} = \frac{50\%}{\sqrt{E}} \oplus 3\% \text{ hadronic barrel}$

554 $\frac{\sigma_E}{E} = \frac{100\%}{\sqrt{E}} \oplus 10\% \text{ hadronic end-cap}$

555

5.4 Muon Spectrometer

556 The muon spectrometer (MS) is the outermost detector system in ATLAS.

557 Muons with a $p_T > 4$ GeV are energetic enough to reach the MS. To measure the
558 momentum of these muons barrel and end-cap toroid magnets are used covering
559 $|\eta| < 1.4$ and $1.6 < |\eta| < 2.7$. For $1.4 < |\eta| < 1.6$, a combination of the barrel
560 and end-cap toroidal magnetic fields bend muon trajectories. The detector in the
561 barrel region form three concentric rings at $R = 5, 7.5, 10$ m and are segmented
562 in ϕ to accommodate the magnets. The end-cap region consists of three circular
563 planes perpendicular to z and located at $|z| = 7.4, 14, 21.5$ m from the interaction
564 region. An additional detector at $|z| = 10.8$ m covers the transition region between
565 the barrel and end-cap.

566 The MS readout consists of four subsystems: Monitored Drift Tubes (MDT),
567 Cathode Strip Chambers (CSC), Resistive Plate Chambers (RPC), and Thin Gap
568 Chambers (TGC). The first two subsystems are used primarily for measuring
569 muon track parameters, while the RPC and TGC subsystems are used for muon
570 triggering. A schematic of this system is shown in Figure 5.9.

571 The MDT subsystem consists of precision tracking chambers for $|\eta| < 2.7$,
572 except for the inner most end-cap layer ($2.0 < |\eta| < 2.7$), where CSCs are used.
573 The basic unit of MDT chambers are thin walled Aluminum tubes with a diameter
574 of 3 cm and length of 0.9-6.2 m. These tubes are filled with a mixture of Ar-CO₂
575 gas with a 50μm W-Rn wire running down the center of the tube, which is kept at

576 3080 V. Since the maximum drift time of these chambers is ~ 700 ns, they are not
577 used for triggering. MDT chambers consist of 3-4 layers of tubes mounted on a
578 rectangular support system, as seen in Figure 5.10, orientated along ϕ to measure
579 the coordinate in the bending plane of the magnetic field with a resolution of 35
580 μm .

581 The MDT subsystem can only handle hit rates below $150\text{Hz}/\text{cm}^2$. For this
582 reason, CSCs are used in the innermost end-cap layer where hit rates are larger.
583 CSCs can handle hit rates up to $1000\text{Hz}/\text{cm}^2$. CSC are multiwire proportional
584 chambers. These chambers are filled with a Ar- CO_2 gas mixture and evenly spaced
585 wires kept at 1900 V. These wires are orientated in the radial direction but not
586 read out. Instead on one side of the cathode are copper strips parallel to the wires,
587 measuring η , while on the other side of the cathode are strips parallel to the wires
588 measuring ϕ . The width between strips is approximately 1.5 mm providing a
589 resolution of 60 μm in the bending-plane and 5 mm in the non-bending plane.

590 Since the CSC and MDT systems do not have prompt timing signals, the RPC
591 and TGC systems are used for triggering. The RPC system is used in the barrel
592 region ($|\eta| < 1.05$). RPC consist of two parallel resistive plates separated by a 2
593 mm insulated spacer with 100 mm spacing kept at 9.8 kV, as shown in Figure 5.11.
594 A gaseous mixture of $\text{C}_2\text{H}_2\text{F}_4$, C_4H_{10} , and SF_6 fills the space between the two
595 plates. Metallic strips on the outer faces of the plates are used to read out signals
596 produced by the gas ionizing. The middle barrel layer consists of two layers of
597 RPCs on either side of the MDT layer and one layer on the outermost MDT
598 layer. Each layer contains two orthogonal sets of metallic strips providing η and
599 ϕ measurements. The timing resolution of RPCs is 1.5 ns, and therefore may be
600 used to identify bunch crossings.

601 Finally, the TGCs are used in the end-cap regions and are primarily used to

602 provide L1 trigger decisions and ϕ measurements. TGCs are multi-wire propor-
 603 tional chambers consisting of arrays of gold-coated tungsten wires placed between
 604 two cathode planes. These wires are separated by 1.8 mm and cathodes are 1.4 mm
 605 from the wires. Orthogonal to the wires, on the opposite side of the cathode plane
 606 are copper strips held at 2900 V. The chambers are filled with a mixture of CO_2
 607 and n-pentane gas, the latter acts as a quenching gas to prevent avalanches initi-
 608 ated by secondary γ -rays from the primary avalanche. Figure 5.12 is a schematic
 609 of a TGC. The timing resolution of TGCs is less than 25 ns and therefore they
 610 are used for bunch crossing measurements.

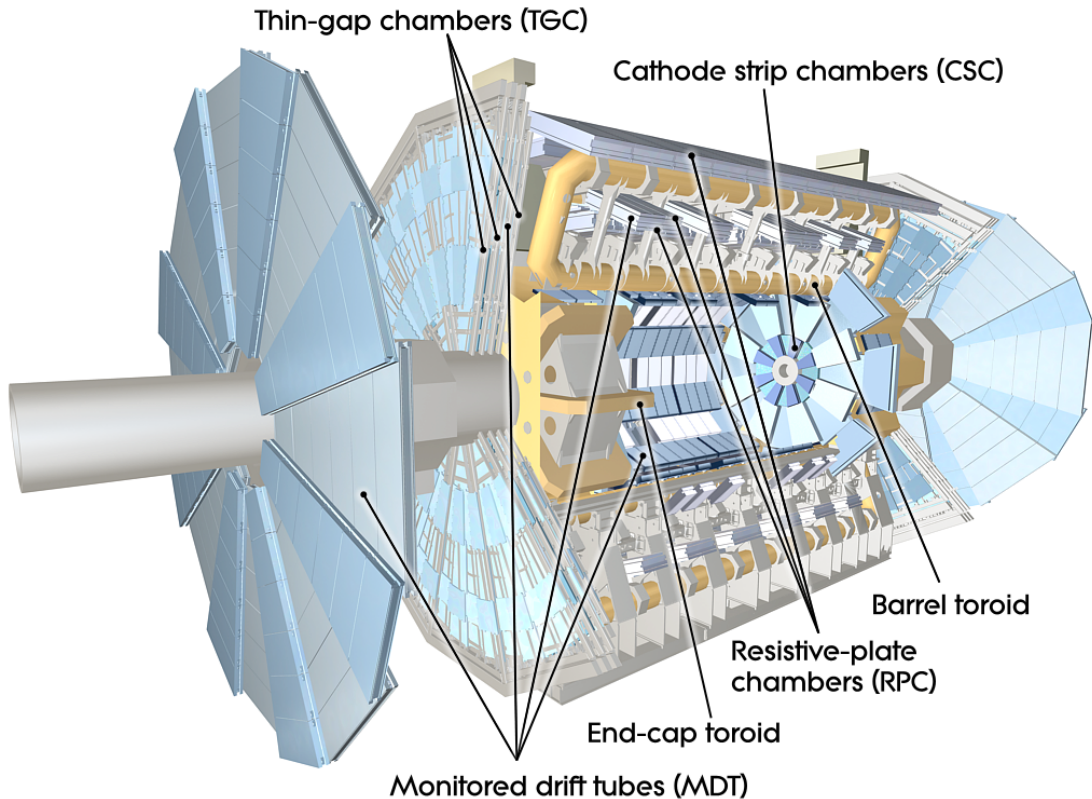


Figure 5.9: Schematic of Muon Spectrometer [cite G35]

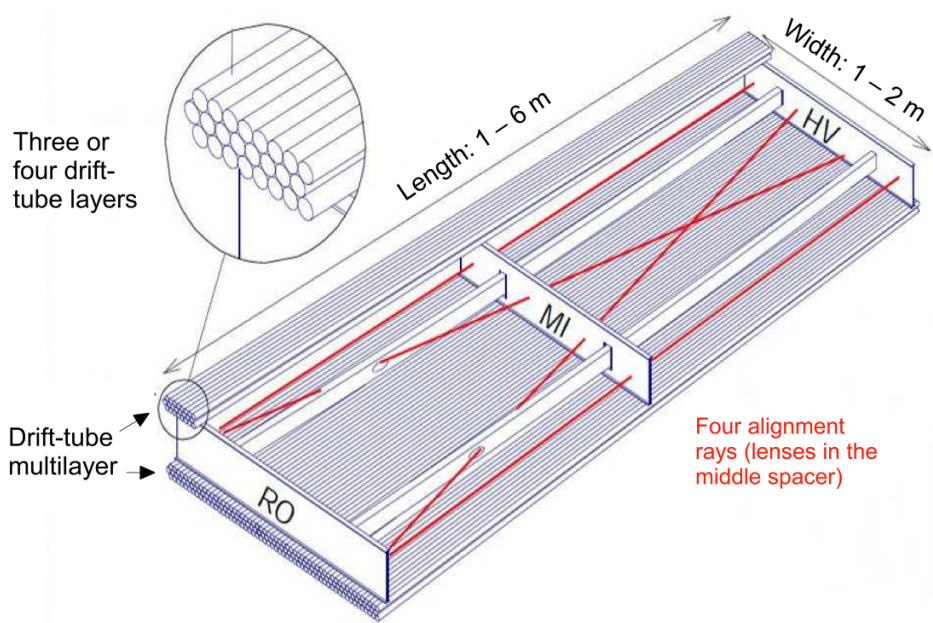


Figure 5.10: Schematic of MDT chamber. [cite G35]

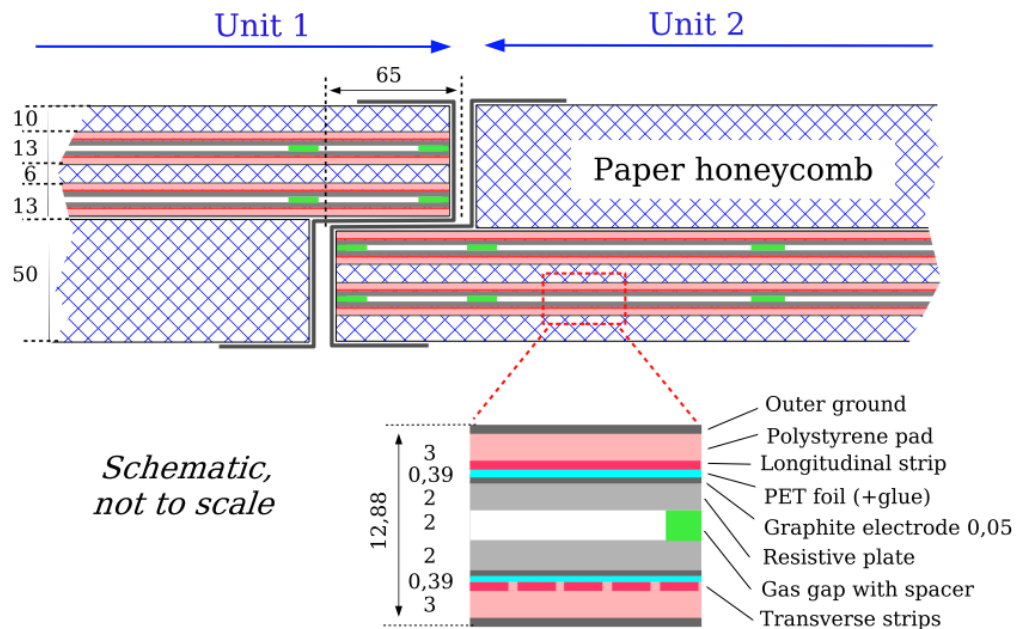


Figure 5.11: Schematic of RPC chamber, which is used for triggering in the central region of the detector [cite G35].

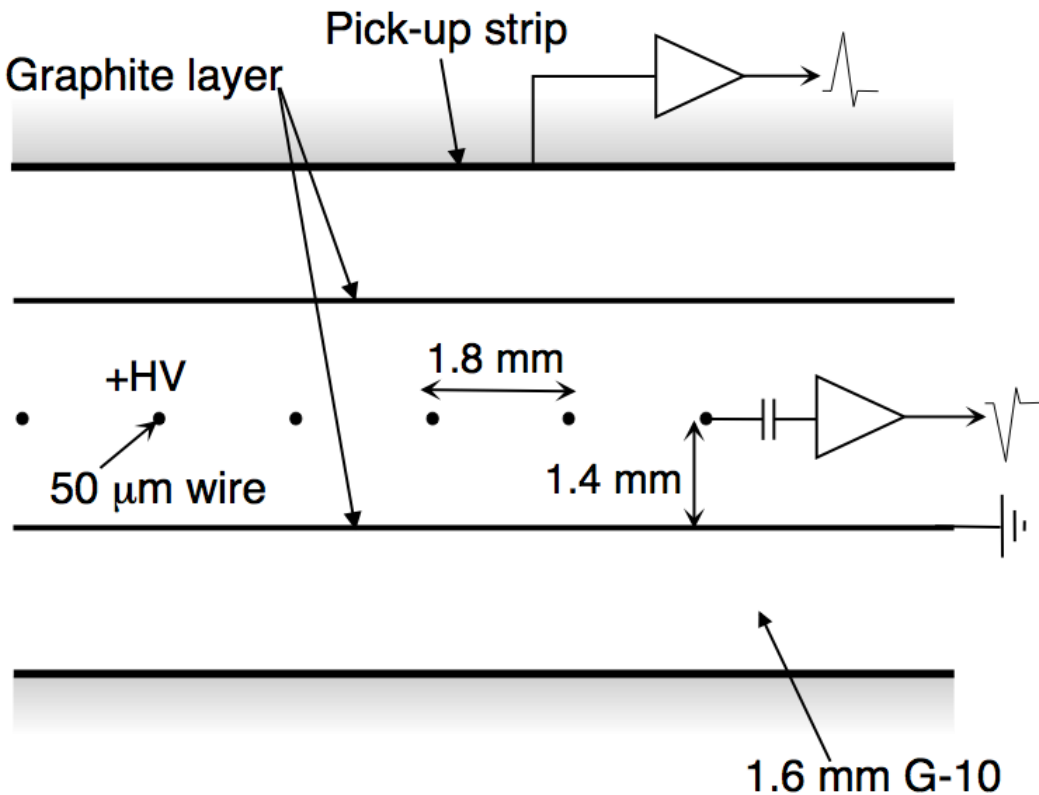


Figure 5.12: Schematic of TGC chamber, which is used for triggering in the muon end-cap region. [cite G35]

611 5.5 Magnet System

612 A particles with charge, q , and velocity v , moving in magnetic field, B , ex-
 613 periences a force, $F = qv \times B$. This force can cause charged particles to have a
 614 curved trajectory in magnetic fields, which the ID and MS use to determine the
 615 particles p_T . The central solenoid provides the magnetic field for the ID and the
 616 toroidal magnets provide the magnetic field for the MS.

617 The layout of the magnet system is shown in Figure 5.13. The central solenoid
 618 consists of a single-layer Al-stabilized NbTi conductor coil wound inside an Al

619 support cylinder. The solenoid is 5.8 m long, 50 cm thick and has an inner radius
620 of 1.23 m. It is cooled to 4.5 K to reach superconducting temperatures and shares
621 the liquid argon calorimeter vacuum vessel to minimize material in the detector.
622 A current of 7.730kA produces a 1.998 T solenoidal magnetic field, pointing in
623 the $+z$ direction.

624 The toroidal magnet system consists of a barrel and two end-cap toroidal
625 magnets used to create a magnetic field outside the calorimeters that is orientated
626 along ϕ . Each barrel toroid is 25.3 m long with an inner and outer diameter of 9.4
627 and 20.1 m and weighs 830 tonnes. Endcap toroids are 5 m long with an inner and
628 outer radius of 1.65 and 10.7 m. Both toroid systems use Al-stabilized Nb/Ti/Cu
629 conductors. The magnetic field strength in the barrel and endcap regions are 0.5
630 and 1 T, respectively.

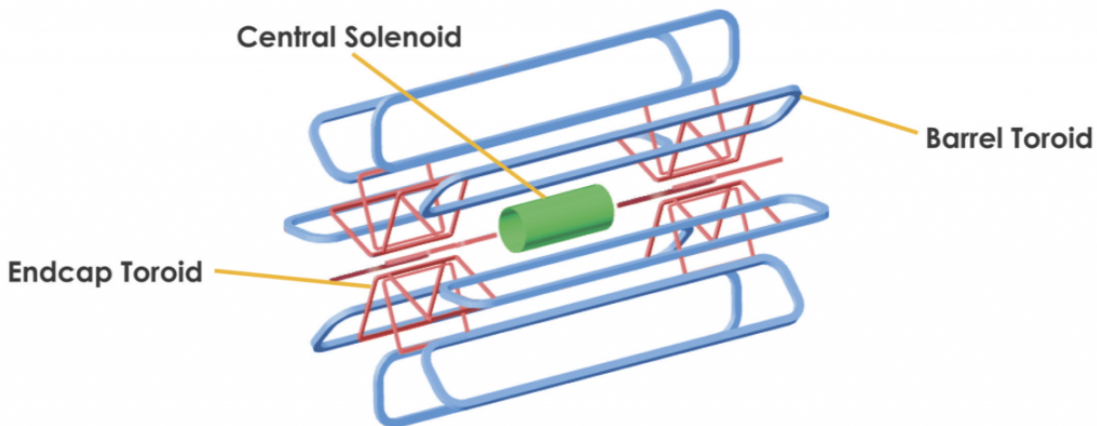


Figure 5.13: Layout of ATLAS magnet systems.

631 **5.6 Trigger System**

632 Since collisions occur every 25 ns and reading out all detector channels and
633 storing that information is not currently feasible (would require saving 60 million
634 megabytes per second), the majority of events are not kept for analysis. ATLAS

uses a multi-stage trigger system to select approximately 1,000 of the 1.7 billion collisions that occur each second (corresponding to a rate of 1 kHz from the 40 MHz proton collision rate). The first stage of the trigger system is the hardware level (L1) trigger. This trigger reduces the event rate to \sim 100 kHz by identifying Regions-of-Interest (ROIs) containing high p_T leptons, photons, jets, or E_T^{miss} by using information from RPCs, TGCs, and calorimeters to make a $2.5 \mu\text{s}$ decision. This information is then passed to a high-level trigger (HLT) which further decreases event rates to \sim 1 kHz. The HLT uses finer granularity measurements from the MS and ID to perform simplified offline reconstruction to decide which events to keep.

Part III

645

Method

646

647 **Chapter 6**

648 **Dataset and Simulated Samples**

649 **6.1 Dataset**

650 This analysis uses pp collision data collected from 2015 to 2018 at $\sqrt{s} = 13$
651 TeV, corresponding to 139/fb of data as shown in Figure 6.1 and 6.2. From this
652 dataset, only those events in which the tracker, calorimeters, and muon spectrom-
653 eter have good data quality are used. For a given event, the solenoid and toroidal
654 magnets must also be operating at their nominal field strengths. In addition to
655 this, events must pass further quality checks to reject events where detector sub-
656 systems may have failed. These selections reject events that containing LAr noise
657 bursts, saturation in the electromagnetic calorimeter, TileCal errors, and failures
658 in event recovery due to tracker failures. Events with information missing from
659 subsystems (usually due to busy detector conditions) are rejected. Events must
660 also contain a primary vertex with at least two associated tracks, where the pri-
661 mary vertex is selected as the vertex with the largest $\sum p_T^2$ over tracks associated
662 with the vertex and $p_T > 0.5$ GeV.

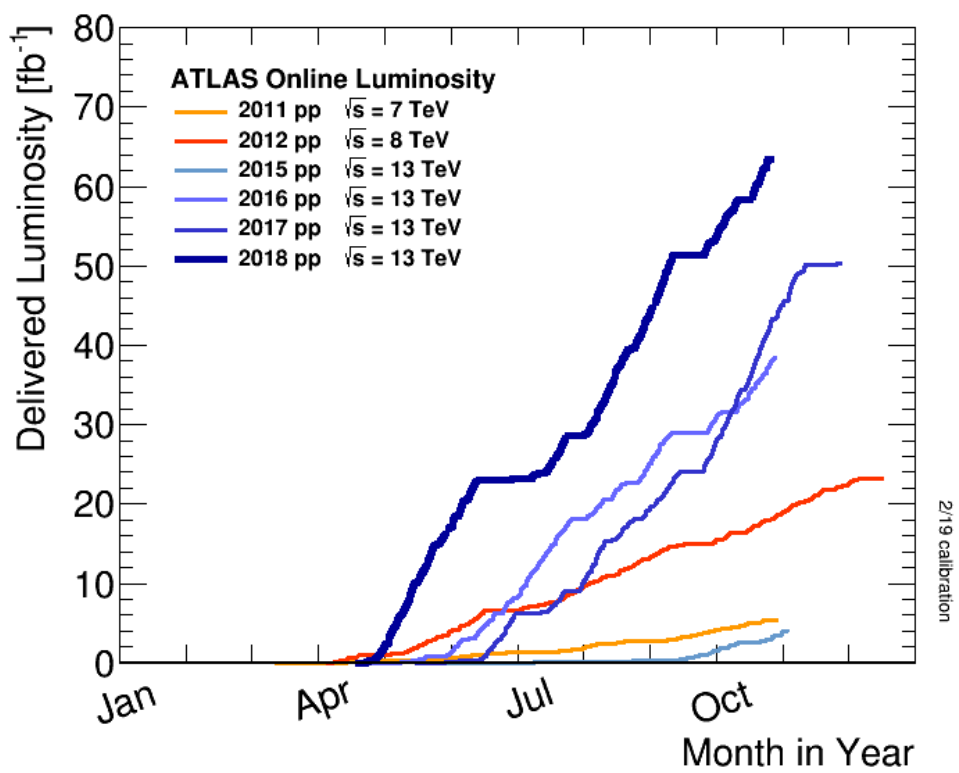


Figure 6.1: Integrated luminosity for data collected from ATLAS from 2011 - 2018

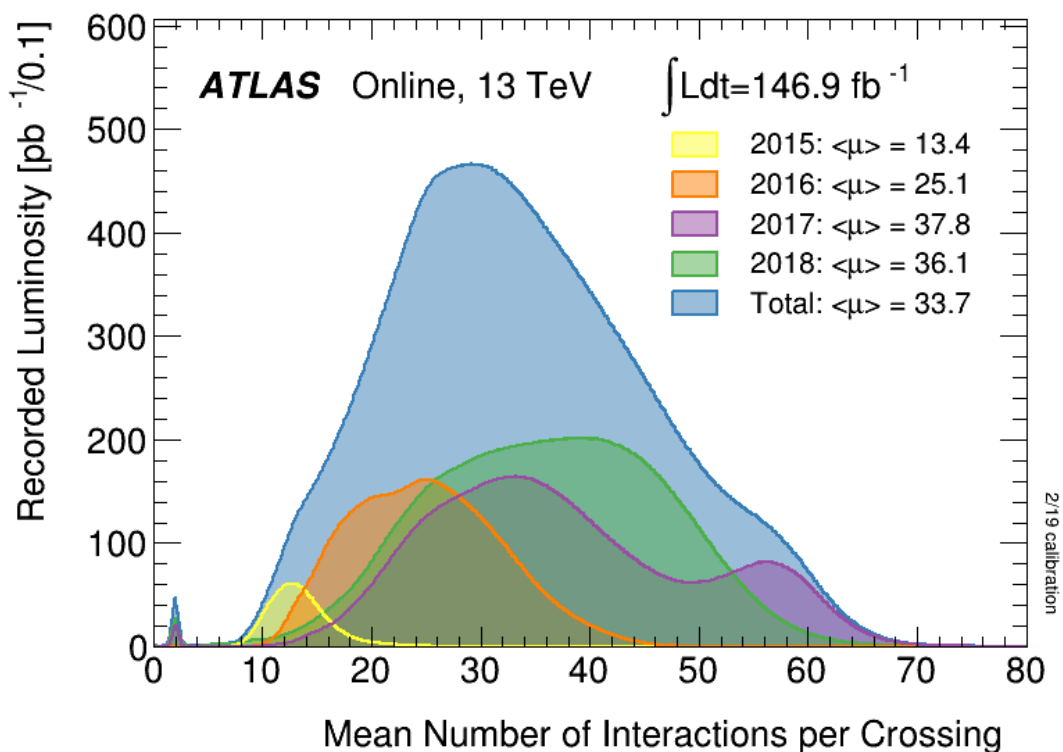


Figure 6.2: Mean number of interactions per crossing for data collected from ATLAS from 2011 - 2018

663 6.2 Simulated Samples

664 Samples are simulated in order to model backgrounds, evaluate signal ac-
665 ceptance, optimize event selection and estimate systematic and statistical uncer-
666 tainties. The dominant backgrounds for this analysis are $W/Z + \text{jets}$, diboson
667 (WZ/WW), $t\bar{t}$, single top and multijet production.

668 $W/Z+\text{jet}$ events are simulated using Sherpa 2.2.1 at NLO [cite [29]] and merged
669 with the Sherpa parton shower using the ME+PS@NLO prescription [12]. These
670 events are then normalized to NNLO cross sections. The $t\bar{t}$ and single-top back-
671 grounds are generated with Powheg-Box with NNPDF3.0NLO PDF sets in the
672 matrix element calculation [cite[35]]. For all processes, the parton shower, frag-
673 mentation, and underlying event are simulated using Pythia 8.320 with the A14
674 tune set[cite[ATL-PHYS-PUB-2014-02]]. Diboson processes are generated using
675 Sherpa 2.2.1.

676 Signal samples are simulated using MadGraph 5-2.2.2 [cite 42] and Pythia
677 8.186 with NNPDF230LO. RS Graviton samples are generated with $k/M_{PL}=1$.
678 HVT Model A (B) samples are simulated with $g_V = 1(3)$, as the difference in the
679 width of the samples is smaller than detector resolution. Model C is generated by
680 setting $g_H = 1$ and $g_f = 0$ to model VBF production of HVT bosons. Signals are
681 generated for masses between 300 GeV and 5 TeV.

682 **Chapter 7**

683 **Objects**

684 **7.1 Electrons**

685 Electrons are reconstructed from electromagnetic showers in the LAr EM
686 calorimeter. During reconstruction cells of $\Delta\eta \times \Delta\phi = 0.025 \times 0.025$ are grouped
687 into 3×5 clusters. These clusters are then scanned for local maxima that seed
688 electron clusters. These clusters must then be matched to ID track from the PV.
689 This requirement minimizes non-prompt electron and fake electron backgrounds.
690 Electrons must pass identification and isolation requirements. Electron identifica-
691 tion (loose, medium, tight) classification is based on a multivariate discriminant
692 that identifies electrons using a likelihood based method. For this analysis tight
693 electrons are used. Electrons are also required to be isolated. The electrons are
694 considered isolated if the quotient of the sum of the transverse momentum (of
695 calorimeter energy deposits) in a cone around the electron of size $\Delta R = 0.2$ and
696 the transverse momentum of the electron to be less than $0.015 * p_T$ or 3.5 GeV,
697 whichever is smaller. This requirement rejects non-prompt photons and other
698 fake leptons. Electrons in this analysis are also required to have $p_T > 30$ GeV and
699 $|\eta| < 2.47$. Electrons are also required to have $p_T > 30$ GeV.

700 Electrons are calibrated to determine data-driven scale factors using $J/\Psi \rightarrow$
701 ee , $Z \rightarrow ee$, $Z \rightarrow \ell\ell\gamma$ processes. These corrections account for the non-uniform
702 response of the detector which introduces modeling and reconstruction uncertain-
703 ties.

704 **7.2 Muons**

705 As muons traverse the entire detector, they are reconstructed from ID and MS
706 tracks. For this analysis the muon identification and isolation working points are
707 chosen to minimize the contributions from non-prompt muons. Towards this end,
708 the medium muon identification working point is used. For this working point,
709 two types of reconstructed muons are used: combined and extrapolated muons
710 (CB and ME, respectively). For CB muons, ID and MS tracks are reconstructed
711 independently and a combined track fit is performed by adding or removing MS
712 tracks to improve the fit quality. ME muons are reconstructed from only MS
713 tracks with hits in at least two layers, which ensures the track originates from the
714 PV. ME muons extend the acceptance for muon reconstruction outside the ID
715 from $2.5 < |\eta| < 2.7$. The medium identification working point uses CB and ME
716 tracks. CB tracks must have at least 3 hits in two MDT layers. ME tracks are
717 required to have at least three MDT/CSC hits. To further minimize contributions
718 from fake muons, the selected muons are required to be isolated from other tracks,
719 as muons from W, Z decays are often isolated from other particles. To insure the
720 selected muons are isolated, the scalar sum of the transverse momentum of tracks
721 in a cone of $\Delta R = 0.3$ compared to the transverse momentum of the muon must
722 be less than 0.06. Muons are also required to have $p_T > 30$ GeV.

723 Muons are calibrated using well-studied resonances $J/\Psi \rightarrow \mu\mu$ (low- p_T), $Z \rightarrow$
724 $\mu\mu$ (high- p_T). Figure 7.1 shows the combined muon p_T uncertainty from this

725 calibration. The total systematic uncertainty is less than 1% for all p_T ranges
 726 considered in this analysis.

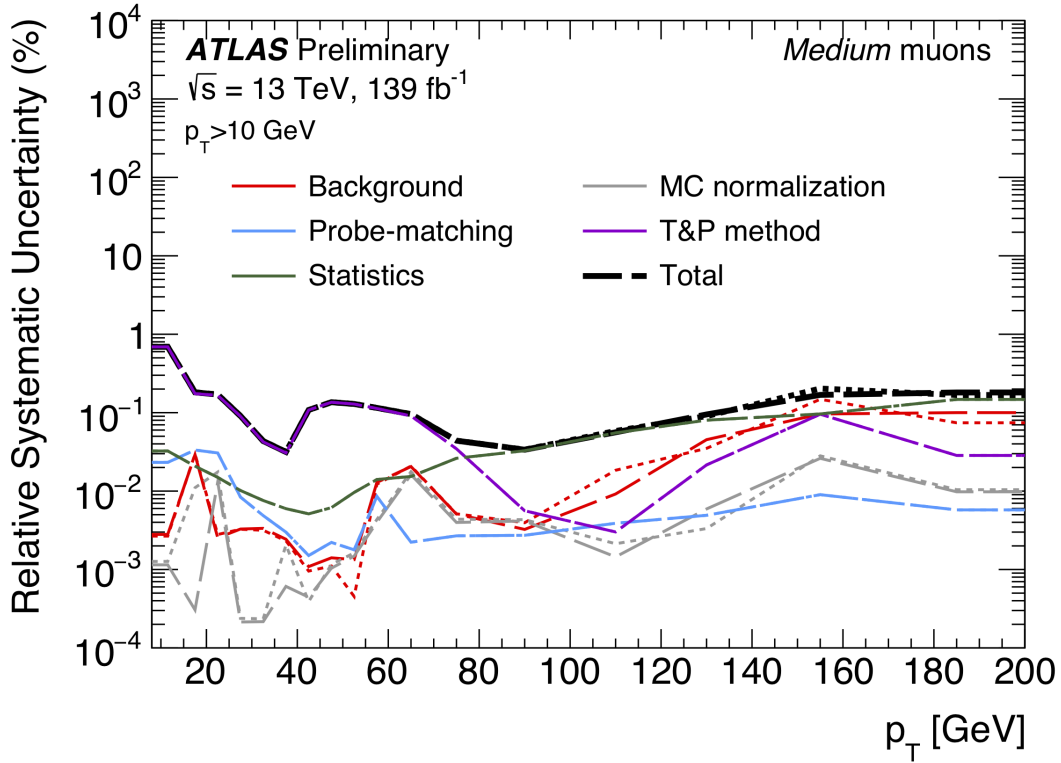


Figure 7.1: This figure shows the breakdown of the muon reconstruction efficiency scale factor measured in $Z \rightarrow \mu\mu$ as a function of p_T [4].

727 7.3 Jets

728 Three types of jets are used in this analysis: variable radius, small-R and
 729 large-R jets. Variable radius jets are used to reconstruct Z bosons decaying to
 730 two b -jets in the jet catchment area of large-R jet in the Merged regime. Small-R
 731 jets are used to reconstruct the hadronically decaying W/Z candidates in the
 732 resolved analysis and the forward jets from resonances produced through vector
 733 boson fusion. Large-R jets are used to reconstruct the hadronically decaying boson

734 in the merged regime.

735 For all of these jet collections, the jet energy is calibrated sequentially as shown
736 in Figure 7.2. After the jet direction is corrected to point to the PV, the energy
737 of the jet is corrected. First, the jet energy is corrected to account for pileup
738 contributions based on the p_T and area of the jet (these corrections are extracted
739 from a $pp \rightarrow jj$ sample). Following this, another pileup correction is applied that
740 scales with μ and N_{PV} .

741 MC-based corrections are then applied that are meant to transform the jet
742 energy and η back to truth level. Therefore, these corrections account for the
743 non-compensating nature of the ATLAS calorimeters and inhomogeneity of the
744 detector. Following this, the Global Sequential Calibration is applied that re-
745 duces flavor dependence of jet calibrations and accounts for energy leakage of jets
746 outside the calorimeters. Finally, in-situ corrections are applied that account for
747 differences in jet responses between data and simulation ($\gamma/Z+jet$ and fake lep-
748 ton samples are used). These differences can be due to mismodelling of the hard
749 scatter event, pile-up, jet formation, etc.

750 To further reject fake jets, jets must pass quality requirements based on the
751 following variables ([cite P42]):

752 - f_Q^{LAr} : fraction of energy of jet's LAr cells with poor signal shape

753 - f_Q^{HEC} : fraction of energy of jet's HEC cells with poor signal shape

754 - E_{neg} : sum of cells with negative energy

755 - f_{EM} : fraction of jet's energy deposited in EM calorimeter

756 - f_{HEC} : fraction of jet's energy deposited in HEC calorimeter

757 - f_{max} : maximum energy fraction in any single calorimeter layer

758 - f_{ch} : ratio of the scalar sum of the p_T of a jet's charged tracks to the jet's p_T

759 Jets selected for the resolved analysis must pass one of the following criteria:

760 - $f_{HEC} > 0.5$ and $|f_Q^{HEC}| > 0.5$ and $\langle Q \rangle > 0.8$

761 - $|E_{neg}| > 60$ GeV

762 - $f_{EM} > 0.95$ and $f_Q^{LAr} > 0.8$ and $\langle Q \rangle > 0.8$ and $|\eta| < 2.8$

763 - $f_{max} > 0.99$ and $|\eta| < 2$

764 - $f_{EM} < 0.05$ and $f_{ch} < 0.05$ and $|\eta| < 2$

765 - $f_{EM} < 0.05$ and $|\eta| > 2$

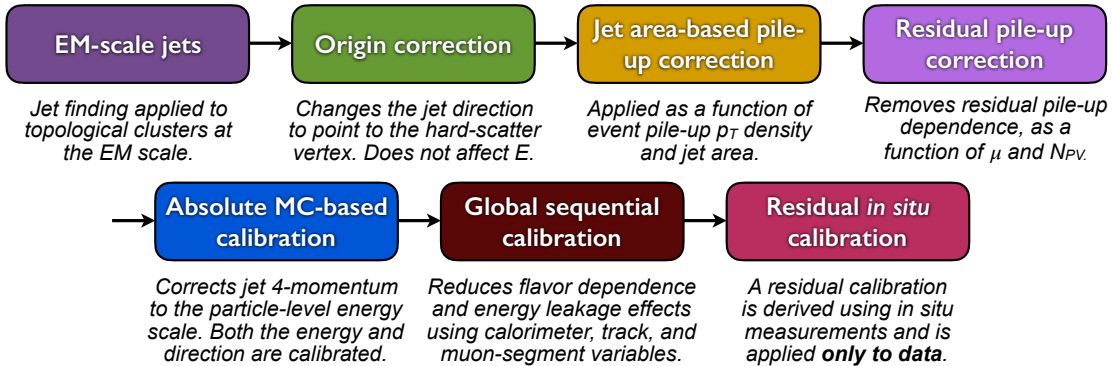


Figure 7.2: [7] This diagram shows the calibration stages for EM jets.

766 7.3.1 Small-R jets

767 Small-R jets are used to reconstruct the hadronically decaying W/Z candidate when the two resulting jets are well-separated in $\eta\phi$ space. Small-R jets
768 are also used to identify forward jets from resonances produced through vector
769 boson fusion. Small-R jets are constructed from topologically connected clusters
770

771 of calorimeter cells (topoclusters), seeded from calorimeter cells with energy de-
772 posits significantly above the noise threshold. These cells are then used as inputs
773 to the $anti-k_t$ algorithm [14] with a radius parameter, $R = 0.4$.

774 Jets used in this analysis must have $p_T > 30$ GeV and $|\eta| < 2.5$. To further
775 reduce fake jets the jet-vertex-tagger (JVT) is used to reject pile-up jets [6]. The
776 JVT uses two track-based variables, corrJVF and R_{p_T} to calculate the likelihood
777 that the jet originated from the PV. The corrJVF compares the scalar sum of the
778 p_T of tracks associated with the jet and PV to the scalar sum of the p_T of tracks
779 associated with the jet. This variable also includes a correction that reduces the
780 dependency of corrJVF with the number of reconstructed vertices in the event.
781 The other discriminant, R_{p_T} , is given by the ratio of the scalar sum of the p_T of
782 tracks associated with the jet and PV to the p_T of the jet. Both of these variables
783 peak around zero for pileup jets, as these jets are unlikely to have tracks associated
784 with the PV. JVT cuts are applied to all jets with $p_T > 120$ GeV. Central jets
785 ($|\eta| < 2.4$) are required to have a $JVT > 0.59$ and forward jets ($2.4 < |\eta| < 2.5$)
786 are required to have $JVT > 0.11$.

787 7.3.2 Large-R jets

788 Large-R ($R = 1.0$) jets are used to reconstruct the hadronically decaying W/Z
789 candidate when the resulting jets are not well-separated in $\eta\phi$ space, and overlap
790 forming one large-R jet. Track-Calorimeter Clusters (TCCs) are used to reconstruct these
791 jets [cite ANA 50]. These jets are constructed using a pseudo particle flow method
792 using ID tracks matched to calorimeter clusters. The angular resolution of the
793 calorimeter degrades sharply with jet p_T , but the jet energy resolution improves.
794 The tracker has excellent angular resolution which improves with p_T . Therefore,
795 by matching tracks to jets, TCCs have more precise energy and angular resolution

796 than jets constructed from calorimeter information only. These jets are required
 797 to have $p_T > 200$ GeV, $|\eta| < 2.0$ and $m_J > 50$ GeV.

798 TCC jets are trimmed as detailed in [cite ANA 45], which suppresses pileup
 799 and soft radiation in the jet, the jet mass is calculated as the four-vector sum
 800 of the jet's constituents (assuming massless constituents). The jet mass peaks
 801 around the W/Z boson mass for $W/Z \rightarrow qq$ jets, and more broadly for quark and
 802 gluon induced jets.

803 These jets are then tagged as W jet if it passes optimized jet mass and D_2
 804 cuts for W bosons, and a Z jet if it passes the optimized cuts for the Z boson.
 805 The jet substructure variable D_2 is given by the ratio of energy correlation func-
 806 tions. These fuctions are derived from the energies and pair-wise angles of a jet's
 807 constituents [cite ANA 46, 47]:

$$D_2^{\beta=1} = E_{CF3} \left(\frac{E_{CF1}}{E_{CF2}} \right)^3 \quad (7.1)$$

808 Where the energy correlation functions are defined as:

$$E_{CF1} = \sum_i p_{T,i} \quad (7.2)$$

$$E_{CF2} = \sum_{ij} p_{T,i} p_{T,j} \Delta R_{ij} \quad (7.3)$$

$$E_{CF3} = \sum_{ijk} p_{T,i} p_{T,j} p_{T,k} \Delta R_{ij} \Delta R_{jk} \Delta R_{ki} \quad (7.4)$$

811 A two-dimensional optimization of the jet mass and D_2 thresholds was per-
 812 formed to provide maximum sensitivity for this analysis. This optimization was
 813 done by maximizing the signal sensitivity (using HVT W' and G_{KK} samples)
 814 against the single quark and gluon jet backgrounds in bins of jet p_T . Figure 7.3
 815 shows the optimized thresholds on D_2 and jet mass as a function of p_T . Figure

⁸¹⁶ 7.4 shows the efficiency of the optimized W/Z taggers as a function of jet p_T .

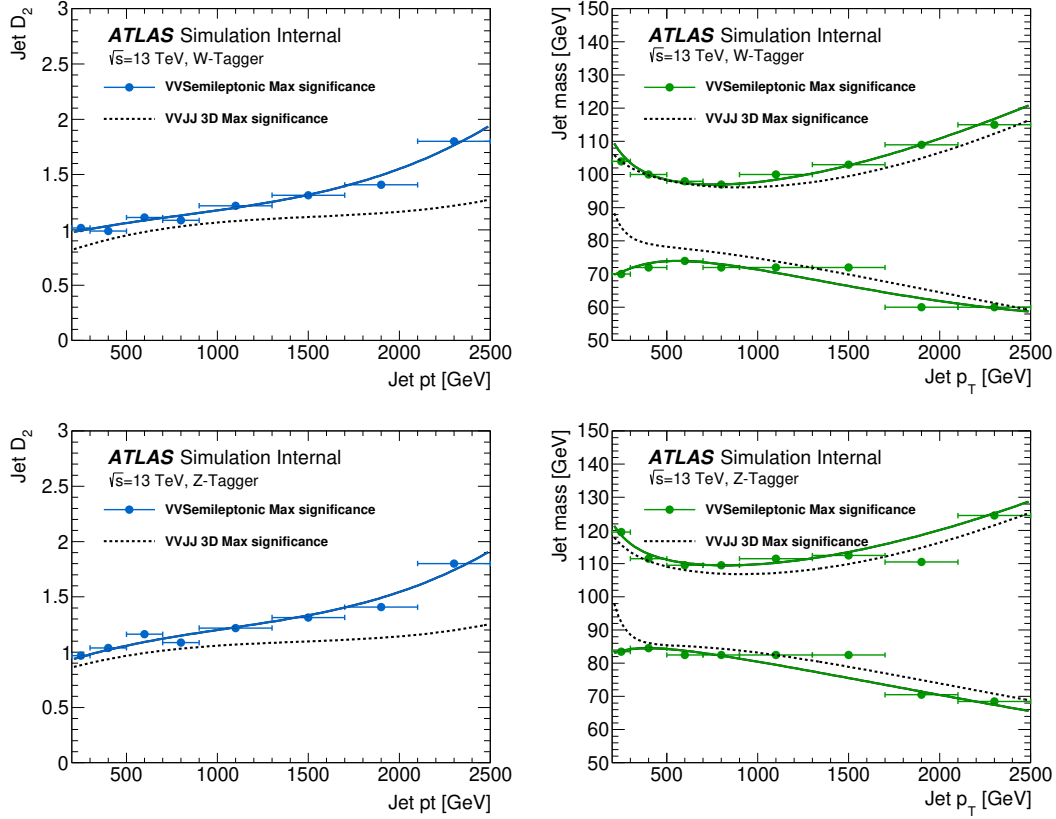


Figure 7.3: The upper cut on D_2 (a) and jet mass window cut i.e. the upper and lower boundary of the mass (b) of the W -tagger as a function of jet p_T . Corresponding values for Z -tagger are shown in (c) and (d). The optimal cut values for maximum significance are shown as solid markers and the fitted function as solid lines. Working points from $VV \rightarrow JJ$ [ATLAS-HDBS-2018-31-002] is also shown as dashed lines as a reference. Natasha reword?

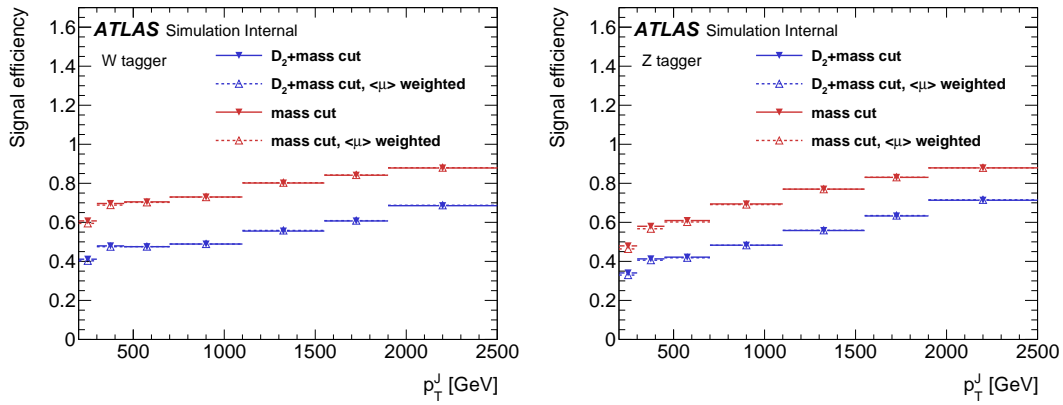


Figure 7.4: Natasha write caption

817 7.3.3 Variable Radius jets

818 To more accept more boosted Z bosons decaying to $b\bar{b}$ that would normally be
 819 rejected due to topological cuts discussed 8.4 variable radius (VR) track jets are
 820 used to identify b -jets within the catchment area of large-R jets [13]. VR jets are
 821 constructed from ID tracks using the anti- k_t algorithm with a radius parameter
 822 that depends on the p_T of the track, shown in Equation 7.5.

$$R_{eff}(p_{T,i}) = \frac{\rho}{p_{T,i}} \quad (7.5)$$

823 For this search $\rho = 30$ GeV and an upper and lower limit on cone size are set
 824 to 0.02 and 0.4, respectively, to prevent unphysical asymptotic behavior of ρ .
 825 Collinear VR jets are possible, so track jets that are not separated by the the
 826 smaller jet's cone size are not used. Additionally, VR jets are required to have
 827 $p_T > 10$ GeV and $|\eta| < 2.5$.

828 **7.3.4 Jet Flavor Tagging**

829 To further classify events, the small-R and VR jets originating from a b-quark
830 are classified using a multivariate b -tagging algorithm (BDT), MV2c10 [cite G 210
831 199]. This algorithm uses the impact parameters of the jet's ID tracks, secondary
832 vertices (if they exist), and reconstructed flight paths of b and c hadrons in the
833 jet to determine if the jet was induced by a b -quark. For this analysis the 85%
834 efficient working point of this algorithm is used giving c , τ , and light-flavor jet
835 rejection of 3, 8, and 34 respectively in simulated $t\bar{t}$ samples.

836 **7.4 MET/Neutrinos**

837 As neutrinos are uncharged and colorless they do not leave tracks or jets in the
838 detector. For this reason, neutrinos are reconstructed calculated the E_T^{miss} , the
839 negative vector sum of p_T all the physics objects and an extra "soft" term. The
840 "soft" term accounts for energy deposits not associated with any of the objects in
841 the event. For this analysis the soft term is given by the sum p_T of all ID tracks
842 not associated with objects in the event. The selected tracks must be matched to
843 the primary vertex, which decreases pile-up contamination [cite G 217 218]. The
844 tight working point is used [Natasha look up what this means].

845 **7.5 Overlap Removal**

846 Reconstructed jets and leptons in this analysis can arise from the same energy
847 deposits. For instance, a cluster of energy from an electron can also be a valid
848 calorimeter seed for a jet. To mitigate this confusion of multiple objects originating
849 from a single jet or lepton overlapping objects are removed via a procedure referred
850 to as overlap removal. In this procedure the separation of the two objects, $\Delta(R) =$

851 $\sqrt{(\Delta\eta)^2 + (\Delta\phi)^2}$ determines which object is removed from the event.

852 The overlap selections used in this analysis are:

853 - when an electron shares a track with another electron with the lower p_T
854 electron is rejected, as it is more likely to be a fake electron

855 - when a muon and electron share a track the muon is rejected if it is a
856 calo-muon, otherwise the electron is rejected

857 - when $\Delta R < 0.2$ for an electron and jet, the jet is rejected to maximize signal
858 acceptance

859 - when $\Delta R > 0.2$ for an electron and jet, the electron is rejected as likely
860 originated from decays within the jet

861 - when $\Delta R < \min(0.4, 0.04 + 10\text{GeV}/p_T^\mu)$ the muon is rejected, again maximiz-
862 ing signal acceptance, otherwise the jet is rejected

863 - when $\Delta R < 1.0$ for the a large-R jet and electron, the jet is rejected

864 **Chapter 8**

865 **Event Selection and**

866 **Categorization**

867 **8.1 Pre-selection**

868 Before applying topological cuts to suppress backgrounds and reduce data
869 size in this search, preselection cuts are applied which include trigger and event
870 requirements. Events must contain exactly one tight lepton (no additional loose
871 leptons), the $p_T^{\ell\nu} > 75$ GeV, and there must be at least two small-R jets or one
872 large-R jet.

873 **8.2 Trigger**

874 The data were collected using the lowest unprescaled single-lepton or E_T^{miss}
875 triggers, as summarized in Table ???. Since the muon term is not considered in the
876 trigger E_T^{miss} calculation, the E_T^{miss} trigger is fully efficient to events with high- p_T
877 muons. For this reason, the E_T^{miss} trigger is used for events where $p_T^\mu > 150$ GeV, to
878 compensate for the poor efficiency of the single muon trigger above $p_T^\mu > 150$ GeV.

Table 8.1: The list of triggers used in the analysis.

Data-taking period	$e\nu qq$ channel	$\mu\nu qq$ ($p_T(\mu\nu) < 150$ GeV) channel	$\mu\nu qq$ ($p_T(\mu\nu) > 150$ GeV) channel
2015	HLT_e24_lhmedium_L1EM20 OR HLT_e60_lhmedium OR HLT_e120_lhloose	HLT_mu20_iloose_L1MU15 OR HLT_mu50	HLT_xe70
2016a (run < 302919) $(L < 1.0 \times 10^{34} \text{ cm}^{-2} \text{ s}^{-1})$	HLT_e26_lhtight_nod0_ivarloose OR HLT_e60_lhmedium_nod0 OR HLT_e140_lhloose_nod0 HLT_e300_etcut	HLT_mu26_ivarmedium OR HLT_mu50	HLT_xe90_mht_L1XE50
2016b (run ≥ 302919) $(L < 1.7 \times 10^{34} \text{ cm}^{-2} \text{ s}^{-1})$	same as above	same as above	HLT_xe110_mht_L1XE50
2017	same as above	same as above	HLT_xe110_pufit_L1XE55
2018	same as above	same as above	HLT_xe110_pufit_xe70_L1XE50

879 **8.3 non-VBF/VBF RNN**

880 To classify events as originating from non-VBF/DY or VBF production a
881 recursive neural network (RNN [19]) is used. This approach is more powerful than
882 a cut-based classification as it improves signal efficiency and analysis sensitivity
883 by exploiting correlations between variables that the RNN learns. In particular, a
884 RNN architecture is ideal as it can handle variable numbers of jets in the events.

885 The RNN uses the four-momentum of candidate VBF jets to classify events
886 as VBF or GGF topologies. As sometimes jets will be incorrectly reconstructed
887 the number of jets in the event are expected to vary across the inputs samples.
888 VBF candidate jets are identified by removing jets from the event that are likely
889 from $W/Z \rightarrow qq$. For the resolved regime this means removing the two leading
890 small-R jets from the VBF candidate jet list. For the merged regime this means
891 removing small-R jets separated by less than 1.0 in dR from the large-R jet. VBF
892 candidate jets are also required to be within $|\eta| < 4.5$. From the list of remaining
893 VBF candidate jets, the two highest- p_T jets are chosen.

894 The architecture of the RNN is show in Figure 8.1. LSTMs are a type of
895 RNN that extract meaningful information and can retain it (unlike other neural
896 networks architectures). This is useful for VBF event classification for events with
897 two jets, where using the kinematic properties of both jets (and their correlations)
898 will lead to more efficient event classification.

899 In this RNN architecture, the VBF candidates are first passed to a masking
900 layer which checks the number of jets in the event. If there is only one jet, only one
901 LSTM layer is used. The output of masking is then passed to a Long Short-Term
902 Memory (LSTM) cell, with a tanh activation function. This output is passed to
903 a dropout layer, that has a probability of 0.3 to completely forget the output of
904 the LSTM. Dropout is a regularization method, that prevents over-fitting. The

905 output of the dropout layer is then passed to the second LSTM and then through
906 another dropout layer with a probability of 0.3.

907 The weights and other parameters of the network are learned by training the
908 network with VBF and GGF signals over 200 epochs with an Adam Optimizer
909 [natasha add reference]. The training is truncated if the network parameters are
910 unchanged after ten iterations. The training, testing and validation sets are 56,
911 30, and 14 percent of the input samples, respectively. Figure [add INT figure
912 32] shows the loss function of the network as a function of training epochs. The
913 validation test set has a smaller loss function as dropout was not applied. Figure
914 8.3 shows the ROC curve for the RNN using k-fold cross validation.

915 Finally this output is passed to a dense layer [natasha ask antonio about this]
916 and then to a sigmoid activation layer, leading to an overall RNN score. Figure 8.2
917 shows the RNN discriminant for backgrounds, GGF signals, and VBF signals. The
918 RNN score is ~ 0 for GGF and background processes and ~ 1 for VBF processes.
919 Figure 8.4 shows the limits for various signal processes based on the RNN cut
920 applied. Requiring the RNN score to be > 0.8 was chosen as it provided the best
921 significance (and signal efficiency) across for this final state and the $\nu\nu qq$ and $\ell\ell qq$
922 channels this channel will be combined with for future publications.

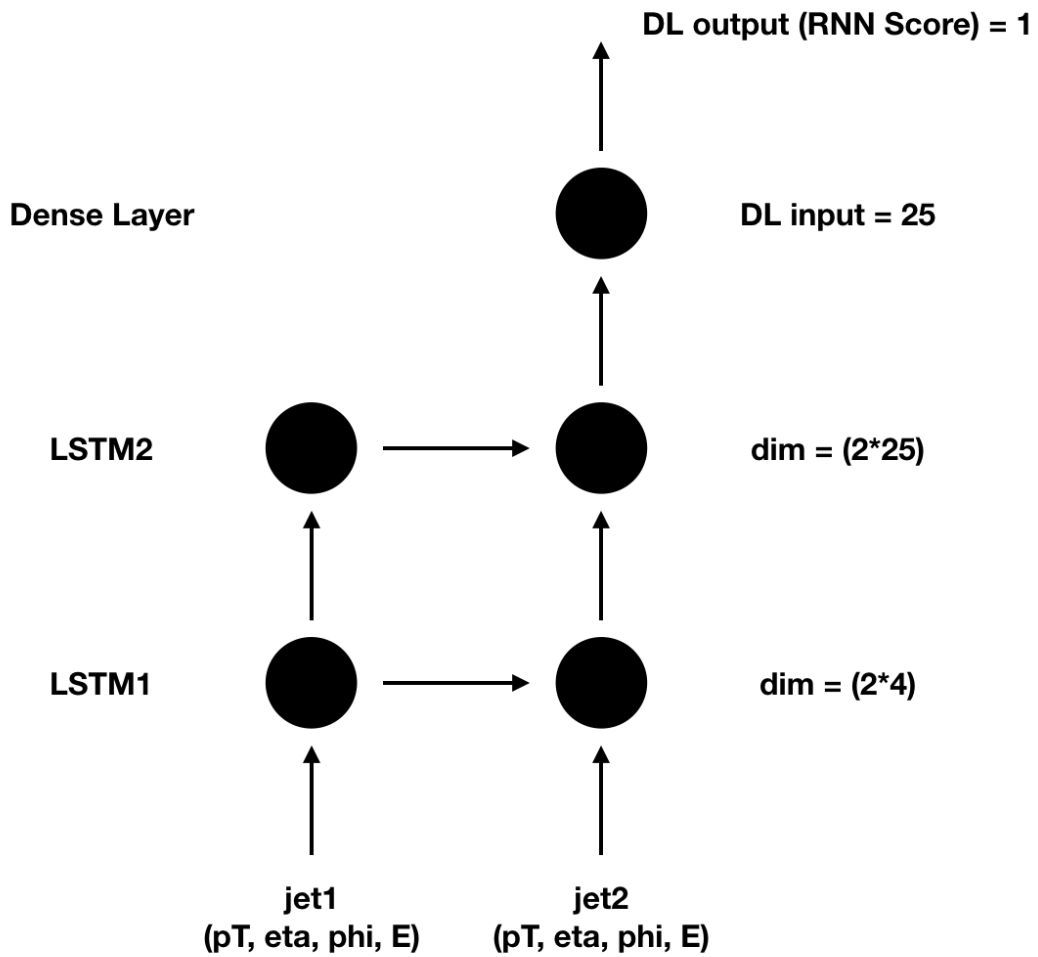


Figure 8.1: RNN architecture. Natasha add caption

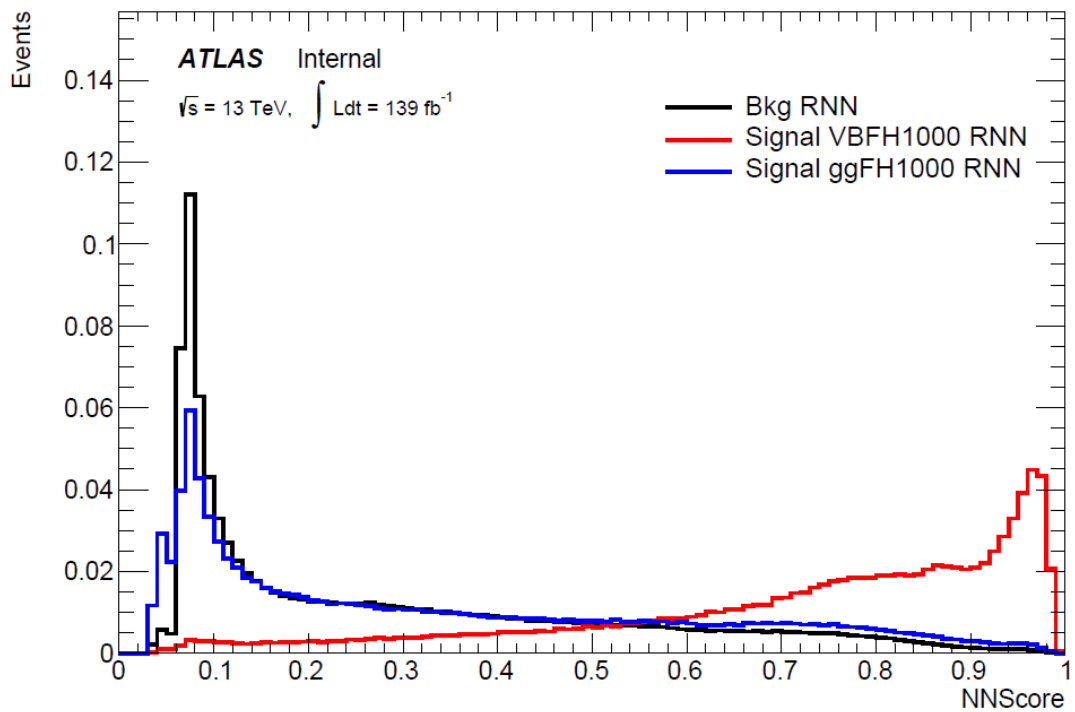


Figure 8.2: RNN Score distribution for ggF and VBF signals and backgrounds.

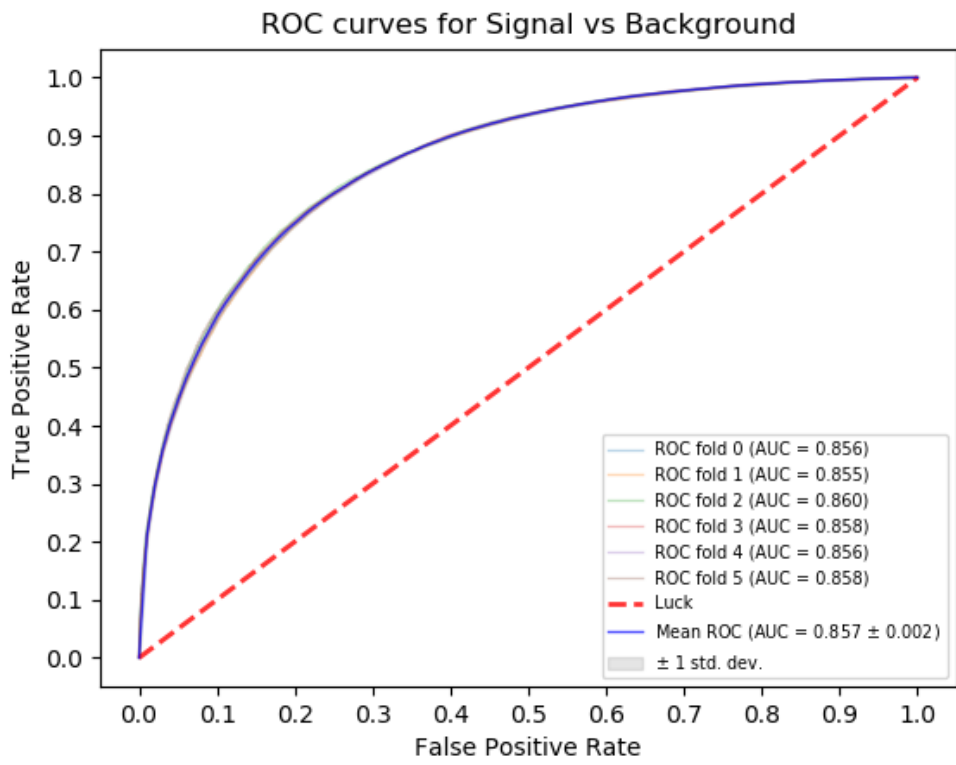


Figure 8.3: ROC curve using k-fold validation for RNN.

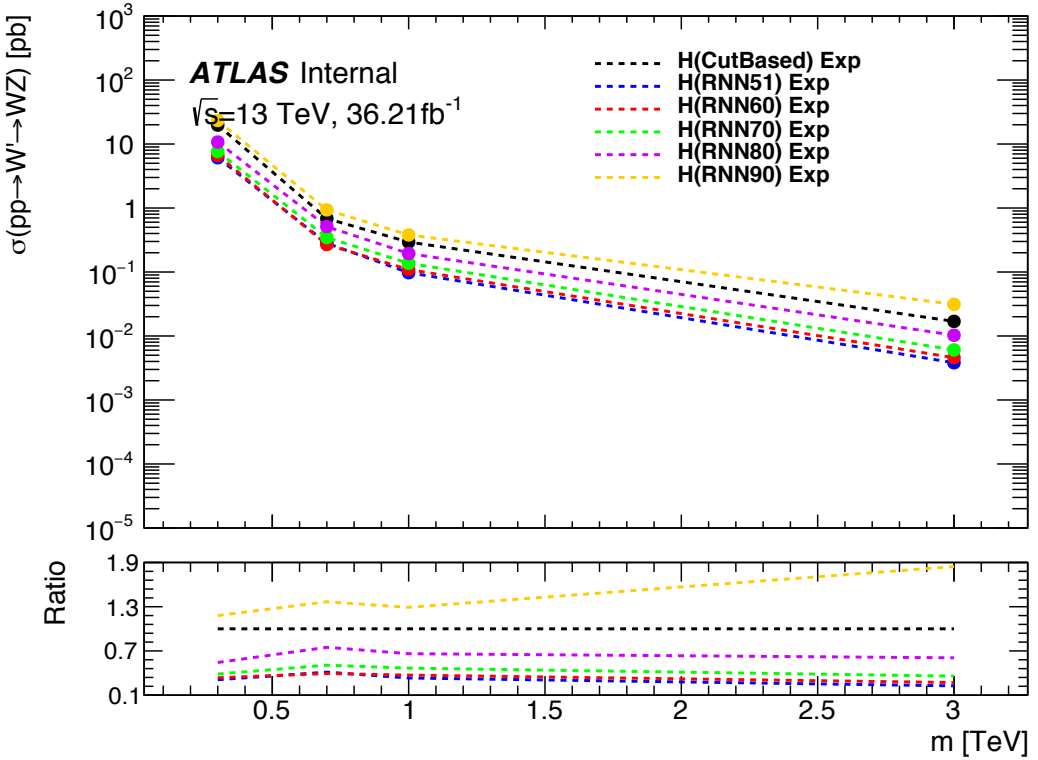


Figure 8.4: Comparison of GGF Z' limits for different RNN score selections. The bottom panel shows the ratio of the upper limits set for different RNN cuts to the cut-based analysis. In this panel smaller numbers, indicate that the expected upper limit is smaller than the cut-based analysis, which is desired.

923 8.4 Topological Cuts

924 Once an event is classified as VBF or GGF via the RNN, it must pass other
 925 topological cuts that maximize S/\sqrt{B} . First, to efficiently select events with a
 926 $W \rightarrow \ell\nu$ candidate exactly one tight lepton is required and $E_T^{miss} > 100(60)$
 927 GeV and $p_{T,\ell\nu} > 200(75)$ GeV in the merged (resolved) analysis to suppress the
 928 multi-jet background.

929 For the merged analysis, in addition to the $W \rightarrow \ell\nu$ and $W/Z \rightarrow J$ selections
 930 above, the $\min(p_{T,\ell\nu}, p_{T,J})/m_{WV} > 0.35(0.25)$ for the GGF (VBF) category. To
 931 reduce $t\bar{t}$ contamination events with the signal region and $W+jets$ control region

932 events with at least one b jet with $\Delta R > 1.0$ from the large-R jet are excluded.
 933 High purity signal regions require the D_2 and W/Z mass window cut to be passed,
 934 whereas the low purity region only requires the W/Z mass window cut to be
 935 passed. Finally for events to be classified as tagged the large-R jet must contain
 936 exactly two b-tagged jets. Untagged events must have no more than one b-tagged
 937 jet matched to the large-R jet. These selections are shown in Table 8.2. The
 938 distributions for the variables used in merged analysis for top control regions are
 939 shown in Figure 8.6-8.9.

940 Events failing the merged selection are then re-analyzed in the resolved cat-
 941 egory. To enhance resolved signals, the event should contain two high- p_T boson
 942 candidates that are back-to-back in the ϕ as shown by the cuts in Table 18. Again
 943 to suppress the $t\bar{t}$ background in the WCR and SR events are required to have no
 944 additional b-jets.

945 The WV system mass, m_{WV} is reconstructed from the lepton, neutrino, and
 946 hadronically-decaying boson candidate. The momentum of the neutrino along the
 947 z -direction is obtained by constraining the W boson mass of the lepton neutrino
 948 system to be $80.3 \text{ GeV}/c^2$. For complex solutions to this constraint, p_Z is taken
 949 as either the real component of the solution or the one with the smaller absolute
 950 value of the two real solutions. For the resolved analysis, m_{WV} is reconstructed
 951 by constraining the $W(Z)$ dijet system:

$$p_{T,jj}^{corr} = p_{T,jj} \times \frac{m_{W/Z}}{m_{jj}} \quad (8.1)$$

$$m_{jj}^{corr} = m_{W/Z} \quad (8.2)$$

952 where m_{jj} and $m_{W/Z}$ are the reconstructed invariant mass of the hadronically-
 953 decaying W/Z boson and the PDG values of the W/Z boson masses, respectively.

Table 8.2: Summary of selection criteria used to define the signal region (SR), W +jets control region (W CR) and $t\bar{t}$ control region ($t\bar{t}$ CR) for merged 1-lepton channel.

Selection	SR		W CR (WR)		$t\bar{t}$ CR (TR1)	
	HP	LP	HP	LP	HP	LP
$W \rightarrow \ell\nu$	Num of Tight leptons		1			
	Num of Loose leptons		0			
	E_T^{miss}		> 100 GeV			
	$p_T(\ell\nu)$		> 200 GeV			
$W/Z \rightarrow J$	Num of large- R jets		≥ 1			
	D_2 cut		pass	fail	pass	fail
	W/Z mass window cut		pass	pass	fail	pass
	Numb. of associated VR track jets b -tagged		For $Z \rightarrow J$: ≤ 1 ($= 2$) for untagged (tagged) category			
	Topology cut		$\min(p_{T,\ell\nu}, p_{T,J}) / m_{WV} > 0.35(0.25)$ for DY/ggF (VBF) category			
	Top-quark veto		Num of b -tagged jets outside of large- R jet		0	≥ 1
Pass VBF selection			no (yes) for DY/ggF (VBF) category			

955 A summary of the resolved selections is shown in Table 8.3. The distributions for
 956 the variables used in the resolved analysis in the TCR are shown in Figure 8.10,
 957 8.11.

958 The analysis cutflow is shows in Figure 8.5. Events classified as VBF events
 959 are classified as Merged High purity, low purity or resolved signal region selections
 960 sequentially. If the event does not pass any of these selections but passes a VBF
 961 control region selection it is classified as a VBF CR event. If the event fails the
 962 VBF selection it is then checked if it passes the Merged High purity, Low purity
 963 or resolved signal region selections (NB: for the WZ decay modes all the regions
 964 have tagged and untagged categories). If the event fails all the GGF signal region
 965 selections, it is then kept for GGF control region selections, if it passes those
 966 selections.

Table 8.3: The list of selection cuts in the resolved analysis for the WW and WZ signal regions (SR), $W+\text{jets}$ control region (WR) and $t\bar{t}$ control region (TR).

cuts	SR	W CR (WR)	$t\bar{t}$ CR (TR1)
$W \rightarrow \ell\nu$	Number of Tight leptons	1	
	Number of Loose leptons	0	
	E_T^{miss}	$> 60 \text{ GeV}$	
	$\cancel{p}_T(\ell\nu)$	$> 75 \text{ GeV}$	
$W/Z \rightarrow jj$	Number of small-R jets	≥ 2	
	Leading jet p_T	$> 60 \text{ GeV}$	
	Subleading jet p_T	$> 45 \text{ GeV}$	
	$Z \rightarrow q\bar{q}$ $W \rightarrow q\bar{q}$	$78 < m_{jj} < 105 \text{ GeV}$ $68 < m_{jj} < 98 \text{ GeV}$	$50 < m_{jj} < 68 \text{ GeV}$ or $105 < m_{jj} < 150 \text{ GeV}$
Topology cuts	Num. of b -tagged jets	For $Z \rightarrow jj$: ≤ 1 ($= 2$) for untagged (tagged) category	
	$\Delta\phi(j, \ell)$	> 1.0	
	$\Delta\phi(j, E_T^{\text{miss}})$	> 1.0	
	$\Delta\phi(j, j)$	< 1.5	
	$\Delta\phi(\ell, E_T^{\text{miss}})$	< 1.5	
Top vetos	$\min(p_{T,\ell\nu}, p_{T,jj}) / m_{WW}$	$> 0.35(0.25)$ for DY/ggF (VBF) category	
	Number of additional b -tagged jets	0	≥ 1
Pass VBF selection		no (yes) for DY/ggF (VBF) category	

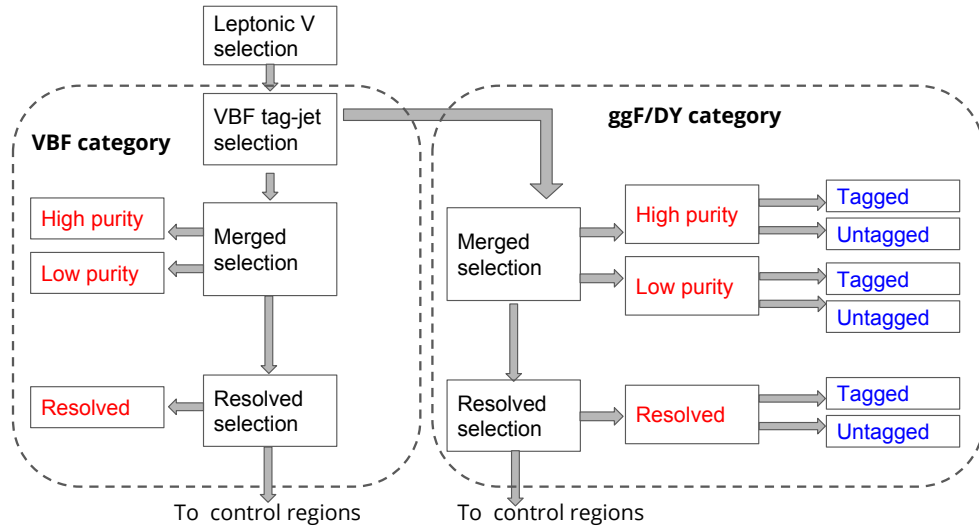


Figure 8.5: Event Categorization. Natasha write more.

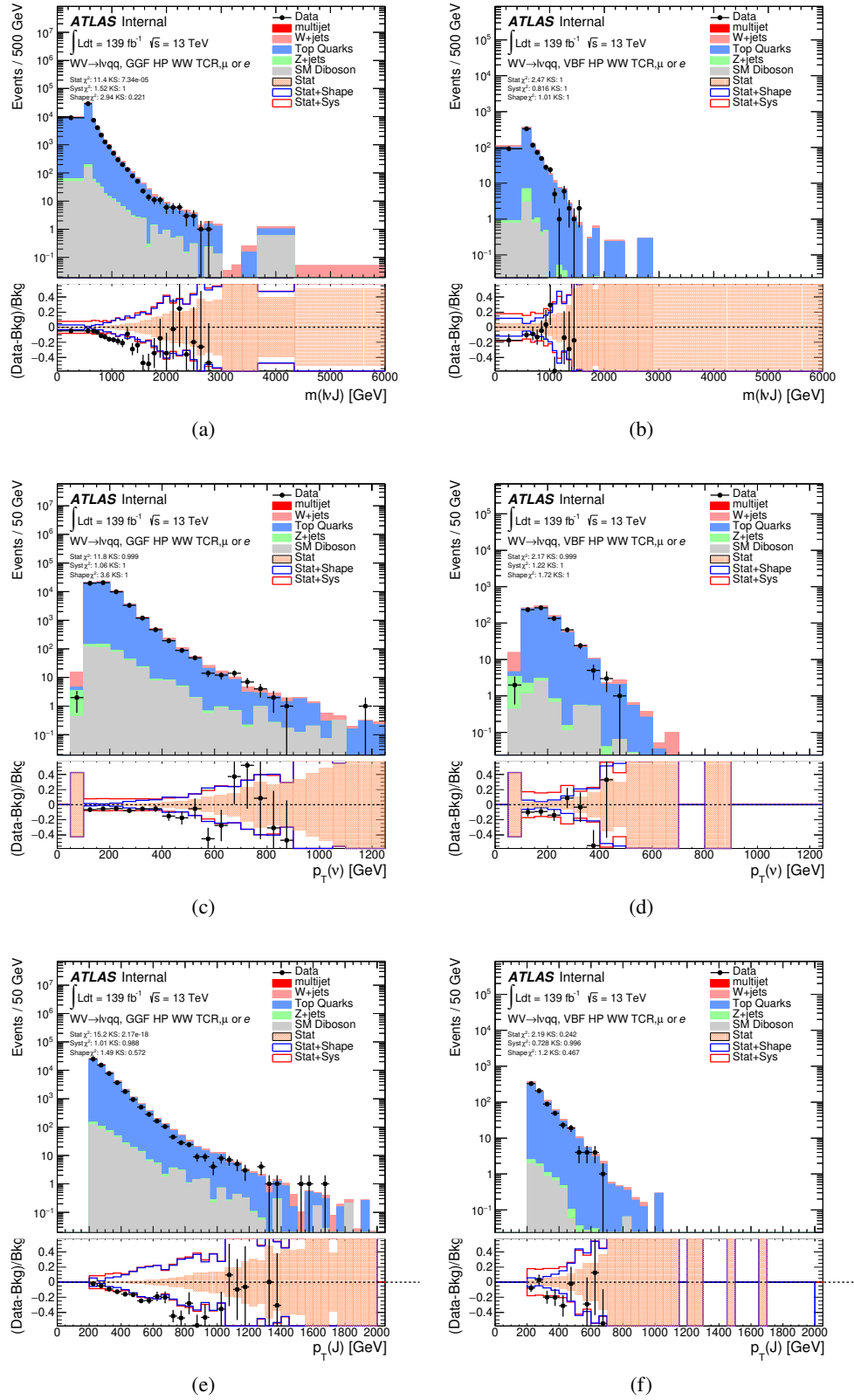


Figure 8.6: Data MC comparison for the merged WW HP TCR. The bottom panel shows the ratio of the difference⁸⁴ between data and simulation to simulation. The red bands include the all systematic and statistical uncertainties on the background.

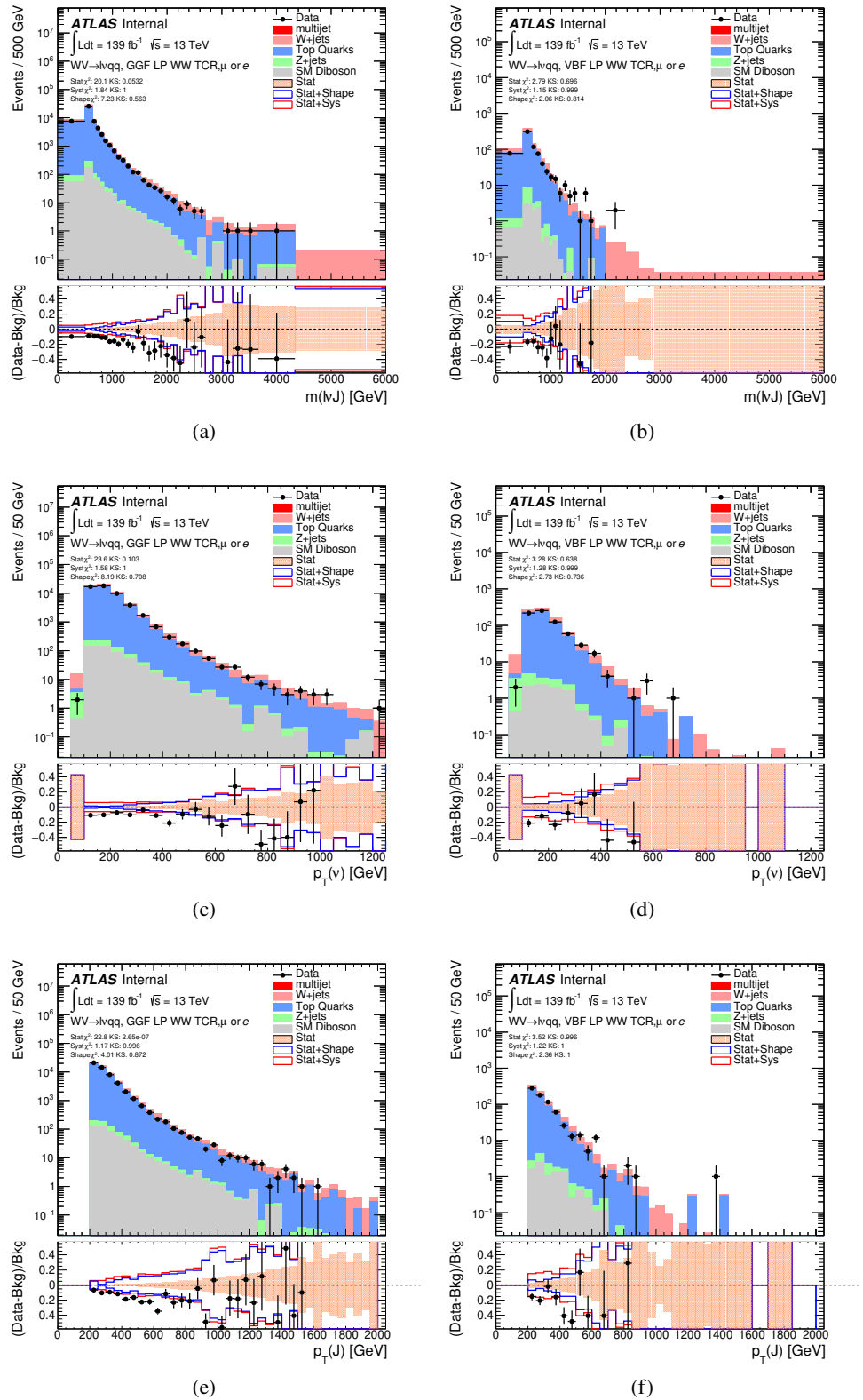


Figure 8.7: Data MC comparison for the merged WW LP TCR. The bottom panel shows the ratio of the difference between data and simulation to simulation. The red bands include the all systematic and statistical uncertainties on the background.⁸⁵

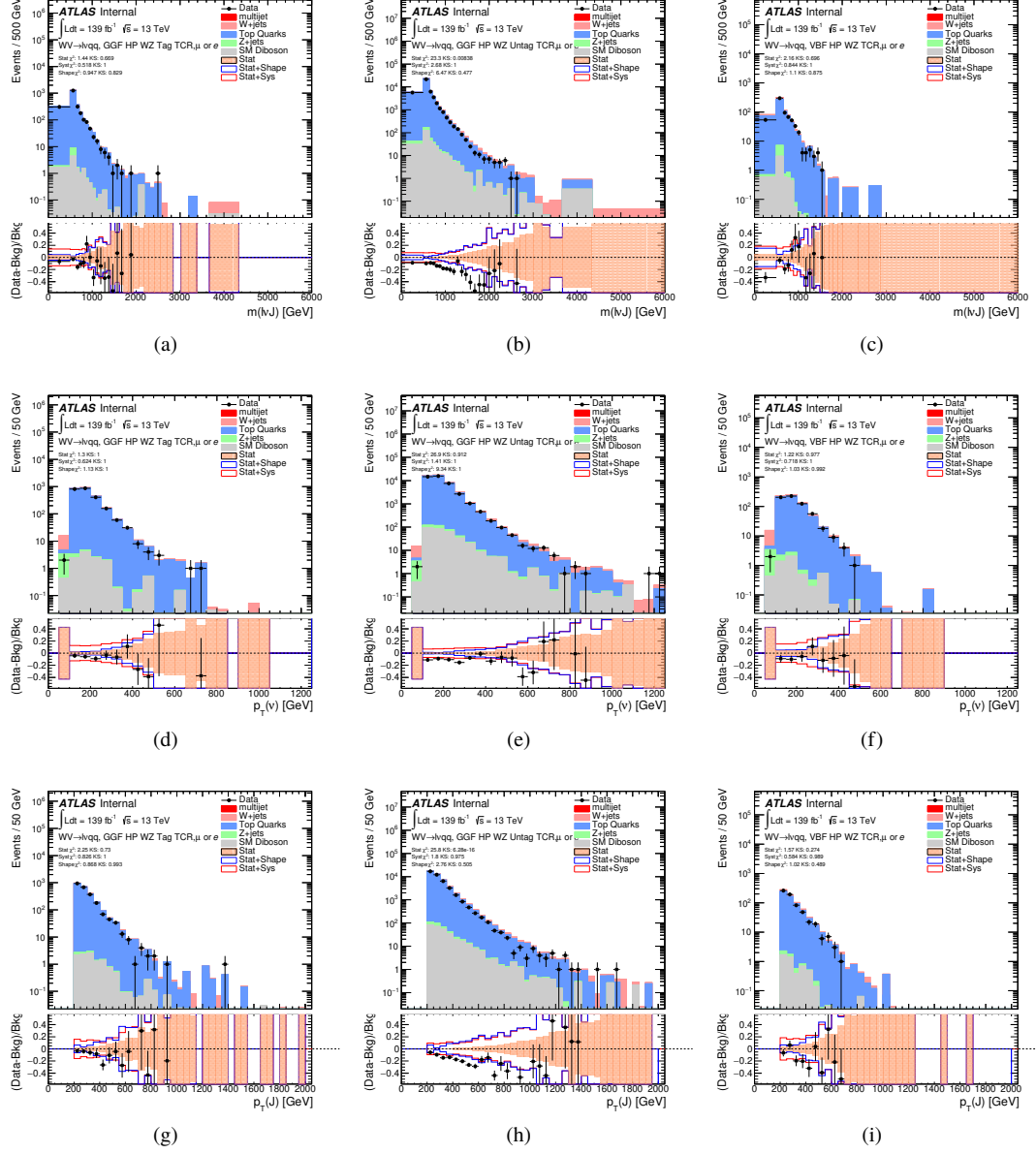


Figure 8.8: Data MC comparison for the merged WZ HP TCR. The bottom panel shows the ratio of the difference between data and simulation to simulation. The red bands include the all systematic and statistical uncertainties on the background.

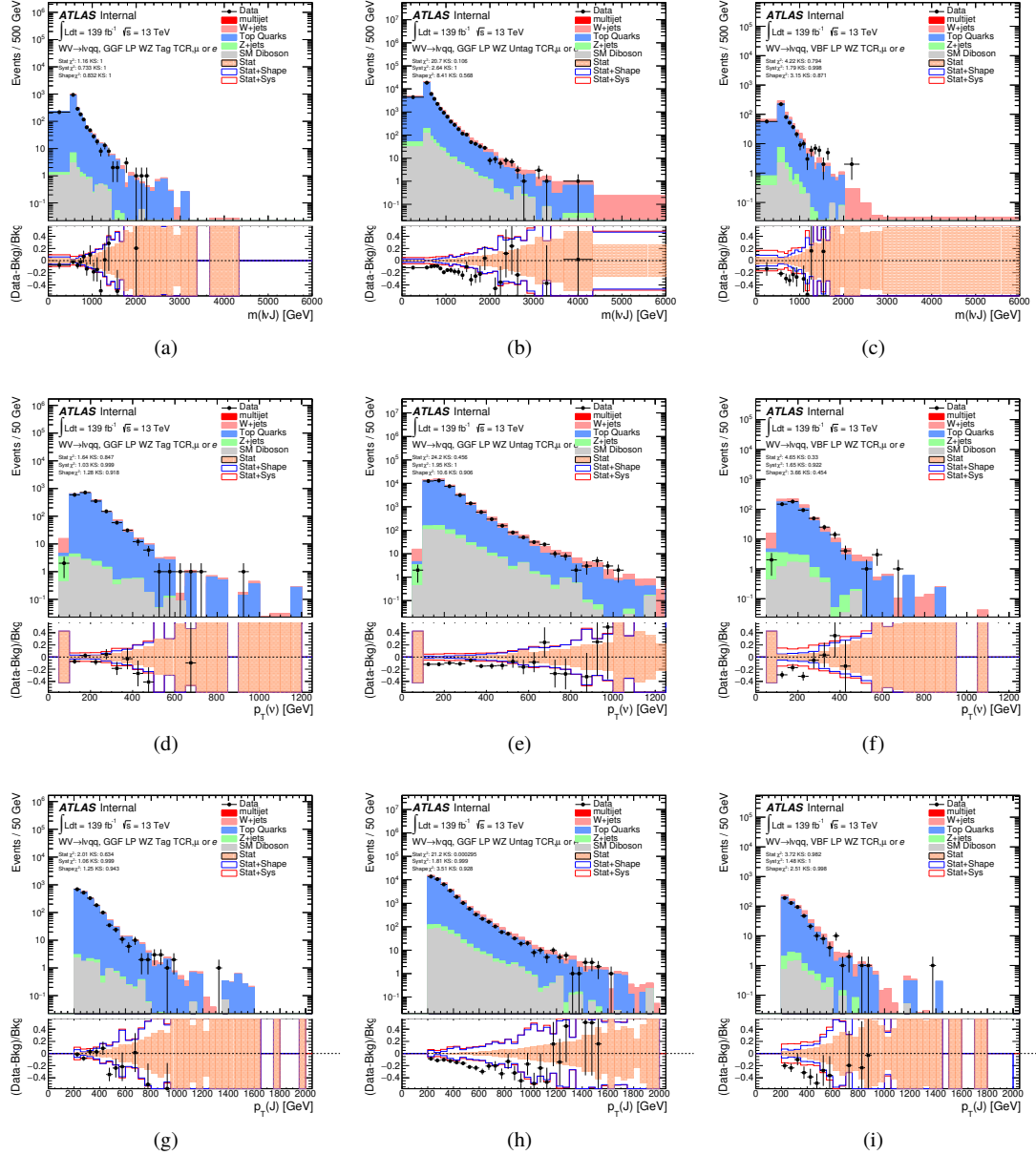


Figure 8.9: Data MC comparison for the merged WZ LP TCR. The bottom panel shows the ratio of the difference between data and simulation to simulation. The red bands include the all systematic and statistical uncertainties on the background.

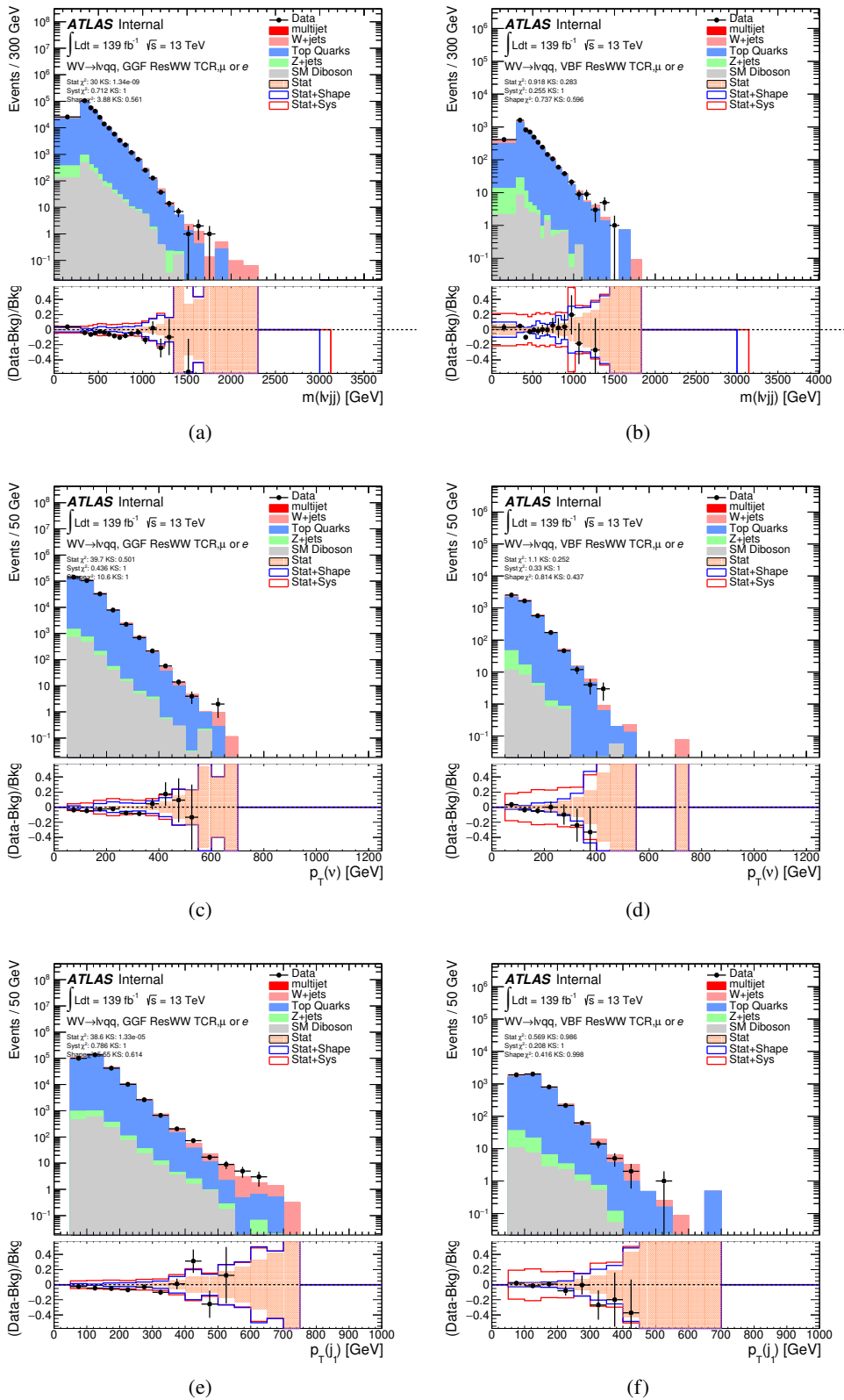


Figure 8.10: Data MC comparison for the resolved WW TCR. The bottom panel shows the ratio of the difference between data and simulation to simulation. The red bands include the all systematic and statistical uncertainties on the background.⁸⁸

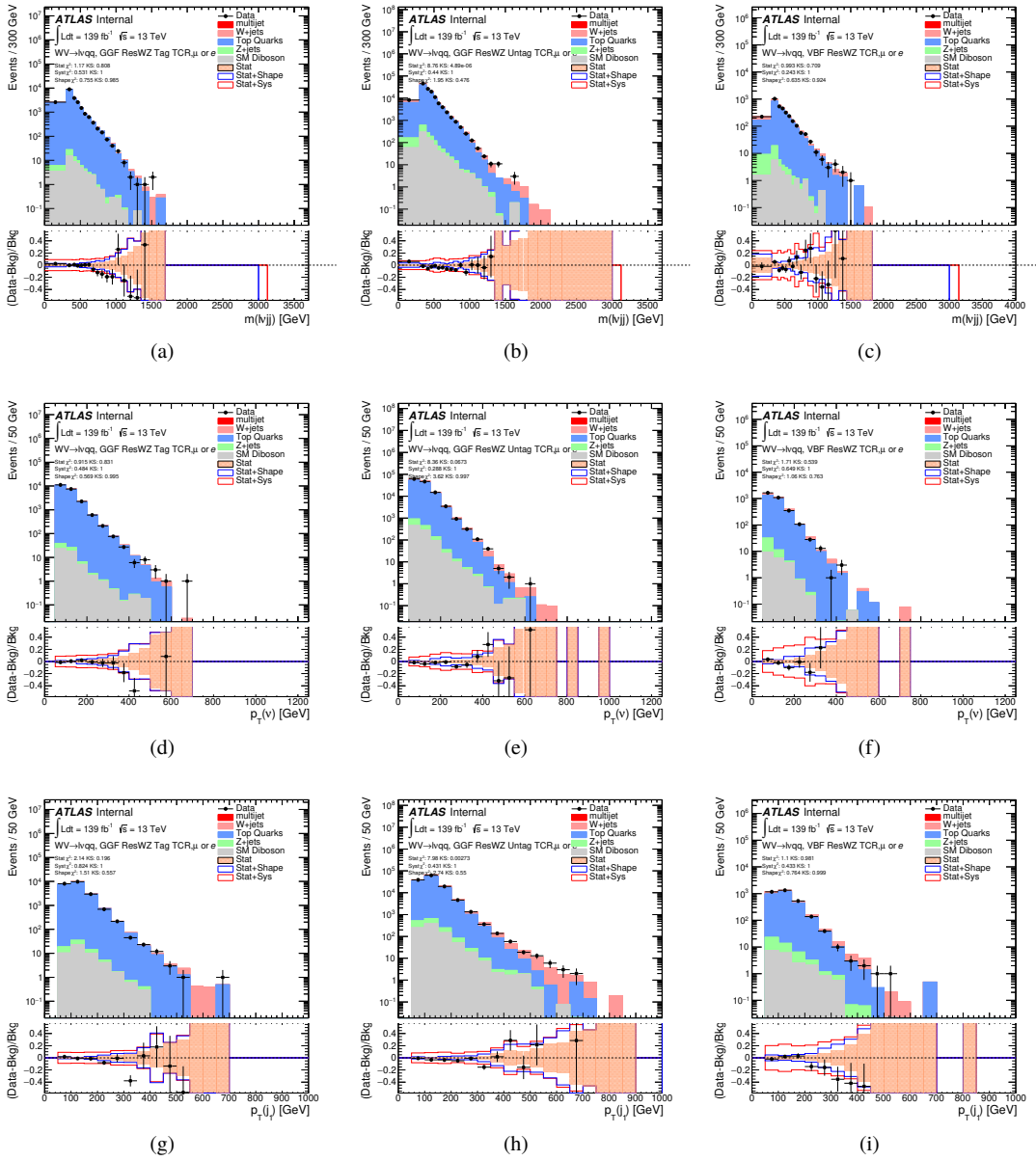


Figure 8.11: Data MC comparison for the resolved WZ TCR. The bottom panel shows the ratio of the difference between data and simulation to simulation. The red bands include the all systematic and statistical uncertainties on the background.

967 **8.5 Selection Acceptance times efficiency for Sig-**
 968 **nal Events**

969 The acceptance times efficiency for the signal region selection is defined as:

$$A \cdot \epsilon = \frac{N_{\text{events selected}}^{\text{truth}}}{N_{\text{events generated}}^{\text{truth}}} \cdot \frac{N_{\text{events selected}}^{\text{reco}}}{N_{\text{events selected}}^{\text{truth}}} = \frac{N_{\text{events selected}}^{\text{reco}}}{N_{\text{events generated}}^{\text{truth}}} \quad (8.3)$$

970 The distributions of $A \cdot \epsilon$ as a function of the resonance mass for the different spin
 971 models are shown in Figures 8.13 - ??.

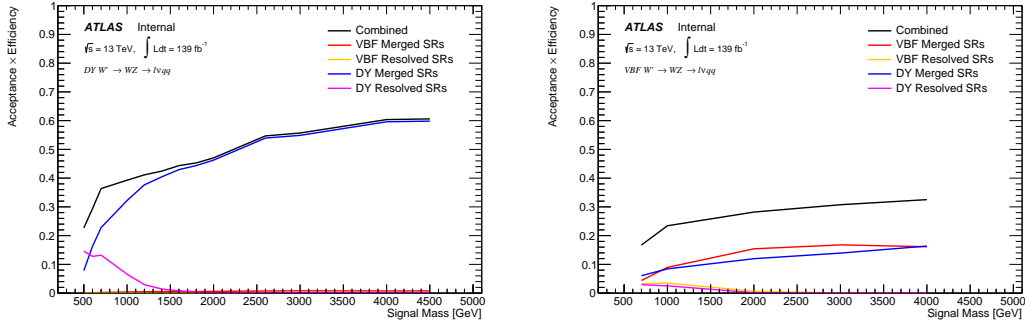


Figure 8.12: Selection acceptance times efficiency for the $W' \rightarrow WZ \rightarrow \ell\nu qq$ events from MC simulations as a function of the W' mass for (a) Drell-Yan and (b) VBF production, combining the merged HP and LP signal regions of the $WW \rightarrow \ell\nu J$ selection and the resolved regions of the $WW \rightarrow \ell\nu jj$ selection.

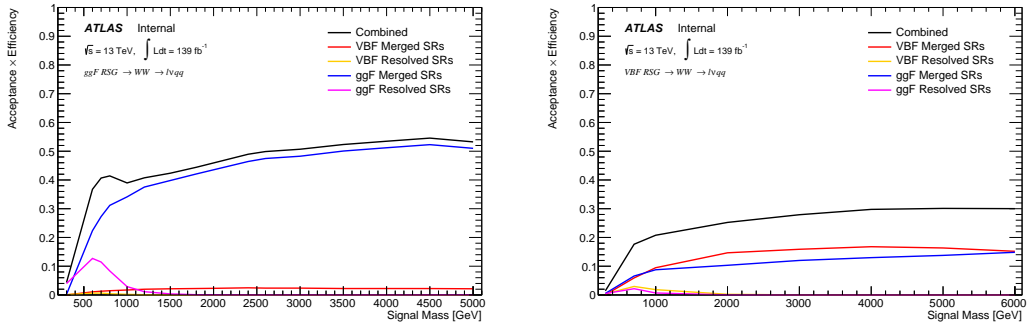


Figure 8.13: Selection acceptance times efficiency for the $G \rightarrow WW \rightarrow \ell\nu qq$ events from MC simulations as a function of the G mass for (a) Drell-Yan and (b) VBF production, combining the merged HP and LP signal regions of the $WW \rightarrow \ell\nu J$ selection and the resolved regions of the $WW \rightarrow \ell\nu jj$ selection.

972 8.6 Background Estimate

973 8.6.1 Control Regions

974 To more accurately model the two dominant backgrounds in this analysis,
 975 $W+jets$ and $t\bar{t}$, control regions are constructed for each. These control regions
 976 are dominated by these processes and used to extract normalization factors in
 977 the final likelihood fit that are then used in the signal region estimates. For the
 978 $t\bar{t}$ control region the event must contain at least one such b jet. The WCR is
 979 constructed using the $m_{jj/J}$ mass window sidebands. All other backgrounds are
 980 estimated using simulation, except fake lepton backgrounds, which are derived
 981 using a data-driven method.

982 8.6.2 Fake Lepton Backgrounds

983 Backgrounds in this analysis containing real leptons (e.g. $W/Z+jets$, diboson,
 984 $t\bar{t}$, single- t) are well-modeled with simulated samples and constrained with data
 985 from CRs. However, the fake lepton background (also referred to as the multijet
 986 background) is not well-modeled with simulation. For this reason, the multijet

987 background is extracted from data. Heavy flavor decay products, jets, and con-
988 verted photons can be mistakenly reconstructed as electrons. Fake electrons often
989 arise from jet fakes while non-prompt muons usually arise from heavy flavor decay.
990 For this analysis, these fake electrons generally fail the electron ID criteria and
991 fake muons fail the muon isolation requirement. Therefore, to derive the multijet
992 template shape the SR and CR selections and inverted lepton requirements are
993 used as seen in Table 8.4. NB: by inverting the lepton isolation/identification
994 criteria the SRs and CRs are orthogonal.

995 The template shape of the MJ background is determined by using a multijet
996 validation region (MJVR) that requires the inverted lepton isolation/identification
997 requirement and the two signal jets to satisfy the m_{jj} requirement used in the
998 $W+jets$ CRs. The E_T^{miss} distribution in MJCR is shown in Figure 8.14 for 2017
999 data. The template is then extracted by subtracting the data in the MJVR from
1000 the electroweak background processes. The resulting template and electroweak
1001 backgrounds are then fit to data. In this fit, the E_T^{miss} distribution compared to
1002 data to extract electroweak background, multijet electron and muon background
1003 normalizations. The fitted scale factors from this MJVR template are then applied
1004 in the MJCR template. The electron and muon background normalizations in the
1005 MJCR template are parameters in the final simultaneous fit. Technically, there
1006 should be a separate template for every CR and SR, but some MJ regions have
1007 insufficient statistics to do this. Additionally, the shapes for the MJ templates for
1008 VBF and ggF regions are found to be compatible within statistical uncertainty.
1009 Therefore, the sample MJ template used for VBF and ggF CR/SRs, but with
1010 different pre-MJ-fit scale factors.

1011 This template method was validated using WCR and full Run 2 data. The
1012 results of the fit are shown in Table 8.5. The multijet contribution in the muon

1013 channel for $p_T^W > 150$ GeV is consistent with zero, and therefore neglected in
 1014 the final fit. Applying the extracted normalization factor to MJVR in WCRs for
 1015 various kinematic variables such as E_T^{miss} , W transverse mass, lepton p_T , and the
 1016 invariant mass as show in Figures 8.15 -8.24. These figures show good agreement
 1017 between the data and background estimate.

Table 8.4: Definitions of “inverted” leptons used in multijet control region

	Criterion	signal lepton	inverted lepton
Electron	ID	TightLH	MediumLH !TightLH
	Calo Isolation	FixedCutHighPtCaloOnlyIso	FixedCutHighPtCaloOnlyIso
Muon	ID	WHSignalMuon	WHSignalMuon
	Track Isolation	FixedCutTightTrackOnlyIso	!FixedCutTightTrackOnlyIso $ptvarcone30/pt < 0.07^*$
*Only applied to events with $pTW < 150\text{GeV}$			

1018

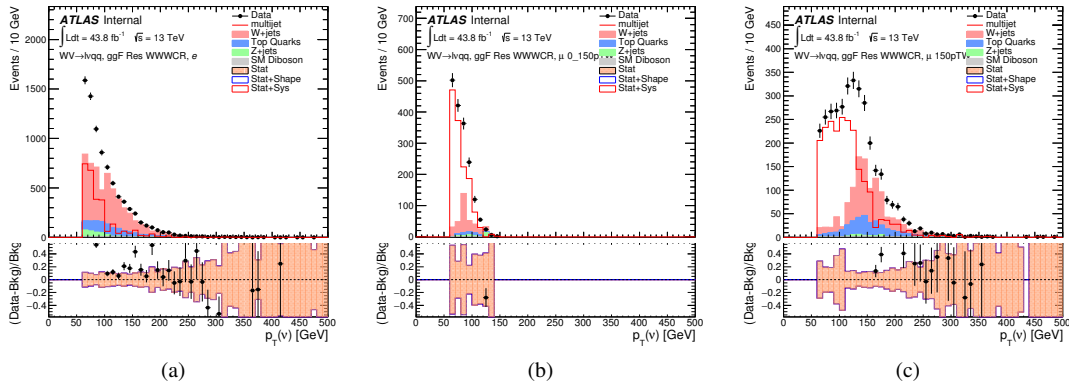


Figure 8.14: The E_T^{miss} distribution in MJCR for 2017 data in the electron channel(left), muon channel with W -boson $p_T < 150$ GeV (center) and > 150 GeV (right). Multi-jet templates are calculated as remaining data components after excluding known MC

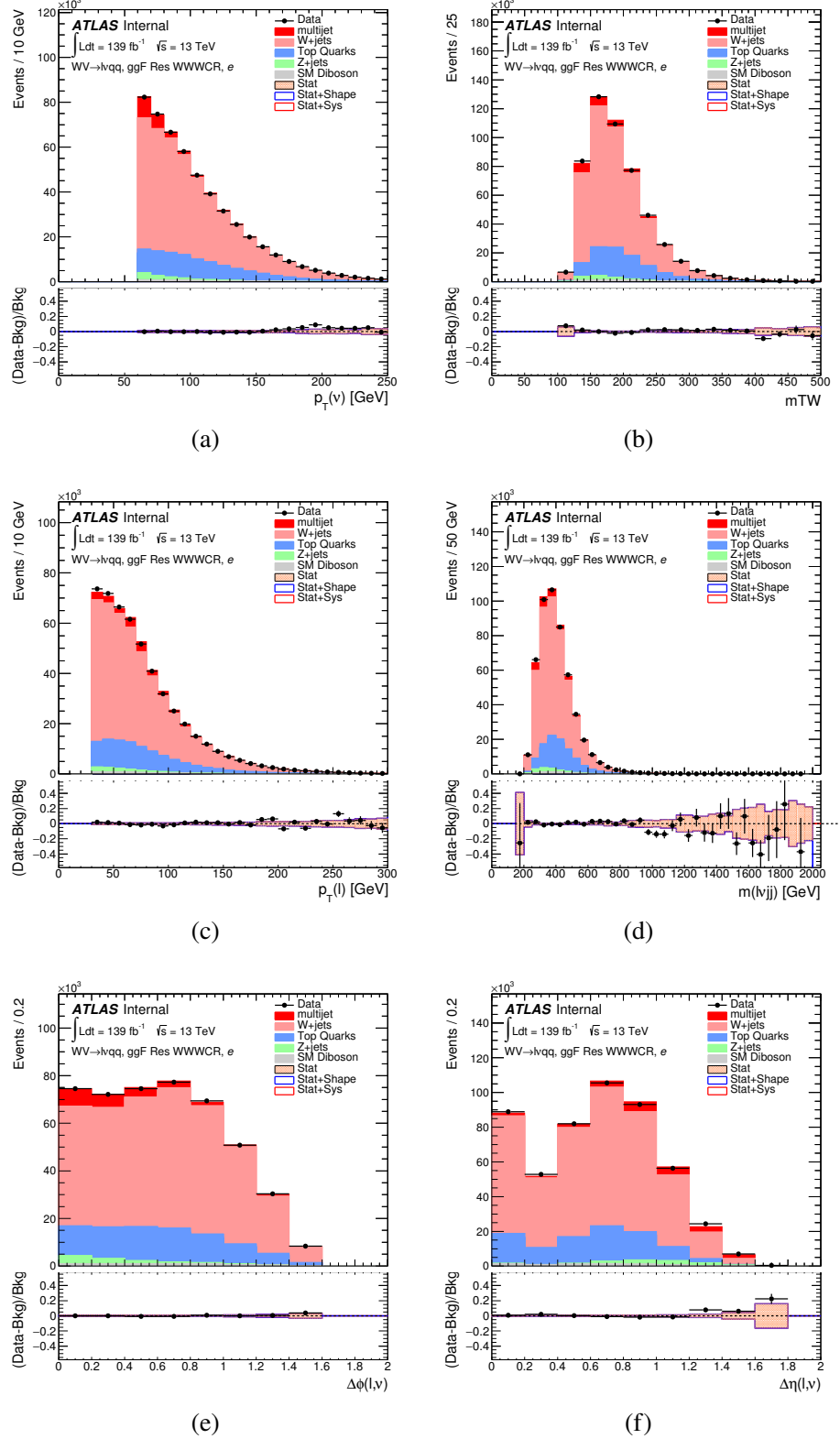


Figure 8.15: Postfit Data/MC comparison of distributions of E_T^{miss} , m_T^W , lepton and neutrino p_T , $m_{\ell\nu jj}$, lepton- ν angular distance in the WW electron channel. The MJ template is obtained from the pre-MJ-fit.

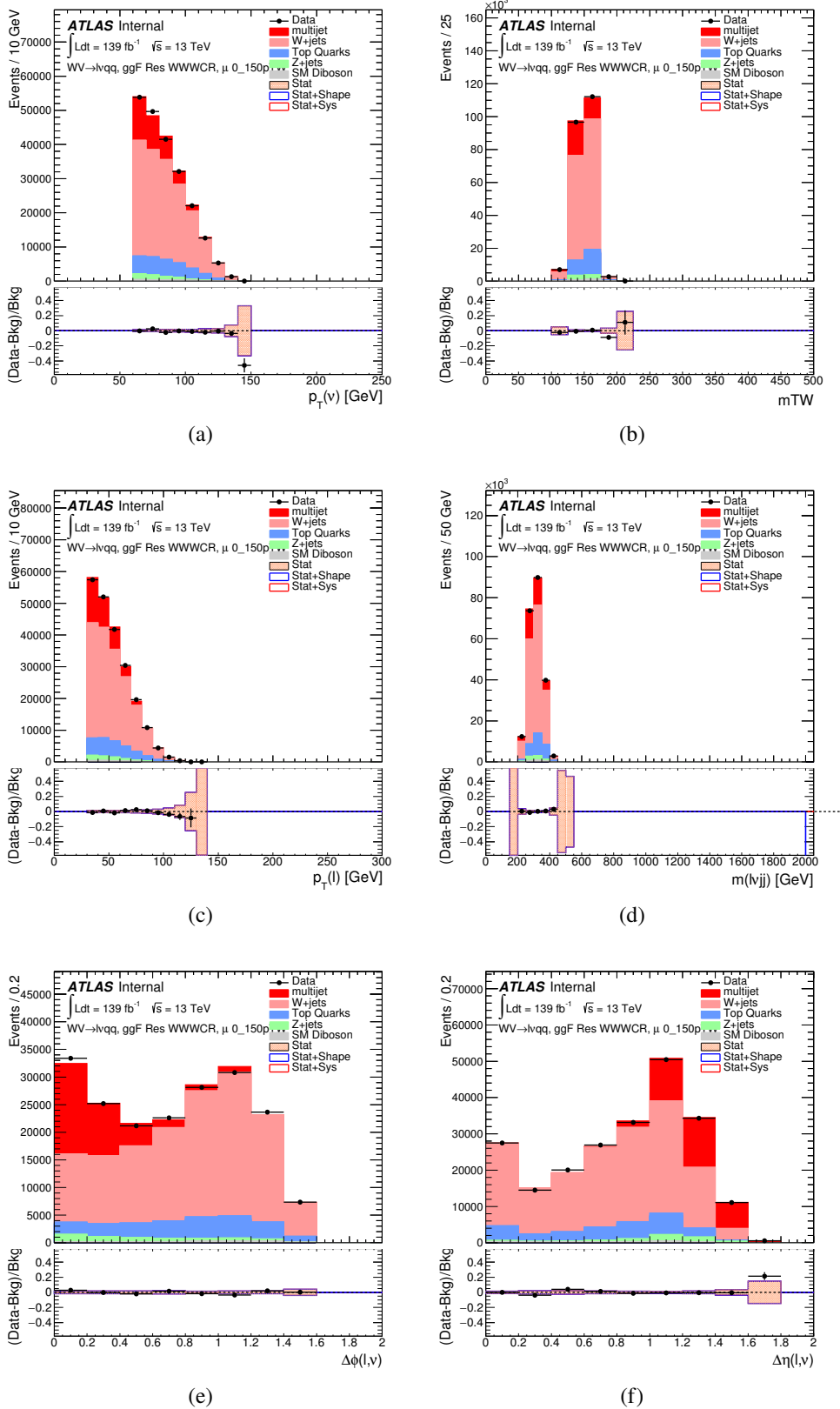


Figure 8.16: Postfit Data/MC comparison of distributions of E_T^{miss} , m_T^W , lepton and neutrino p_T , $m_{l\nu jj}$, lepton- ν angular distance in the WW muon channel. The MJ template is obtained from the pre-MJ-fit.

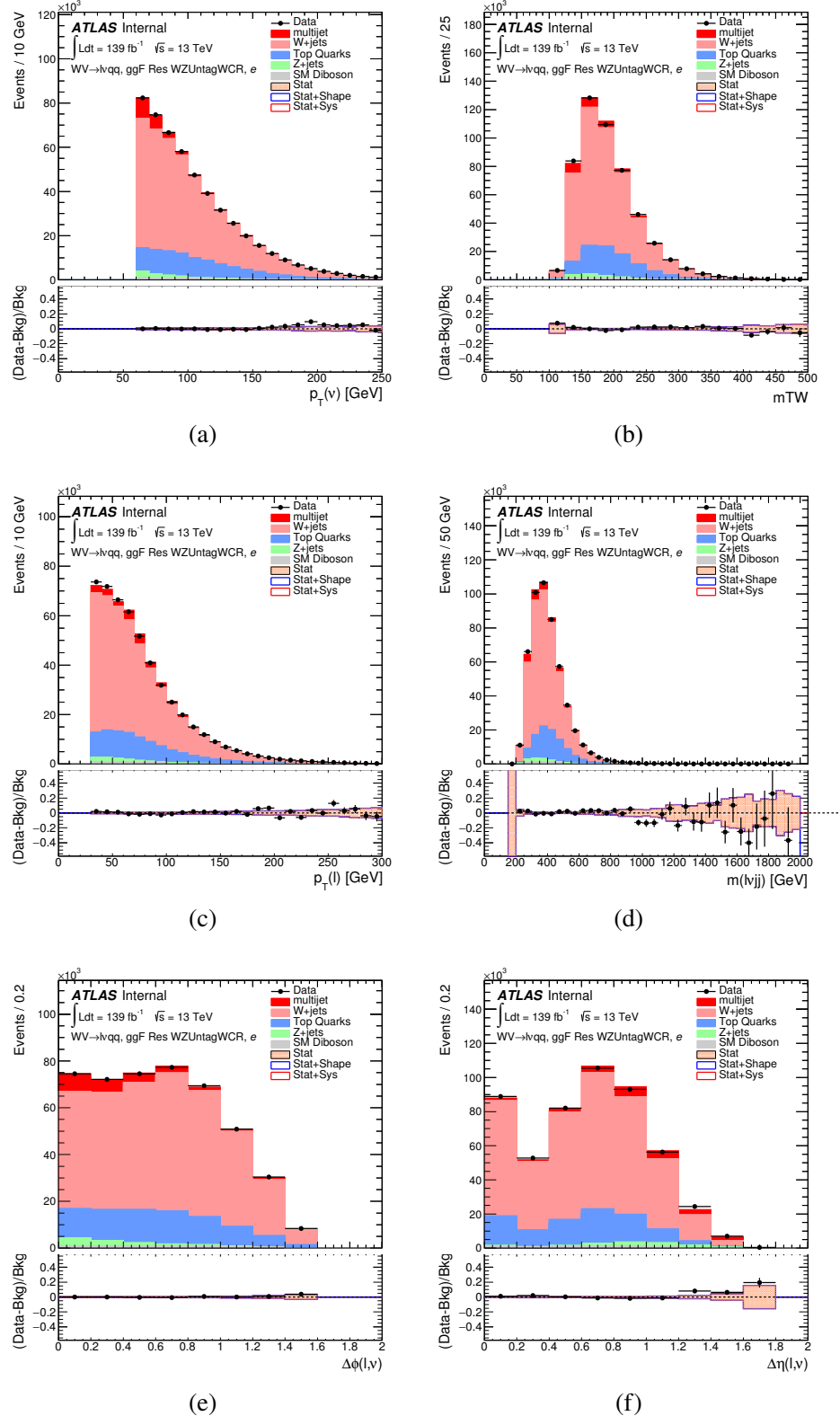


Figure 8.17: Postfit Data/MC comparison of distributions of E_T^{miss} , m_T^W , lepton and neutrino p_T , $m_{l\nu jj}$, lepton- ν angular distance in the WZ untag electron channel. The MJ template is obtained from the pre-MJ-fit.

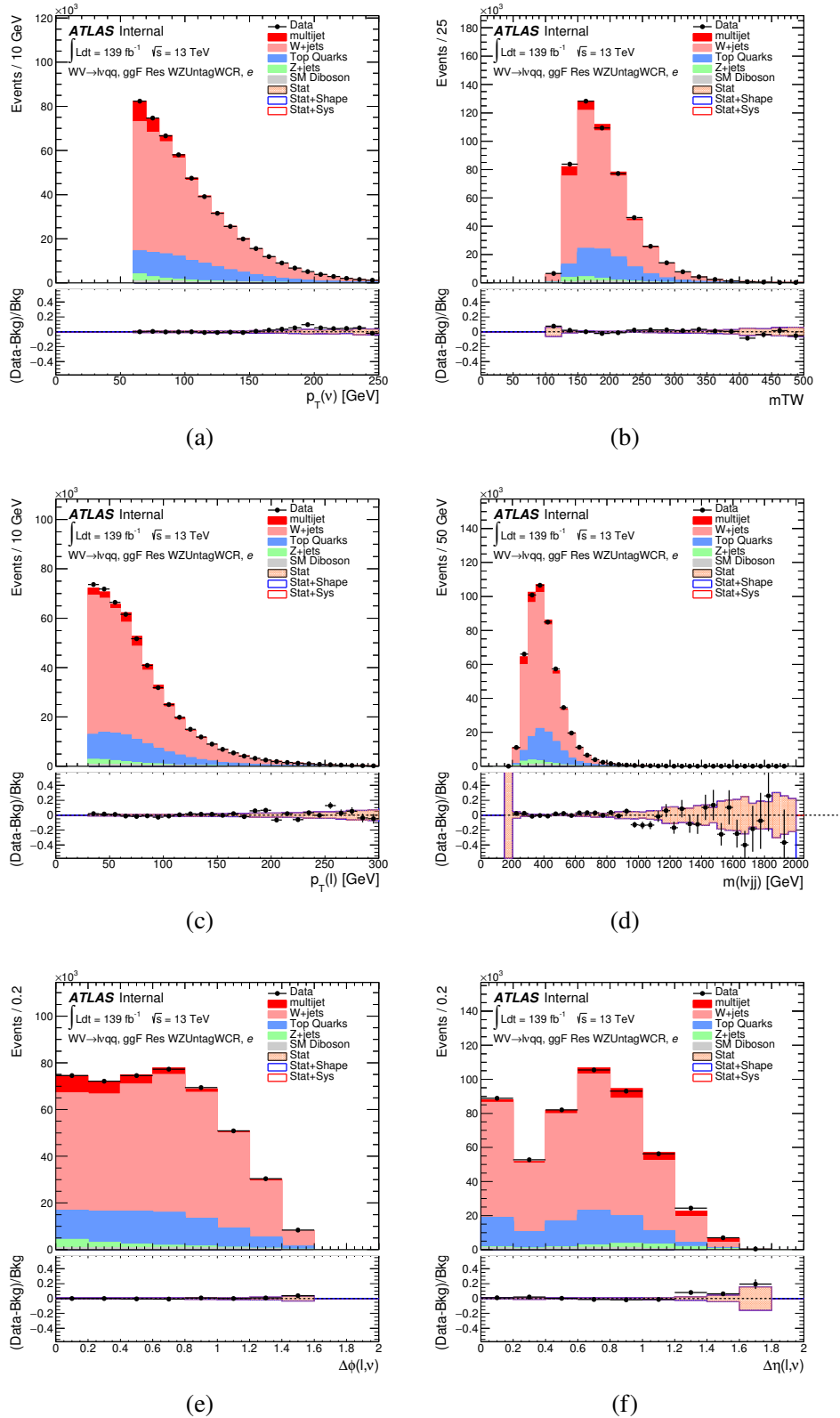


Figure 8.18: Postfit Data/MC comparison of distributions of E_T^{miss} , m_T^W , lepton and neutrino p_T , $m_{\ell\nu jj}$, lepton- ν angular distance in the WZ untag muon channel. The MJ template is obtained from the pre-MJ-fit.

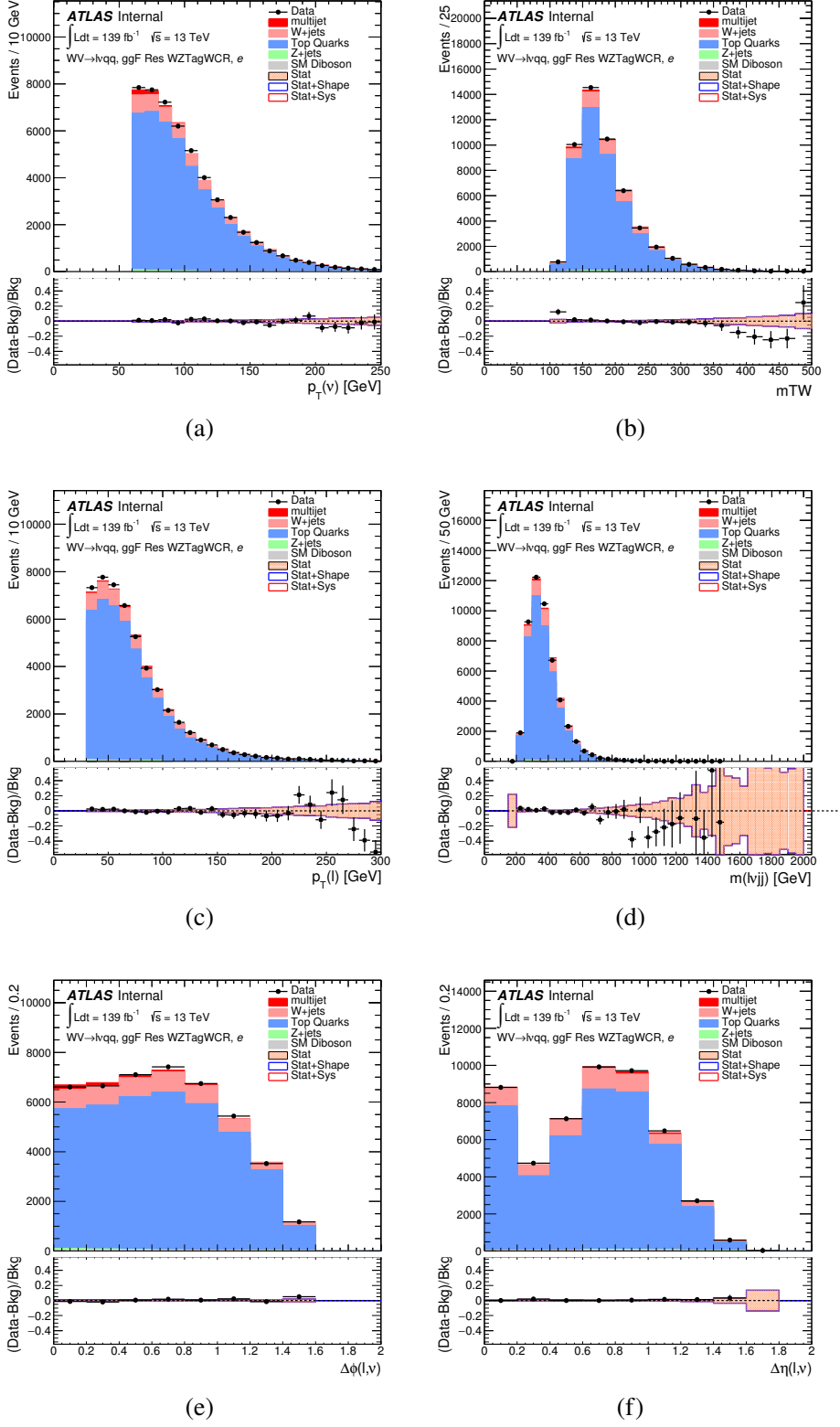


Figure 8.19: Postfit Data/MC comparison of distributions of E_T^{miss} , m_T^W , lepton and neutrino p_T , $m_{l\nu jj}$, lepton- ν angular distance in the WZ untag electron channel. The MJ template is obtained from the pre-MJ-fit.

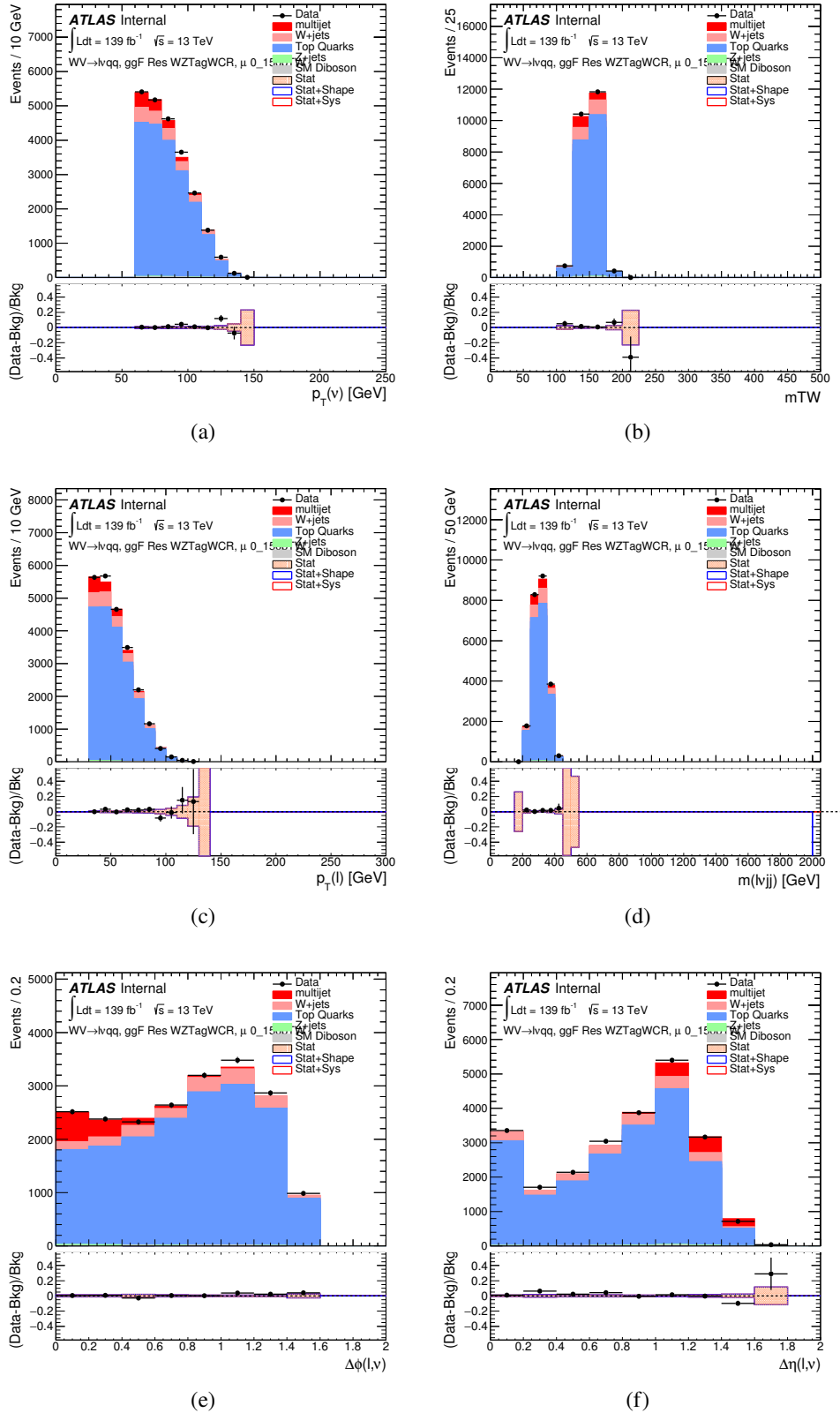


Figure 8.20: Postfit Data/MC comparison of distributions of E_T^{miss} , m_T^W , lepton and neutrino p_T , $m_{\ell\nu jj}$, lepton- ν angular distance in the WZ untag muon channel. The MJ template is obtained from the pre-MJ-fit.

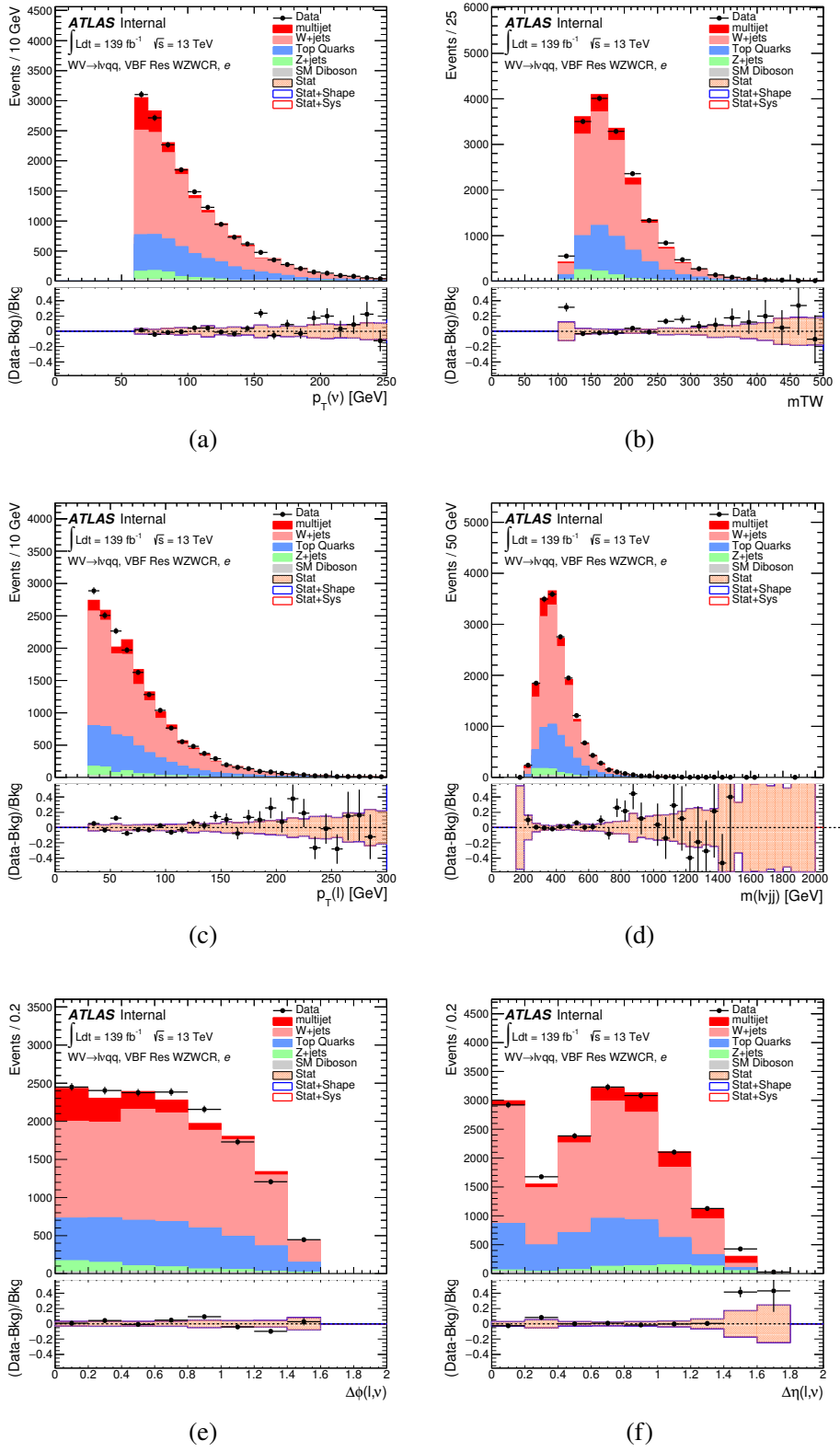


Figure 8.21: Postfit Data/MC comparison of distributions of E_T^{miss} , m_T^W , lepton and neutrino p_T , $m_{l\nu jj}$, lepton- ν angular distance in the VBF WW electron channel. The MJ template is obtained from the pre-MJ-fit.

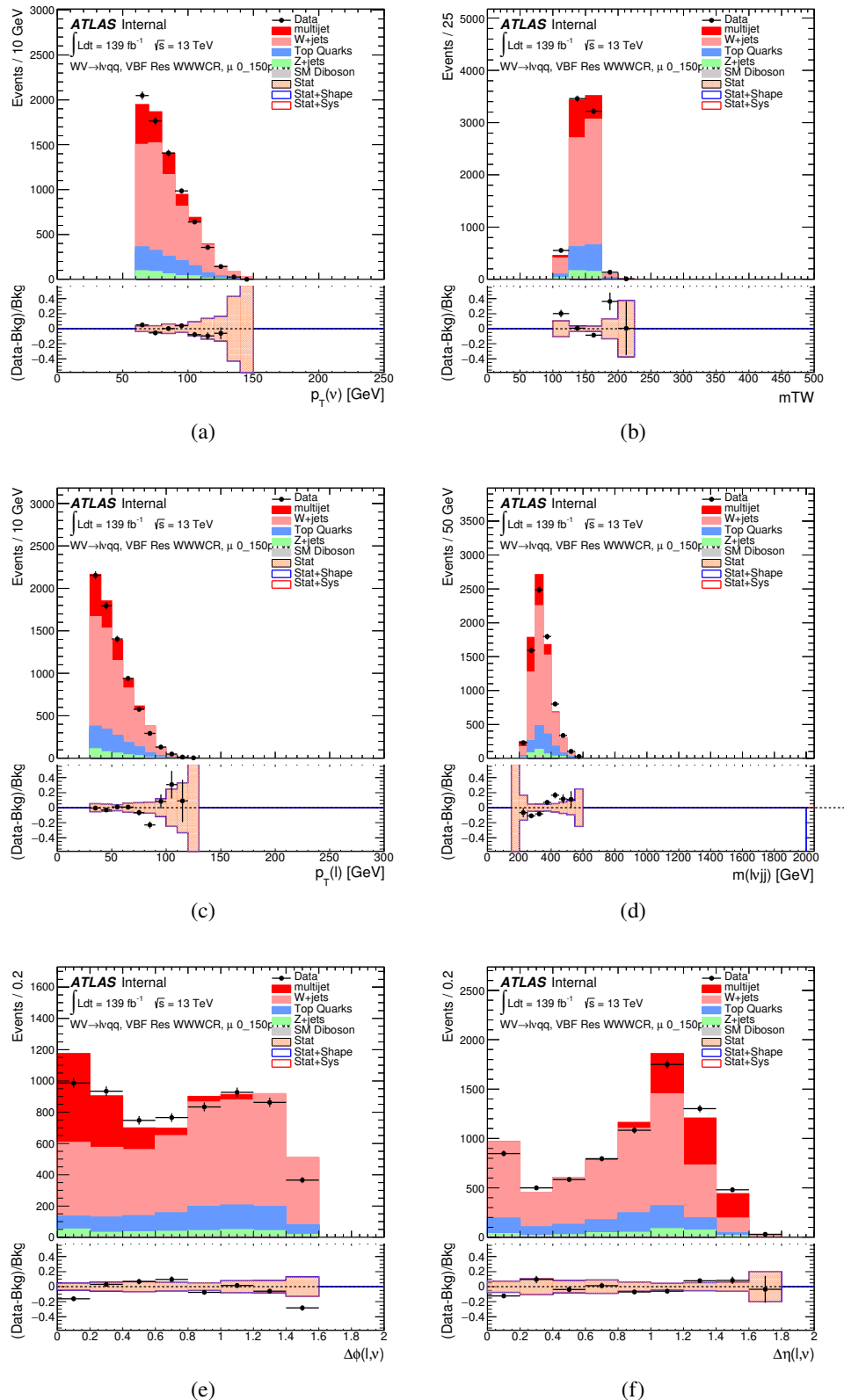


Figure 8.22: Postfit Data/MC comparison of distributions of E_T^{miss} , m_T^W , lepton and neutrino p_T , $m_{\ell\nu jj}$, lepton- ν angular distance in the VBF WW muon channel. The MJ template is obtained from the pre-MJ-fit.

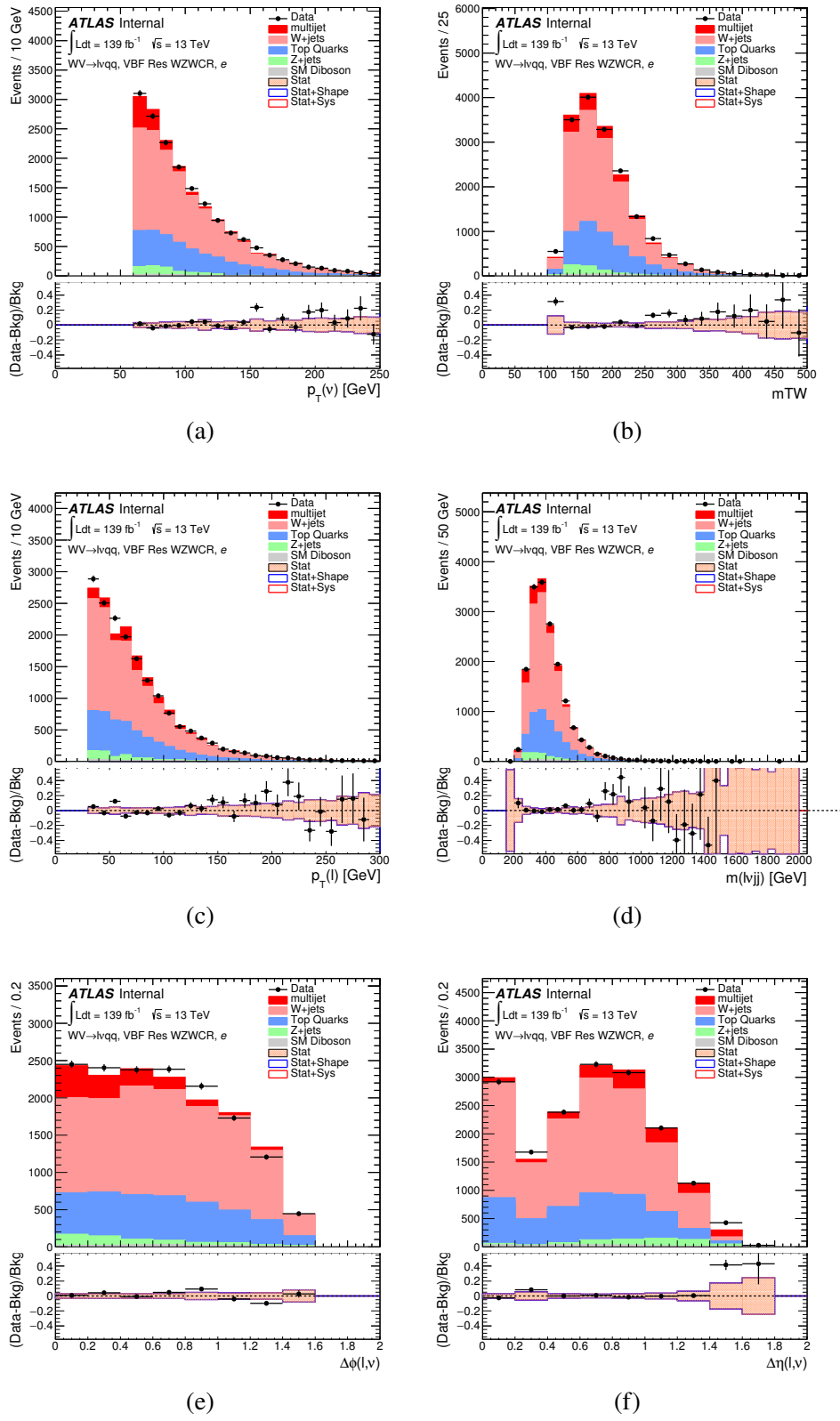


Figure 8.23: Postfit Data/MC comparison of distributions of E_T^{miss} , m_T^W , lepton and neutrino p_T , $m_{l\nu jj}$, lepton- ν angular distance in the VBF WZ electron channel. The MJ template is obtained from the pre-MJ-fit.

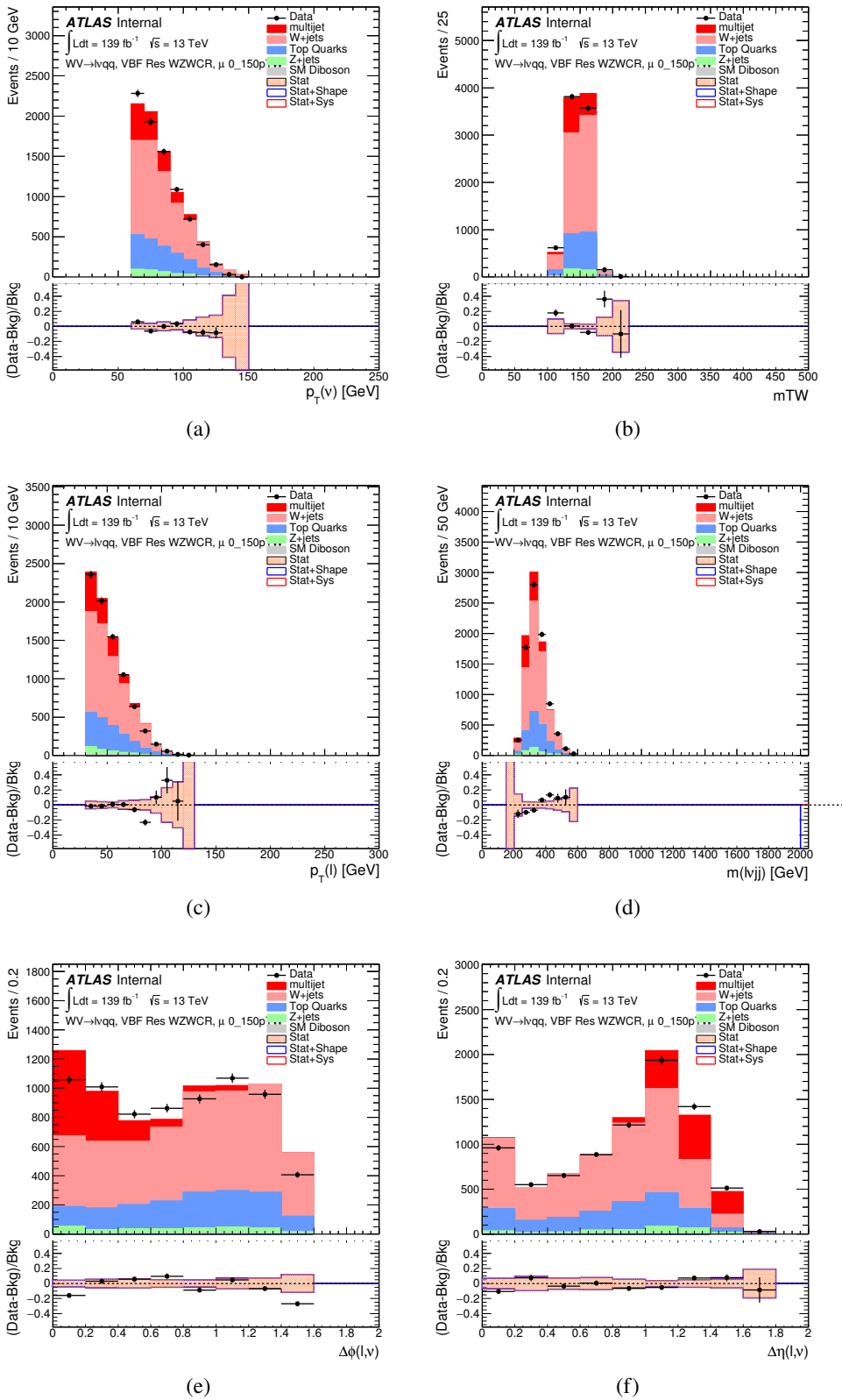


Figure 8.24: Postfit Data/MC comparison of distributions of E_T^{miss} , m_T^W , lepton and neutrino p_T , $m_{l\nu jj}$, lepton- ν angular distance in the VBF WZ muon channel. The MJ template is obtained from the pre-MJ-fit.

Full Run 2
ggF Res WWWCR

Sample	Yield	R.U.	SF
Top&W	645040 ± 1971.68	0.31%	0.998
Z&VV	24075.9		fixed
MJ_el	24156.3 ± 1224.62	5.06%	3.973
MJ_mu	35528.5 ± 923.94	2.60%	9.019

ggF Res WZ01bWCR

Sample	Yield	R.U.	SF
Top&W	644690 ± 1981.4	0.31%	0.997
Z&VV	24075.9		fixed
MJ_el	24366.5 ± 1232.69	5.05%	3.874
MJ_mu	35528.5 ± 921.27	2.58%	8.746

ggF Res WZ2bWCR

Sample	Yield	R.U.	SF
Top&W	71236.5 ± 688.74	0.97%	1.031
Z&VV	518.5		fixed
MJ_el	595.63 ± 449.34	75.44%	0.094
MJ_mu	1196.9 ± 222.13	18.56%	0.294

VBF Res WWWCR

Sample	Yield	R.U.	SF
Top&W	19032.3 ± 364.43	1.91%	0.928
Z&VV	1091.63		fixed
MJ_el	1425.73 ± 214.42	15.03%	0.235
MJ_mu	1281.36 ± 157.21	11.83%	0.314

VBF Res WZWCR

Sample	Yield	R.U.	SF
Top&W	21341.8 ± 392.21	1.84%	0.942
Z&VV	1111.75		fixed
MJ_el	1413.76 ± 230.36	16.29%	0.225
MJ_mu	1281.36 ± 157.21	12.27%	0.314

Table 8.5: Fit validation result in WCRs for 2015+16 data. The fit is done in various WCRs, in order to obtain the corresponding scale factors for MJ templates: ggF resolved WCR for the $WW \rightarrow lvqq$ selection, ggF resolved untagged WCR for the $WZ \rightarrow lvqq$ selection, ggF resolved tagged WCR for the $WZ \rightarrow lvqq$ selection, VBF resolved WCR for the $WW \rightarrow lvqq$ selection, and VBF resolved WCR for the $WZ \rightarrow lvqq$ selection. Post-fit event yields for electroweak processes and MJ contributions are shown. The SF column shows the corresponding normalization scale factors for electroweak processes from the fit. R.U. stands for relative uncertainty.

1019 **Chapter 9**

1020 **Systematic Uncertainties**

1021 This section describes the sources of systematic uncertainties considered in
1022 this analysis. These uncertainties are divided into three categories: experimental
1023 uncertainties, background modeling uncertainties, and theoretical uncertainties on
1024 signal processes. In the statistical analysis each systematic uncertainty is treated
1025 as a nuisance parameter estimated on the m_{VV} distribution.

1026 **9.1 Experimental Systematics**

1027 The uncertainty on the integrated luminosity of the dataset used is 1.7% and
1028 a systematic in the final fit. This uncertainty was calculated using $x - y$ beam
1029 separation scans [ref P55].

1030 An additional source of systematic uncertainty is assigned to the pileup mod-
1031eling in MC samples. This ensures simulated detector response and particle re-
1032construction conditions are as similar as possible. The distribution of the average
1033 number of interactions per bunch crossing applied to simulation is called the μ pro-
1034file. The pileup modeling uncertainty is accounted for by re-weighting simulated
1035events so the average number of interactions per bunch crossing varies within its

1036 uncertainty due to systematics from vertex reconstruction [ref ATL-COM-SOFT-
1037 2015-119]. The associated re-weighting factors are propagated through the entire
1038 analysis chain to construct a systematic uncertainty on m_{VV} .

1039 The single-lepton and E_T^{miss} triggers used are not fully efficient, so scale factors
1040 are applied to simulation to more accurately model the data. These scale factors
1041 are given by the ratio of the distribution of offline objects before trigger selection
1042 and after trigger selection. The associated uncertainty on these scale factors are
1043 used in the final fit.

1044 Uncertainties on small-R jet energy scale and resolution are measured in-situ
1045 by calculating the response between data and simulation. This analysis uses a
1046 reduced set of JES and JER uncertainties (totaling 30 and 8 systematics, re-
1047 spectively). These reduced sets of systematics are calculated using a principal
1048 component analysis, yield largely uncorrelated independent systematics. These
1049 uncertainties on JES and JER account for the dependence on p_T , η , μ , flavor re-
1050 sponse and global sequential corrections. Systematic uncertainties associated with
1051 b -tagging are also considered. These systematics are evaluated as uncertainties on
1052 the scale factor which account for the difference in b -tagging efficiencies in data
1053 and MC, and the flavor dependence (between b, c, and light jets).

1054 The uncertainty on the p_T scale of the large-R jets is determined by comparing
1055 the jet's p_T^{calo} to p_T^{track} in di-jet simulation and data. In addition to this uncertain-
1056 ties from tracking, modeling (Pythia vs Herwig), and statistical constraints are
1057 also calculated. The large-R jet p_T resolution is given by smearing the jet p_T with
1058 a Gaussian with a 2% width.

1059 The W/Z tagging efficiency SF is estimated by comparing the tagging efficiency
1060 in simulation with that in data for four regions of the W/Z tagger (D_2 fail, m_J
1061 fail; D_2 pass, m_J fail; D_2 fail, m_J pass; D_2 pass, m_J pass). (Additionally, separate

1062 scale factors are determined for events with large-R jets from W bosons and top
 1063 backgrounds.) A simultaneous template fit is used to fit the signal jets (jets
 1064 initiated by W/Z bosons or top quarks) and background jets (all other jets from
 1065 the simulated backgrounds) to the data in the four regions. The SF for a given
 1066 region is then given by:

$$SF = \frac{\epsilon_{data} = \frac{N_{fitted\text{-}signal}^{region}}{N_{fitted\text{-}signal}^{all\text{-}regions}}}{\epsilon_{MC} = \frac{N_{signal}^{region}}{N_{signal}^{all\text{-}regions}}} \quad (9.1)$$

1067 The W/Z -tagging SF is estimated in data using a control sample and cor-
 1068 rected by comparing it with simulation. The efficiency to W/Z -induced signal is
 1069 estimated by a $t\bar{t}$ control sample, while the efficiency to single- q/g background
 1070 is estimated using a dijet sample. The effects of experimental and theoretical
 1071 uncertainties on the efficiency scale factor are determined by taking the ratio of
 1072 efficiencies in data and simulation. By taking this ratio the uncertainties not
 1073 arising for jet mass and D_2 cancel.

1074 Lepton identification, reconstruction, isolation systematic uncertainties are de-
 1075 termined by reconstructing the Z mass peak with a tag and probe method. The
 1076 lepton energy and momentum scales are also measured with the Z mass peak.
 1077 Additionally, the track-to-vertex association efficiency is used for muons.

1078 As E_T^{miss} is calculated using all the physics objects in the event, all those objects
 1079 associated errors result in an uncertainty on E_T^{miss} . Additionally, the unassociated
 1080 tracks used to construct E_T^{miss} contribute to the uncertainty on E_T^{miss} .

1081 9.2 Theory Systematics

1082 Theoretical uncertainties for signal and background processes arise from un-
1083 certainties in the parameters used in Monte Carlo simulation. In particular for
1084 the $t\bar{t}$, $W/Z + \text{jets}$, diboson backgrounds and signal samples, the QCD scale, PDF,
1085 generator and hadronization uncertainties were evaluated. To assess the QCD
1086 scale uncertainty the renormalization and factorization scales were scaled up and
1087 down by a factor of two at the event generation stage of sample production. Un-
1088 certainties due to the choice of the parton distribution functions were evaluated by
1089 re-weighting samples from the nominal PDF to a set of error PDFs which account
1090 for the uncertainty of the fits used to produce the PDF set. In addition to this,
1091 samples are re-weighted to different PDF sets to account for the arbitrariness of
1092 the PDF choice. The difference between the m_{WV} distributions using different
1093 event generators is assessed by comparing samples generated with different gen-
1094 erators. Similarly, the uncertainty in hadronization models is accounted for by
1095 comparing samples created using different hadronization models (e.g. $t\bar{t}$ Powheg
1096 is compared to AMC@NLO, $W + \text{jets}$ compares Sherpa and MadGraph+Pythia
1097 samples). Figures 9.2 - 9.8 show the impact of these uncertainties on the $t\bar{t}$ and
1098 $W/Z + \text{jets}$ backgrounds. Additionally, contributions to the diboson background
1099 for the VBF analysis were found to be small and were accounted for by including
1100 a 5(10)% systematic in the diboson normalization in the final fit.

1101 The normalization of the $t\bar{t}$ and $W+\text{jets}$ processes impact the multijet tem-
1102 plate shape. The impact of these normalizations was assessed by including a
1103 shape systematic on the multijet background from varying the $t\bar{t}$ and $W+\text{jets}$
1104 normalization factors.

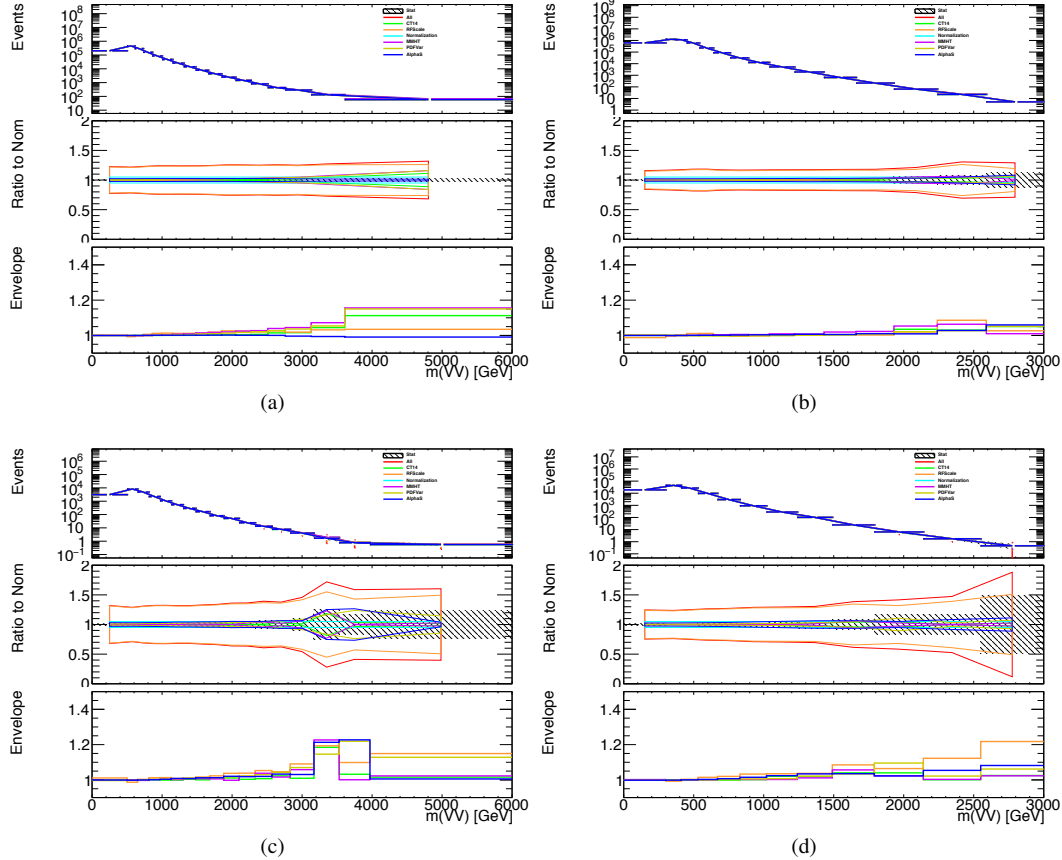


Figure 9.1: The $W/Z + \text{jet}$ systematics for the a) Merged ggF, b) Resolved ggF, c) Merged VBF, and d) Resolved VBF regions. The top subplot shows the nominal and variation distributions/bands, the middle shows the ratio of the two, and the final shows just the shape of the envelope (the final uncertainty).

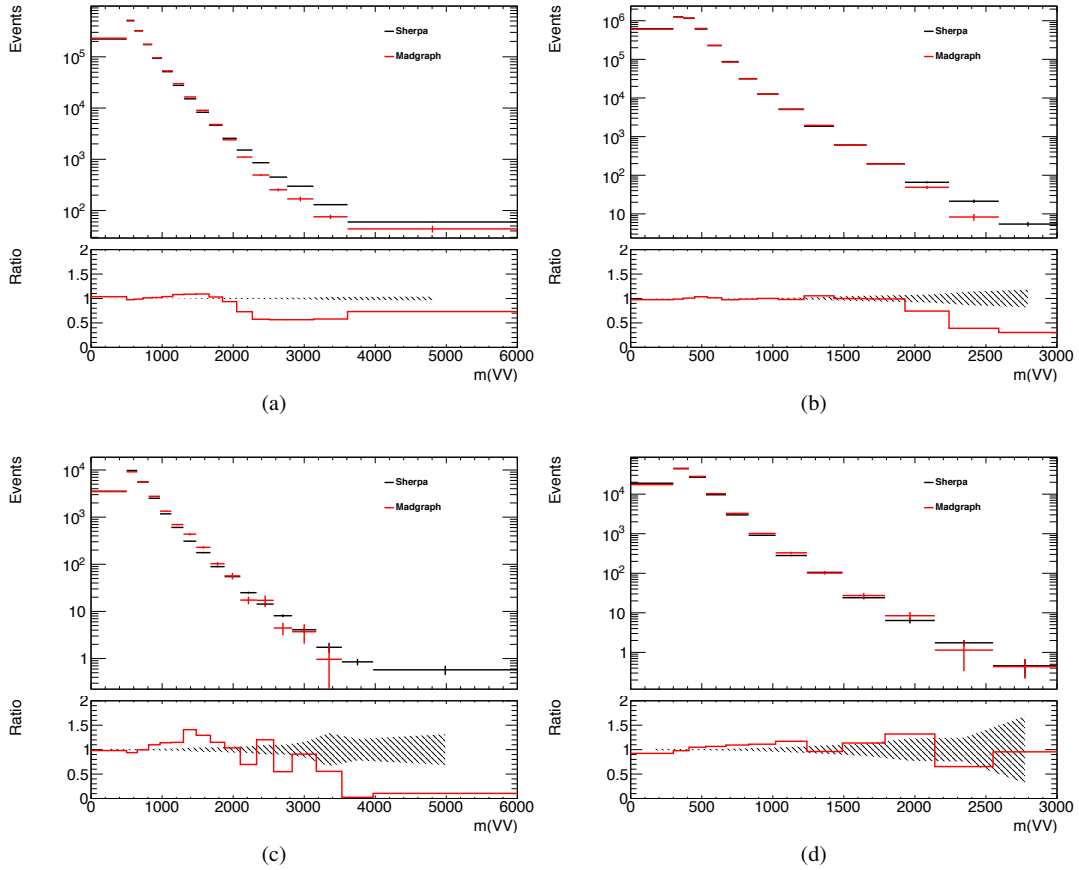


Figure 9.2: The two-point generator comparison between Sherpa and MadGraph for the $W/Z + \text{jet}$ samples in the a) Merged ggF, b) Resolved ggF, c) Merged VBF, and d) Resolved VBF regions. The normalization of the Madgraph sample is set to the Sherpa value to consider only shape effects. The bottom inset shows the ratio of the two.

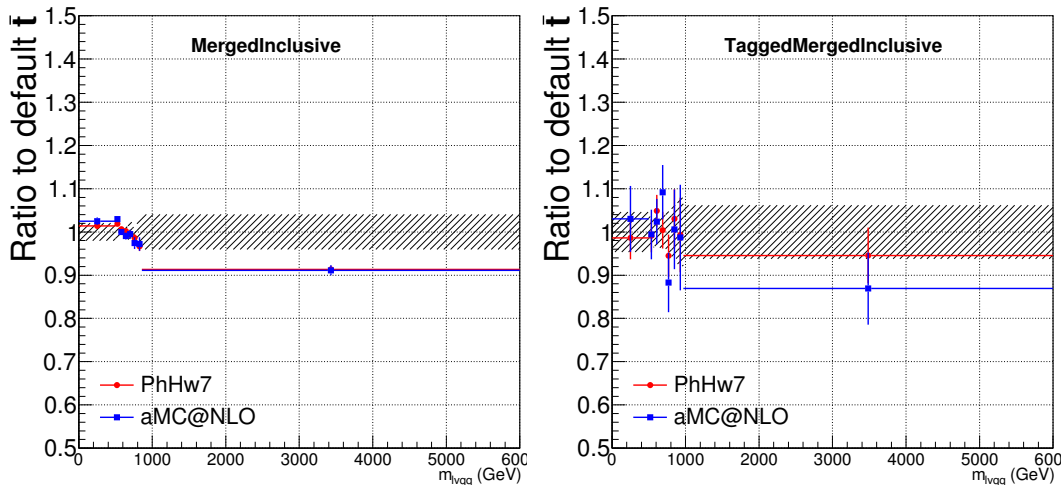


Figure 9.3: Ratio between the variations of generator (red) and hadronization (blue) variations for the Merged regime for $t\bar{t}$ sample.

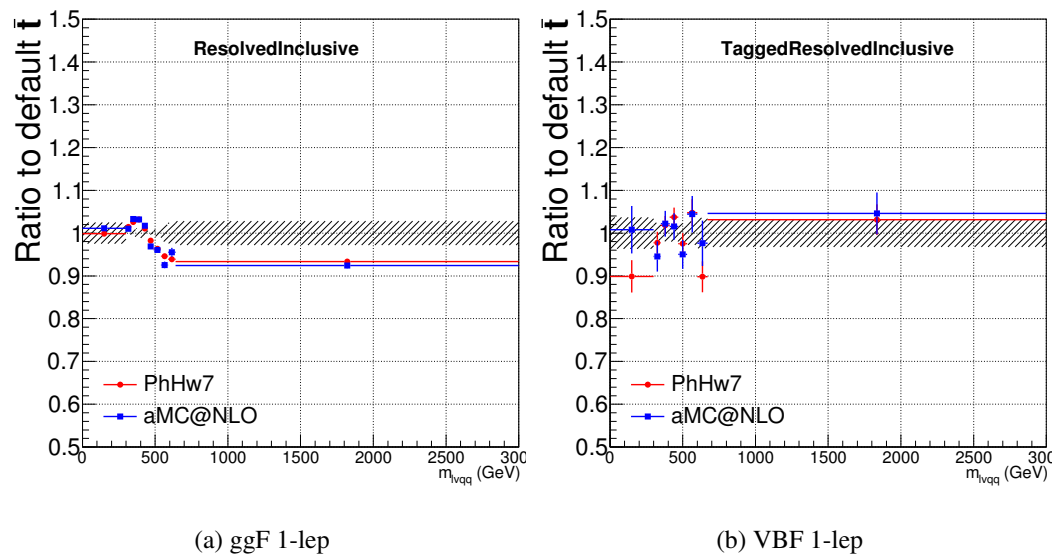


Figure 9.4: Ratio between the variations of generator (red) and hadronization (blue) variations for the Resolved regime for $t\bar{t}$ sample.

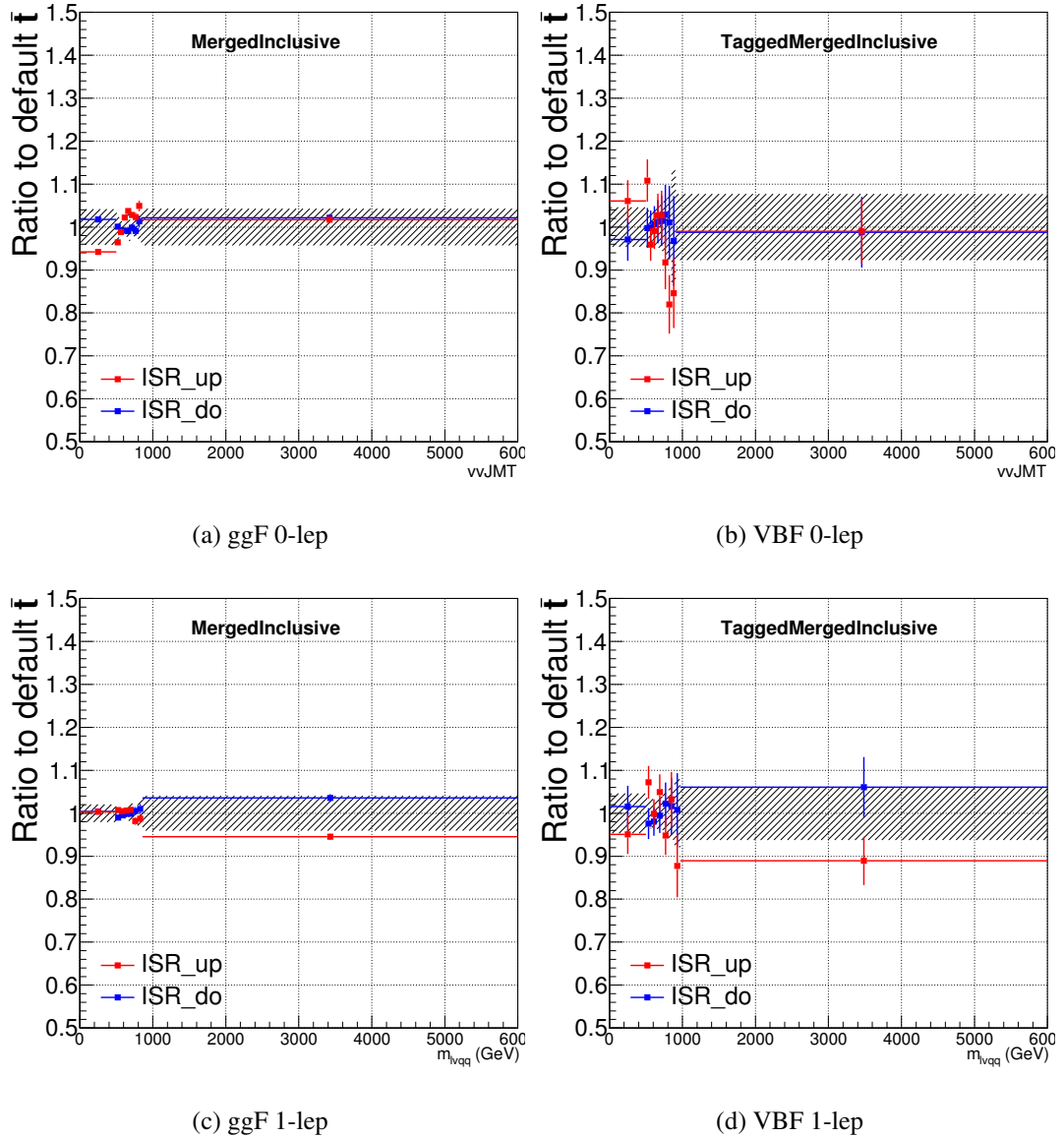


Figure 9.5: Ratio between the variations of ISR up (red) and down (blue) variations for the Merged regime for $t\bar{t}$ sample.

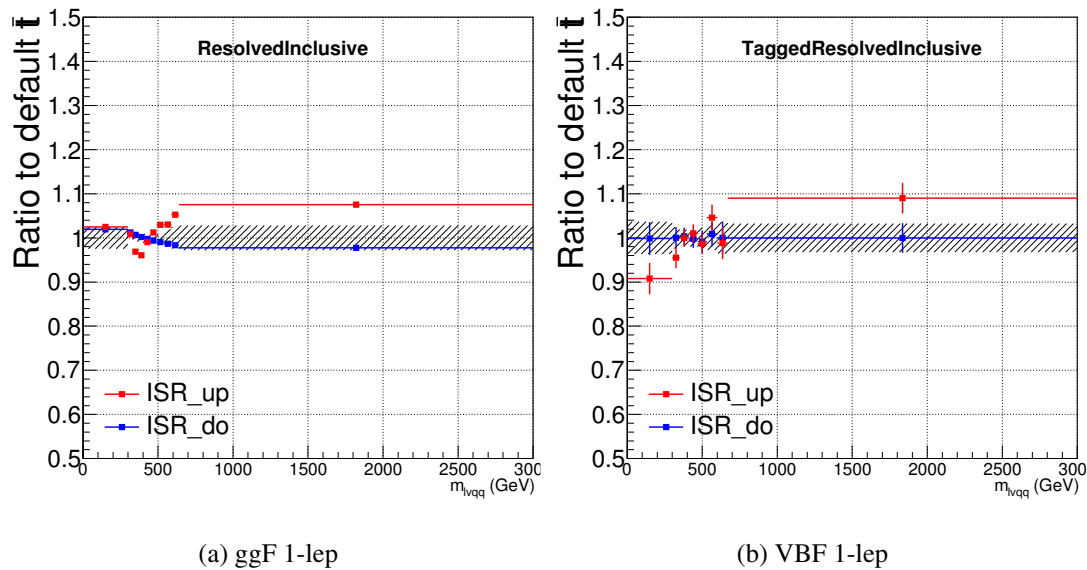


Figure 9.6: Ratio between the variations of ISR up (red) and down (blue) variations for the Resolved regime for $t\bar{t}$ sample.

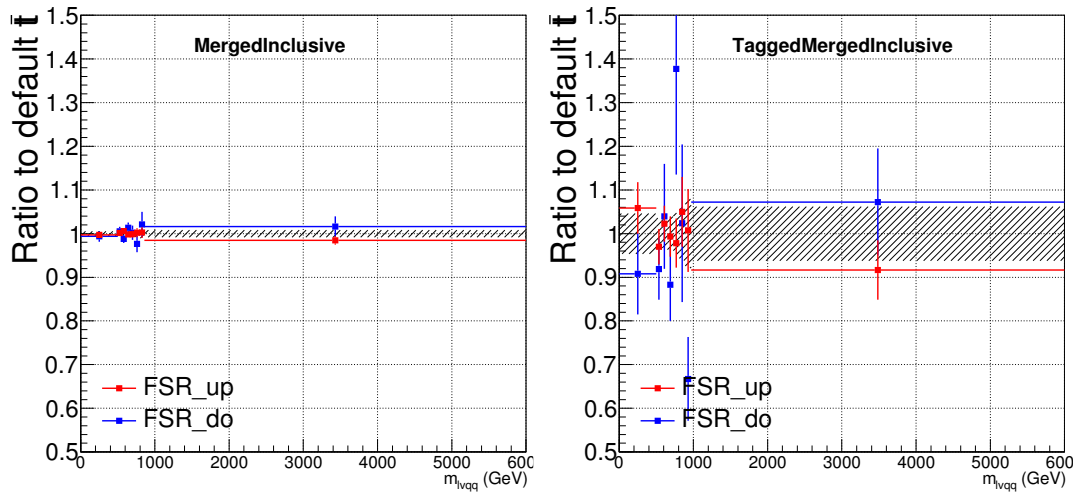


Figure 9.7: Ratio between the variations of FSR up (red) and down (blue) variations for the Merged regime for $t\bar{t}$ sample.

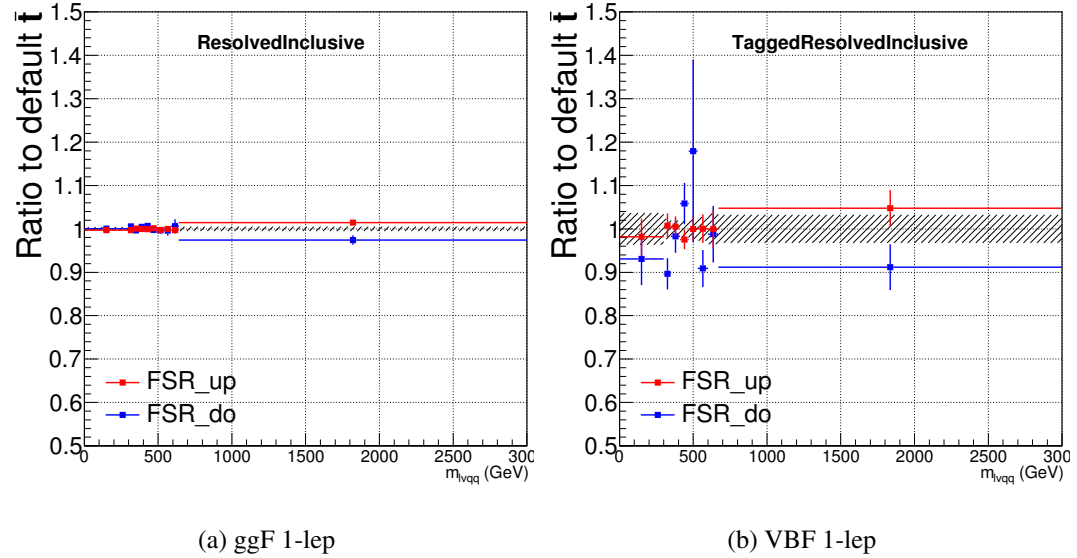


Figure 9.8: Ratio between the variations of FSR up (red) and down (blue) variations for the Resolved regime for $t\bar{t}$ sample.

₁₁₀₅ **Chapter 10**

₁₁₀₆ **Statistical Analysis**

₁₁₀₇ To determine the compatibility of the data collected with the proposed reso-
₁₁₀₈ nances a statistical procedure based on a likelihood function is used. A discovery
₁₁₀₉ test is used to measure the compatibility of the observed data with the back-
₁₁₁₀ ground only hypothesis. If the observed data is sufficiently incompatible with the
₁₁₁₁ background only hypothesis, this could indicate a discovery. In the absence of
₁₁₁₂ discovery, upper limits on the signal strength parameter, μ , are assessed using the
₁₁₁₃ CLs method.

₁₁₁₄ **10.1 Likelihood Function Definition**

₁₁₁₅ The likelihood function is product of Poisson probabilities for all analysis bins
₁₁₁₆ and systematic constraints:

$$\mathcal{L}(\mu, \boldsymbol{\theta}) = \prod_c \prod_i \frac{(\mu s_{ci}(\boldsymbol{\theta}) + b_{ci}(\boldsymbol{\theta}))^{n_{ci}}}{n_{ci}!} e^{-(\mu s_{ci}(\boldsymbol{\theta}) + b_{ci}(\boldsymbol{\theta}))} \prod_k (\theta'_k | \theta_k) \quad (10.1)$$

₁₁₁₇ Here c are the analysis channels considered and i runs over all the $m_{\ell\nu qq}$ bins

used in the fit. The signal strength parameter, μ , multiplies the expected signal yield in each analysis bin, s_{ci} . The background content for channel c and bin i is given by b_{ci} . The dependence of signal and background predictions on systematic uncertainties is described by the aforementioned set of nuisance parameters $\boldsymbol{\theta}$, which are parameterized by Gaussian or log-normal priors denoted here as θ_k . Statistical uncertainties of the simulated bin contents are also included as systematic uncertainties. Most systematics are correlated among all the analysis regions and considered to be independent from each other. The validity of this assumption is checked by evaluating the covariance of nuisance parameters.

10.2 Fit Configuration

The binning of $m_{\ell\nu qq}$ in signal regions for likelihood fit is determined by the statistical uncertainty of signal mass width. For each signal mass point, the signal mass resolution is given by the fitted Gaussian width of the $m_{\ell\nu qq}$. The fitted signal widths are then fit to a line to give a parameterized signal mass width, as shown in Figures 10.1 and 10.2. Bin widths are set first to this parameterized signal mass resolution. Then if the statistical uncertainty of the data or simulated background is more than 50%, bins are merged until the statistical uncertainty is less than 50%. All control regions contain only a single bin.

For this analysis, each signal model is fit in the Merged and Resolved channels for the relevant signal production mode simultaneously. The $W + \text{jets}$ and $t\bar{t}$ normalizations are given by the best fit values in the overall fit and these fitted normalizations are then applied to those backgrounds in the SRs.

Systematics may be affected by low statistics, leading to unsmooth m_{VV} distributions with unphysically large fluctuations. This can lead to artificial pulls and constraints in the fit. To remove such issues a multi-step smoothing pro-

1143 cedure is applied to all systematic variation distributions in all regions. First,
1144 distributions are rebinned until the statistical error per bin is at least 5%. Next
1145 all local extrema are identified. The bins around smallest extrema are iteratively
1146 merged until only four local extrema remain. Then distributions are rebinned so
1147 that statistical uncertainties in each bin are $< 5\%$.

1148 For some systematics, up and down variations may be in the same direction
1149 with respect to the nominal distributions. This causes the variations to not cover
1150 the nominal choice, and the interpretation of the confidence interval is skewed as
1151 the nominal distribution should be bracketed by the up and down variations. This
1152 asymmetry may also lead to unconstrained systematics in the fit. To handle such
1153 asymmetric systematics, if the up and down variation for a given systematic are in
1154 the same direction for at least three m_{VV} bins the variation is averaged for those
1155 bins. The averaging procedure replaces bin-by-bin the up and down variation bins
1156 by $b_{\pm}^{new} = b_{nom} \pm \frac{|b_+ - b_-|}{2}$, where b_{nom} is the nominal bin content and b_{\pm} are the
1157 original up and down variation bin content. The same procedure is also applied to
1158 any variations where the integral of the difference between the up/down variation
1159 and the nominal distribution is twice that of the other down/up variation, further
1160 ensuring variations are symmetric around the nominal distribution.

1161 Finally, systematics that have a negligible effect on the m_{VV} distribution are
1162 not considered in the fit. Shape systematics where no bin in the variational dis-
1163 tribution deviates more than 1% from the nominal distribution (after normalizing
1164 all histograms to the nominal) are not included in the fit. Also, statistical bin
1165 uncertainties $< 1\%$ are ignored.

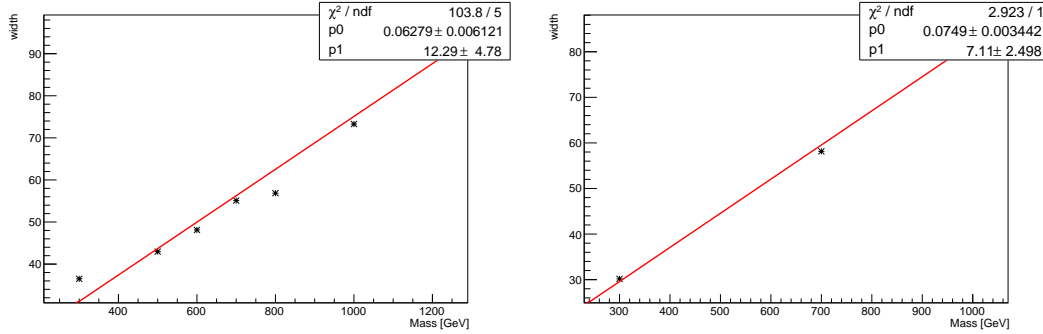


Figure 10.1: The HVT signal mass resolution as a function of mass fit with a straight line in the Resolved ggF region (left) and VBF (right) region.

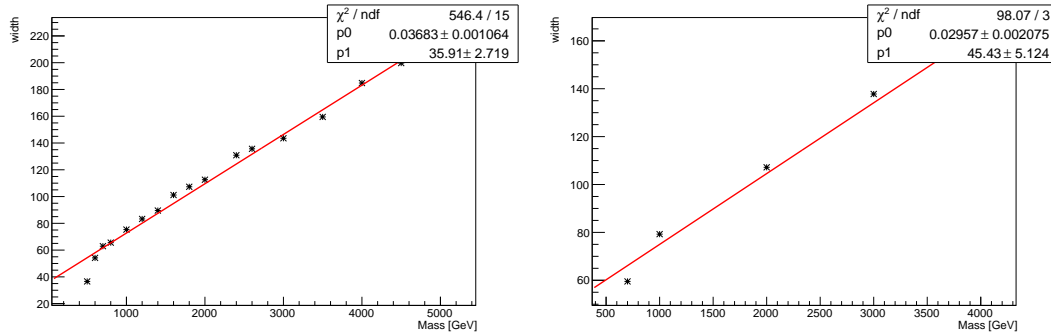


Figure 10.2: The HVT signal mass resolution as a function of mass fit with a straight line in the Merged ggF region (left) and VBF (right) region.

1166 10.3 Best Fit μ

1167 The best fit signal strength parameter is denoted by $\hat{\mu}$ and calculated by
 1168 maximizing the likelihood function with respect to all systematics and μ . The
 1169 corresponding set of systematics that maximize the likelihood are given by $\hat{\mu}$.
 1170 The first term in the likelihood is maximized when the expected number of signal
 1171 and background events is equal to the number of events in data ($n_{ci} = \mu s_{ci} +$
 1172 b_{ci}). Thus, by maximizing the likelihood, the fit determines values of μ and θ
 1173 that give the best agreement between expected and measured event yields. The

1174 second term in the likelihood is a penalty term which decreases the likelihood
1175 when systematics are shifted from their nominal values. This prevents the fit
1176 from profiling systematics in unphysical ways to maximize the likelihood. The
1177 uncertainty on μ is calculated by varying μ up and down until the natural log of
1178 the likelihood function shifts by one-half.

1179 10.4 Discovery Test

1180 To determine if the observed dataset is consistent with tested signal model a
1181 likelihood ratio is constructed:

$$\lambda(\mu) = \frac{\mathcal{L}(\mu, \hat{\theta}_\mu)}{\mathcal{L}(\hat{\mu}, \hat{\theta})} \quad (10.2)$$

1182 The denominator in this equation is the maximized value of \mathcal{L} over all system-
1183 atics and μ . The numerator is the maximized likelihood over all systematics for
1184 a given μ value, where the maximized systematics are given by $\hat{\mu}_\mu$. To test for
1185 the existence of signal the observed dataset the null hypothesis (H_0) is defined as
1186 the background only hypothesis and the alternate hypothesis includes signal and
1187 background (H_1). This test quantifies the compatibility of observed data with
1188 H_0 by calculating a p-value representing the probability of observing data as dis-
1189 crepant or more than the observed data under the H_0 . The test statistic used to
1190 calculate this p-value is given by (r_0):

$$r_0 = \begin{cases} -2 \ln \lambda(0), \hat{\mu} > 0 \\ +2 \ln \lambda(0), \hat{\mu} < 0 \end{cases} \quad (10.3)$$

1191 The expected distribution of the the test statistic under H_0 ($f(r_0|0)$) is used to
1192 calculate the p-value:

$$p_0 = \int_{r_0, obs}^{\infty} f(r_0 | 0) dr_0 \quad (10.4)$$

1193 Small p-values indicate the observed data is poorly described by H_0 . This
 1194 equivalent Z-score of a given p-value is usually used to further quantify the agree-
 1195 ment between the observed data and H_0 . The Z-score is given by the number of
 1196 standard deviations away from the mean of a Gaussian distribution, the integral
 1197 of the upper tail of the distribution would equal the p-value. Mathematically:

$$Z = \Phi^{-1}(1 - p_0) \quad (10.5)$$

1198 where Φ is the Gaussian cumulative distribution function. The statistical
 1199 significance of these tests are expressed as the Z -score. In particle physics, 3σ is
 1200 considered evidence for new phenomena and 5σ is the threshold for discovery.

1201 10.5 Exclusion Limits

1202 In the absence of discovery, upper limits on the signal strength, μ are set using
 1203 the CLs method [cite P60]. The test statistic for this test, q_μ , is constructed as:

$$\tilde{\lambda}_\mu = \begin{cases} \frac{\mathcal{L}(\mu, \hat{\theta}_\mu)}{\mathcal{L}(\hat{\mu}, \hat{\theta})}, \hat{\mu} > 0 \\ \frac{\mathcal{L}(\mu, \hat{\theta}_\mu)}{\mathcal{L}(0, \hat{\theta}_0)}, \hat{\mu} < 0 \end{cases} \quad (10.6)$$

$$\tilde{q}_\mu = \begin{cases} -2 \ln \tilde{\lambda}(\mu), \hat{\mu} < \mu \\ +2 \ln \tilde{\lambda}(\mu), \hat{\mu} > \mu \end{cases} \quad (10.7)$$

1204 As defined, larger values of q_μ correspond to increasing incompatibility between
 1205 the observed data and the background + signal hypothesis. The observed value
 1206 of the test statistic, $q_{\mu, obs}$, is then compared to its expected distribution, f , to

1207 calculate p-values to assess the likelihood of the background+signal hypothesis.

1208 Using these distributions, CL_s values are computed as:

$$1209 \quad CL_{s+b} = \int_{q_{\mu,obs}}^{\infty} f(q_{\mu}|\mu) dq_{\mu} \quad (10.8)$$

$$1210 \quad CL_b = \int_{q_0^{obs}}^{\infty} f(q_{\mu}|\mu = 0) dq_{\mu} \quad (10.9)$$

$$1211 \quad CL_s = \frac{CL_{s+b}}{CL_b} \quad (10.10)$$

1212 CL_{s+b} is the p-value for the signal + background hypothesis and CL_b is the
1213 p-value for the background only hypothesis. The CL_s value is interpreted as
1214 the probability to observe the background + signal hypothesis normalized to the
1215 probability of background-only hypothesis. Normalizing by CL_b prevents setting
artificially strong exclusion limits due to downward fluctuations in data.

1216 For a given signal hypothesis, μ values are scanned simultaneously over all
1217 m_{WV} bins to find the μ value that yields $CL_s=0.05$, meaning the likelihood of
1218 finding data more incompatible with the signal+background hypothesis (relative
1219 to the background only hypothesis) is 5%. The 95% upper limit on the cross
1220 section is then calculated as the product of the μ value found, branching ratio,
1221 and theory cross section.

Part IV

1222

Results

1223

1224 **Chapter 11**

1225 **Statistical Interpretation**

1226 **11.1 Discovery Tests**

1227 To test for the existence of signal in the observed dataset, the discovery tests
1228 discussed earlier are used to calculate p-values as a function of resonance mass.
1229 The results of these tests are shown in Figures 11.1 - 11.5. Across the different
1230 DY signals the largest excesses are $\sim 2.2\sigma$ at 600 GeV and 1.8σ at 2 TeV. The
1231 largest excesses for VBF signals are $< 2.5\sigma$ at for 1 TeV resonances. As these
1232 deviations do not constitute discoveries, upper limits on μ are calculated.

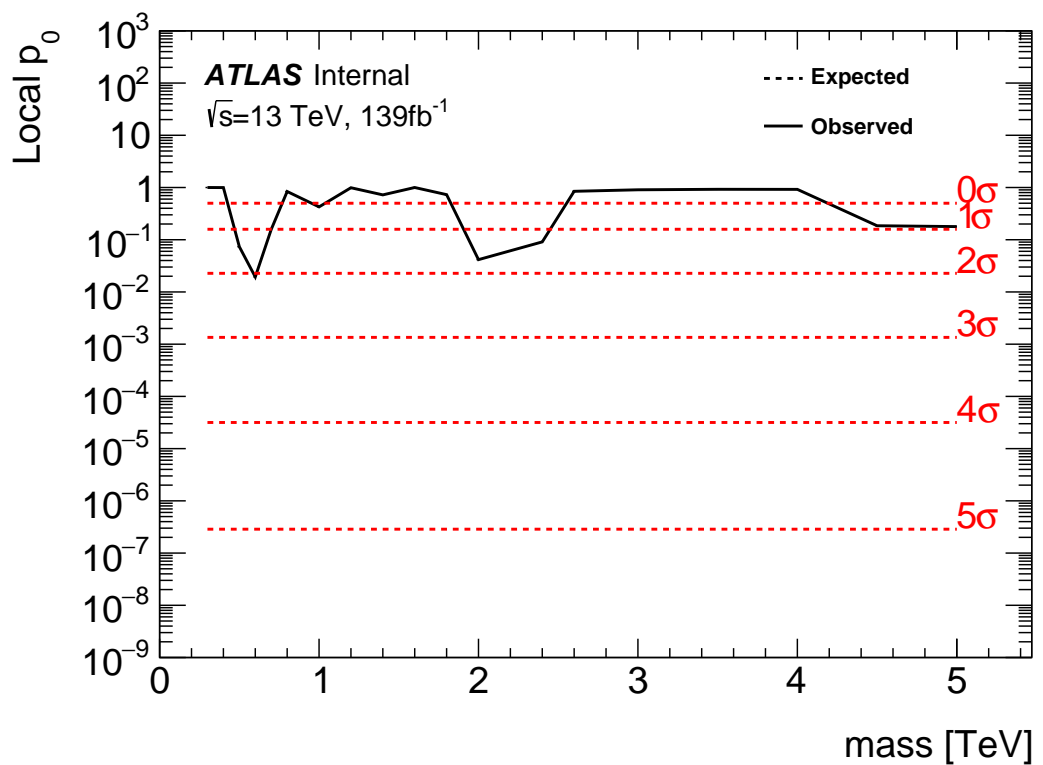


Figure 11.1: These plots show the measured p_0 value as a function of resonance mass for HVT Z' DY production.

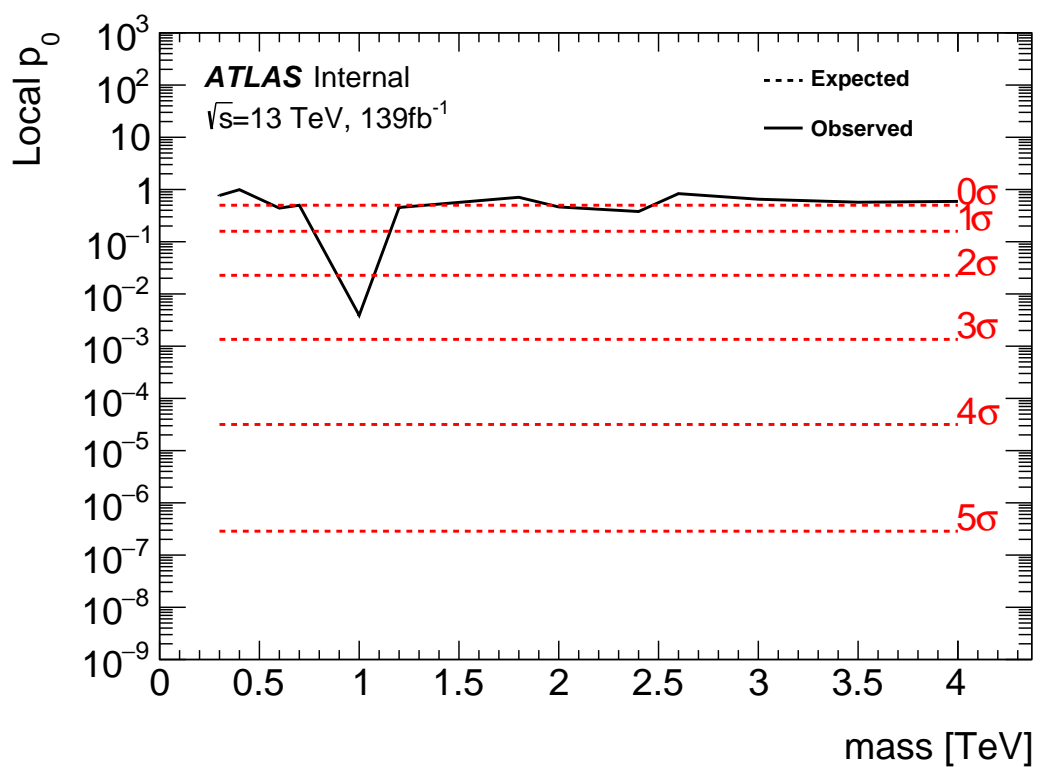


Figure 11.2: These plots show the measured p_0 value as a function of resonance mass for HVT Z' VBF production.

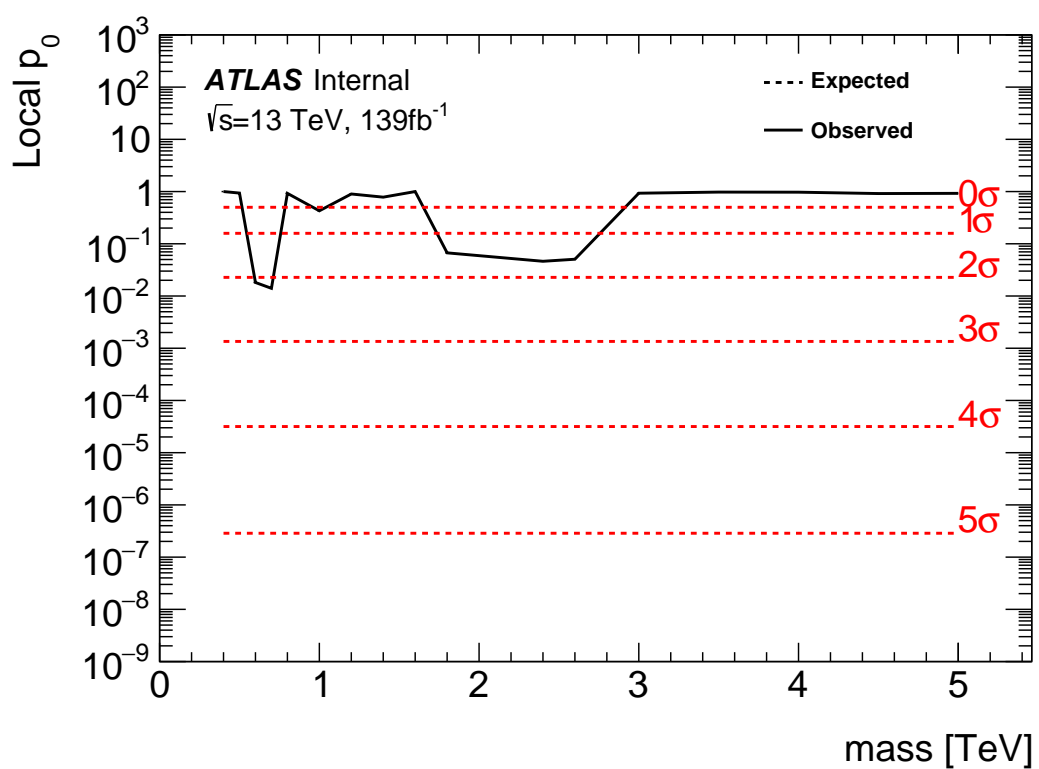


Figure 11.3: These plots show the measured p_0 value as a function of resonance mass for HVT W' DY production.

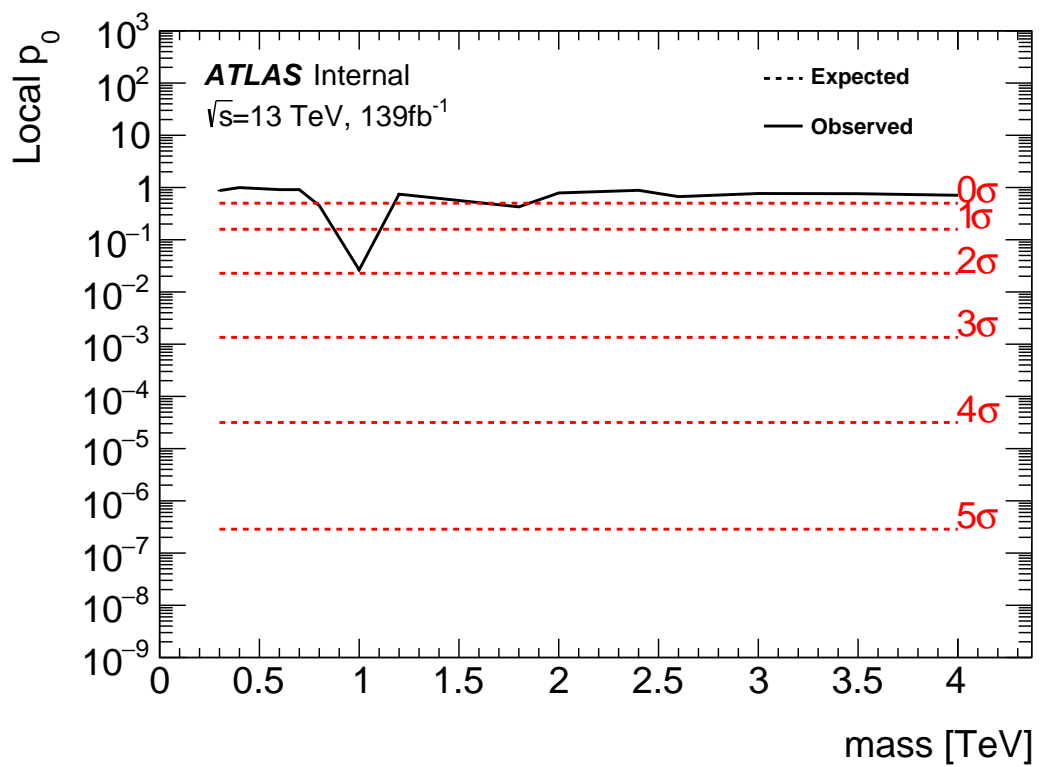


Figure 11.4: These plots show the measured p_0 value as a function of resonance mass for HVT W' VBF production.

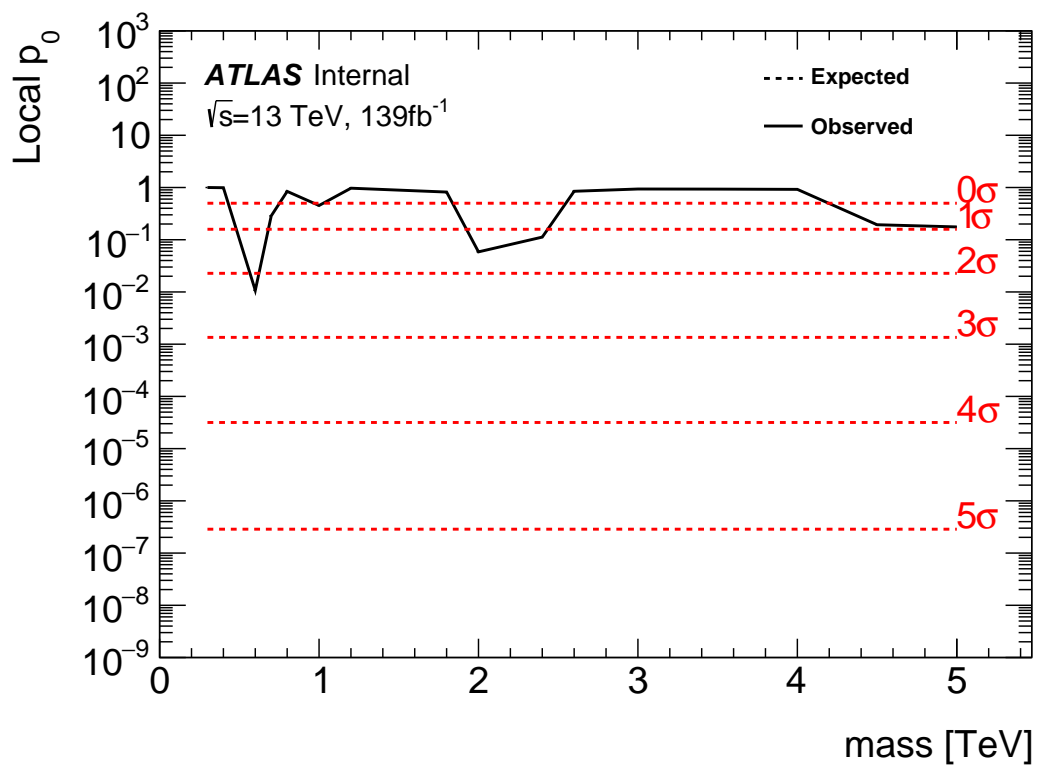


Figure 11.5: These plots show the measured p_0 value as a function of resonance mass for the RS Graviton DY production.

1233 11.2 Systematic Profiling and Correlations

1234 The ranked systematics and their fitted values are shown for the different anal-
 1235 ysis regions in Figure 11.6 - 11.8. Note that background normalizations for $W+jets$
 1236 and $t\bar{t}$ are left free to float in the fit. This means the nominal normalization val-
 1237 ues are at one and the uncertainties are not plotted in the ranked plots. Overall,
 1238 systematics are not pulled outside their uncertainties, especially for highly ranked
 1239 nuisance parameters.

1240 The correlation between systematics are shown in Figures ???. Correlations
 1241 between background normalization are expected. The remaining systematic cor-
 relations are not very strong or unexpected.

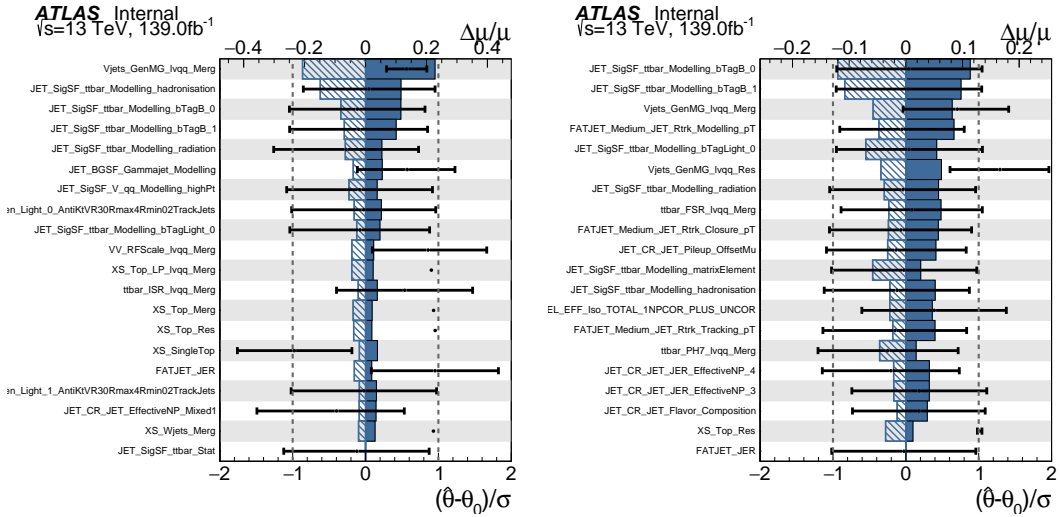


Figure 11.6: Ranked systematics and their fitted values for WW DY (right) and VBF (left) selections.

1242

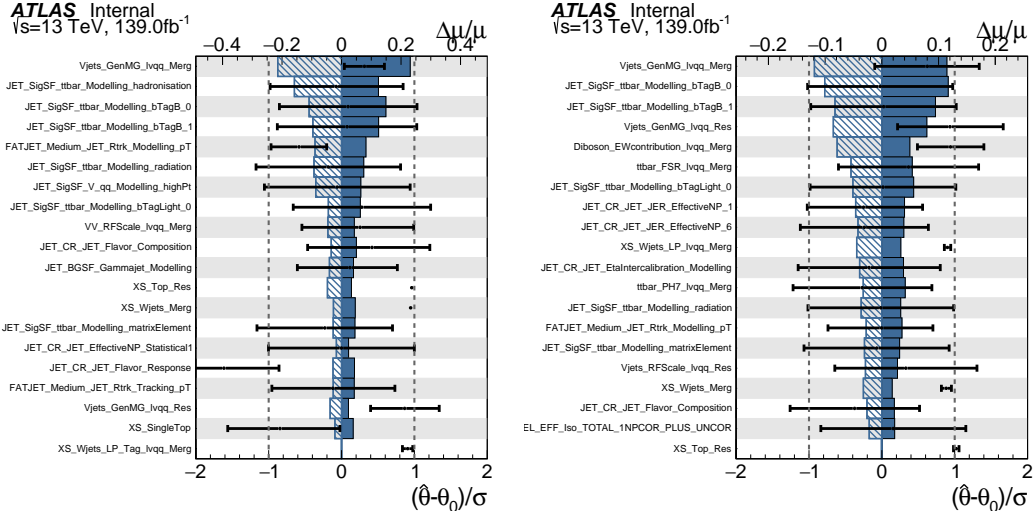


Figure 11.7: Ranked systematics and their fitted values for WZ DY (right) and VBF (left) selections.

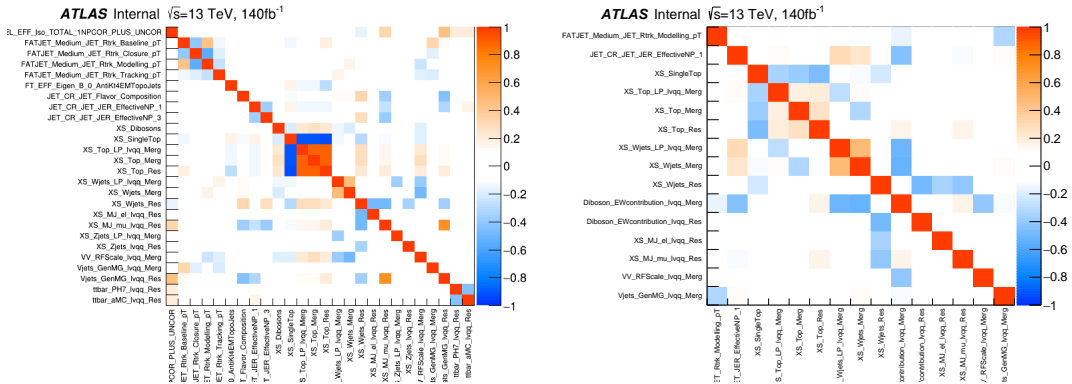


Figure 11.8: Correlations between systematics for WW DY (right) and VBF (left) selections.

1243 11.3 Expected and Measured Yields

1244 The yield tables for the four analysis regions are shown in Tables ?? - ?? . The
 1245 fitted background normalizations are shown in Tables ??-?? . The control region
 1246 $m_{\ell\nu qq}$ distributions are shown in Figures 11.9 - 11.12. The signal region $m_{\ell\nu qq}$
 1247 distributions are shown in Figures 11.13 - ?? .

	HP WCR	LP WCR	Resolved WCR
Electron Multi-jet	-	-	16507.83 ± 2314.87
Muon Multi-jet	-	-	19977.12 ± 2816.06
Diboson	1833.41 ± 177.78	3323.93 ± 320.92	9147.67 ± 961.63
Single-top	2160.62 ± 402.34	3551.09 ± 660.00	20058.36 ± 3817.26
$t\bar{t}$	15518.86 ± 338.22	24069.54 ± 453.15	138866.23 ± 1989.71
$W+jets$	40141.57 ± 357.79	88113.06 ± 487.87	673200.38 ± 4120.53
$Z+jets$	778.83 ± 78.93	1765.54 ± 179.10	16570.50 ± 1672.71
Total	60433.29 ± 664.92	120823.16 ± 1006.99	894328.12 ± 7247.12
Data	60264.00	120852.00	895362.00
	HP TCR	LP TCR	Resolved TCR
Electron Multi-jet	-	-	-
Muon Multi-jet	-	-	-
Diboson	421.11 ± 37.98	550.44 ± 53.10	996.87 ± 119.63
Single-top	4691.44 ± 846.11	3466.26 ± 631.03	16848.71 ± 3258.26
$t\bar{t}$	38945.18 ± 848.77	33836.95 ± 637.04	224226.14 ± 3212.76
$W+jets$	2258.34 ± 20.13	6564.78 ± 36.35	23466.41 ± 143.63
$Z+jets$	66.35 ± 6.72	213.26 ± 21.63	846.66 ± 85.47
Total	46382.43 ± 1199.25	44631.70 ± 899.23	266384.78 ± 4580.43
Data	46354.00	44629.00	266443.00
	WW SR	LP SR	Resolved 1-lepton SR
Electron Multi-jet	-	-	10788.40 ± 1512.85
Muon Multi-jet	-	-	15759.50 ± 2221.53
Diboson	4990.30 ± 376.50	3901.07 ± 313.22	16971.29 ± 1523.77
Single-top	3117.71 ± 565.07	2176.46 ± 400.52	20422.85 ± 3731.94
$t\bar{t}$	13785.77 ± 302.14	11005.12 ± 207.41	126965.25 ± 1819.66
$W+jets$	24718.56 ± 223.72	60080.66 ± 333.12	444133.56 ± 2719.02
$Z+jets$	478.18 ± 48.46	1226.69 ± 124.44	11686.32 ± 1179.69
Total	47090.52 ± 777.65	78389.98 ± 654.22	646727.19 ± 5963.98
Data	47330.00	78380.00	645610.00

Table 11.1: Expected and Measured for DY WW $W+jets$, $t\bar{t}$ control regions and signal regions.

	HP Untagged WCR	LP Untagged WCR	Resolved Untagged WCR
Electron Multi-jet	-	-	15080.03 ± 2277.99
Muon Multi-jet	-	-	27347.10 ± 2950.07
Diboson	1508.48 ± 154.20	2758.24 ± 284.50	9038.55 ± 728.69
Single-top	1756.59 ± 306.69	2913.18 ± 515.93	20511.74 ± 3523.47
$t\bar{t}$	13134.00 ± 238.30	21815.37 ± 334.98	140157.77 ± 2636.96
$W+jets$	40654.84 ± 333.65	87657.76 ± 501.96	665909.12 ± 4420.62
$Z+jets$	768.72 ± 77.97	1759.87 ± 178.96	16512.46 ± 1673.23
Total	57822.63 ± 540.40	116904.42 ± 862.16	894556.75 ± 7492.20
Data	57699.00	117306.00	895362.00
	HP Tagged WCR	LP Tagged WCR	Resolved Tagged WCR
Electron Multi-jet	-	-	384.58 ± 57.11
Muon Multi-jet	-	-	602.93 ± 190.12
Diboson	30.22 ± 4.69	48.95 ± 7.16	264.64 ± 28.24
Single-top	308.44 ± 56.19	371.59 ± 69.43	5752.39 ± 1029.97
$t\bar{t}$	1683.82 ± 48.73	2041.48 ± 70.00	58431.49 ± 614.30
$W+jets$	583.55 ± 75.37	1109.45 ± 85.78	11891.68 ± 903.01
$Z+jets$	13.19 ± 1.34	23.06 ± 2.34	324.74 ± 32.85
Total	2619.22 ± 106.00	3594.53 ± 130.90	77652.45 ± 1514.89
Data	2565.00	3546.00	77973.00
	HP Untagged TCR	LP Untagged TCR	Resolved Untagged TCR
Electron Multi-jet	-	-	-
Muon Multi-jet	-	-	-
Diboson	289.45 ± 28.45	346.78 ± 35.85	650.85 ± 65.56
Single-top	3107.99 ± 538.03	2250.64 ± 385.41	9606.87 ± 1698.22
$t\bar{t}$	30992.40 ± 562.33	26954.21 ± 413.89	91893.59 ± 1728.91
$W+jets$	2236.29 ± 18.35	4874.03 ± 27.91	16122.97 ± 107.03
$Z+jets$	71.54 ± 7.26	155.50 ± 15.81	577.71 ± 58.54
Total	36697.66 ± 779.03	34581.16 ± 567.59	118851.98 ± 2427.40
Data	36677.00	34573.00	118928.00
	HP Tagged TCR	LP Tagged TCR	Resolved Tagged TCR
Electron Multi-jet	-	-	-
Muon Multi-jet	-	-	-
Diboson	9.72 ± 1.13	8.75 ± 1.16	34.06 ± 4.98
Single-top	105.87 ± 20.65	119.66 ± 22.68	656.89 ± 132.96
$t\bar{t}$	1904.75 ± 50.61	1483.86 ± 47.05	17965.33 ± 188.87
$W+jets$	32.36 ± 4.28	85.74 ± 6.96	489.01 ± 37.13
$Z+jets$	1.27 ± 0.13	1.93 ± 0.20	19.14 ± 1.94
Total	2053.98 ± 54.84	1699.93 ± 52.70	19164.43 ± 234.01
Data	2047.00	1708.00	19143.00

Table 11.2: Expected and Measured for DY WZ $W+jets$, $t\bar{t}$ tag and untag control regions.

	HP Untagged SR	LP Untagged SR	Resolved Untagged SR
Electron Multi-jet	-	-	7782.17 ± 1175.56
Muon Multi-jet	-	-	17004.81 ± 1834.40
Diboson	3041.17 ± 273.77	2266.35 ± 212.79	14724.12 ± 1224.31
Single-top	2123.28 ± 373.83	1379.35 ± 240.92	18336.88 ± 3082.47
$t\bar{t}$	11678.86 ± 213.63	8906.34 ± 136.88	112669.24 ± 2122.46
$W+jets$	22741.32 ± 191.47	41726.76 ± 240.56	342934.00 ± 2280.21
$Z+jets$	442.03 ± 44.84	849.79 ± 86.42	9271.83 ± 939.52
Total	40026.65 ± 546.81	55128.59 ± 432.90	522723.03 ± 5131.71
Data	40193.00	54735.00	521813.00
	HP Tagged SR	LP Tagged SR	Resolved Tagged SR
Electron Multi-jet	-	-	199.22 ± 29.58
Muon Multi-jet	-	-	393.43 ± 124.06
Diboson	102.58 ± 11.59	65.44 ± 8.05	624.07 ± 58.10
Single-top	178.21 ± 33.62	155.53 ± 28.95	3470.39 ± 617.48
$t\bar{t}$	1017.93 ± 31.95	706.76 ± 26.20	38189.30 ± 401.91
$W+jets$	325.58 ± 41.62	575.36 ± 43.29	6161.96 ± 467.71
$Z+jets$	7.81 ± 0.80	11.62 ± 1.19	183.36 ± 18.55
Total	1632.11 ± 63.39	1514.70 ± 58.86	49221.74 ± 884.06
Data	1699.00	1559.00	48919.00

Table 11.3: Expected and Measured for DY WZ $W+jets$, $t\bar{t}$ tag and untag signal regions.

	HP WCR	LP WCR	Resolved WCR
Electron Multi-jet	-	-	898.48 ± 137.82
Muon Multi-jet	-	-	601.46 ± 182.74
Diboson	107.45 ± 45.20	166.87 ± 68.11	292.10 ± 235.29
Single-top	78.19 ± 18.22	132.71 ± 31.93	879.82 ± 216.89
$t\bar{t}$	400.71 ± 28.35	569.70 ± 48.88	5067.51 ± 155.69
$W+jets$	864.49 ± 63.44	1940.80 ± 89.41	18563.70 ± 408.99
$Z+jets$	19.51 ± 2.00	46.63 ± 4.77	795.20 ± 80.89
Total	1470.35 ± 84.89	2856.71 ± 126.74	27098.28 ± 594.01
Data	1495.00	2898.00	27120.00
	HP TCR	LP TCR	Resolved TCR
Electron Multi-jet	-	-	-
Muon Multi-jet	-	-	-
Diboson	14.95 ± 6.61	27.57 ± 14.12	24.33 ± 20.32
Single-top	68.31 ± 16.17	58.93 ± 13.56	278.60 ± 73.04
$t\bar{t}$	496.60 ± 31.72	401.23 ± 32.13	3834.49 ± 104.60
$W+jets$	50.68 ± 4.19	144.02 ± 7.86	450.01 ± 11.87
$Z+jets$	1.32 ± 0.14	5.35 ± 0.55	29.96 ± 3.07
Total	631.87 ± 36.45	637.10 ± 38.44	4617.39 ± 129.77
Data	636.00	634.00	4615.00
	HP SR	LP SR	Resolved SR
Electron Multi-jet	-	-	596.34 ± 91.52
Muon Multi-jet	-	-	481.01 ± 144.48
Diboson	148.84 ± 48.64	181.42 ± 67.30	395.52 ± 318.06
Single-top	79.49 ± 19.80	56.82 ± 14.89	782.07 ± 190.79
$t\bar{t}$	338.42 ± 24.14	236.80 ± 20.88	4261.70 ± 138.98
$W+jets$	501.13 ± 39.36	1347.76 ± 64.50	11445.73 ± 291.49
$Z+jets$	9.25 ± 0.95	28.77 ± 2.95	567.66 ± 57.94
Total	1077.13 ± 69.93	1851.57 ± 96.73	18530.03 ± 523.88
Data	1096.00	1846.00	18530.00

Table 11.4: Expected and Measured for VBF WW $W+jets$, $t\bar{t}$ control regions and signal regions.

	HP WCR	LP WCR	Resolved WCR
Electron Multi-jet	-	-	870.00 ± 132.75
Muon Multi-jet	-	-	618.45 ± 196.90
Diboson	92.92 ± 41.77	145.90 ± 64.26	228.62 ± 114.62
Single-top	71.13 ± 16.29	118.82 ± 27.98	1209.87 ± 281.64
$t\bar{t}$	427.80 ± 29.72	509.19 ± 46.57	6860.87 ± 254.83
$W+jets$	871.68 ± 64.22	2020.67 ± 93.54	19088.50 ± 442.10
$Z+jets$	19.58 ± 2.01	47.39 ± 4.85	800.19 ± 82.02
Total	1483.11 ± 83.79	2841.97 ± 125.92	29676.50 ± 644.96
Data	1495.00	2898.00	29755.00
	HP TCR	LP TCR	Resolved TCR
Electron Multi-jet	-	-	-
Muon Multi-jet	-	-	-
Diboson	10.12 ± 4.51	12.73 ± 6.55	14.23 ± 7.49
Single-top	51.57 ± 12.31	35.07 ± 8.17	169.21 ± 44.54
$t\bar{t}$	470.06 ± 28.97	298.99 ± 25.28	2414.75 ± 75.42
$W+jets$	49.64 ± 4.17	109.69 ± 6.16	378.22 ± 12.05
$Z+jets$	1.28 ± 0.13	4.81 ± 0.50	17.62 ± 1.83
Total	582.67 ± 32.07	461.30 ± 28.05	2994.03 ± 88.75
Data	584.00	459.00	3001.00
	HP SR	LP SR	Resolved SR
Electron Multi-jet	-	-	444.65 ± 67.99
Muon Multi-jet	-	-	397.29 ± 125.59
Diboson	109.66 ± 44.13	112.28 ± 46.45	265.75 ± 139.43
Single-top	63.16 ± 15.20	48.02 ± 11.56	872.16 ± 205.00
$t\bar{t}$	348.95 ± 24.34	190.68 ± 17.75	5134.25 ± 193.57
$W+jets$	467.21 ± 37.12	973.73 ± 47.91	10226.83 ± 254.67
$Z+jets$	8.15 ± 0.84	23.62 ± 2.43	558.48 ± 57.25
Total	997.13 ± 64.42	1348.33 ± 70.06	17899.41 ± 432.98
Data	1018.00	1313.00	17826.00

Table 11.5: Expected and Measured for VBF WZ $W+jets$, $t\bar{t}$ control regions and signal regions.

Background	Fitted Normalization
XS_Top_LP_lvqq_Merg_binned	$0.905^{+0.0166}_{-0.0166}$
XS_Top_Merg	$0.936^{+0.0199}_{-0.0199}$
XS_Top_Res	$0.957^{+0.0134}_{-0.0134}$
XS_Wjets_LP_lvqq_Merg_binned	$0.884^{+0.00489}_{-0.00489}$
XS_Wjets_Merg	$0.931^{+0.00831}_{-0.00831}$
XS_Wjets_Res	$1.03^{+0.00628}_{-0.00628}$

Table 11.6: Fitted background normalizations for $t\bar{t}$ and $W+jets$ backgrounds for the DY WW analysis region.

Background	Fitted Normalization
XS_Top_LP_Tag_lvqq_Merg_binned	$0.973^{+0.0333}_{-0.0333}$
XS_Top_LP_lvqq_Merg_binned	$0.894^{+0.0135}_{-0.0135}$
XS_Top_Merg	$0.893^{+0.016}_{-0.016}$
XS_Top_Res	$0.965^{+0.0179}_{-0.0179}$
XS_Top_Tag_lvqq_Merg_binned	$0.954^{+0.0276}_{-0.0276}$
XS_Top_Tag_lvqq_Res_binned	$0.999^{+0.0105}_{-0.0105}$
XS_Wjets_LP_Tag_lvqq_Merg_binned	$0.912^{+0.0703}_{-0.0703}$
XS_Wjets_LP_lvqq_Merg_binned	$0.876^{+0.00502}_{-0.00502}$
XS_Wjets_Merg	$0.948^{+0.00779}_{-0.00779}$
XS_Wjets_Res	$1.01^{+0.00673}_{-0.00673}$
XS_Wjets_Tag_lvqq_Merg_binned	$0.906^{+0.117}_{-0.117}$
XS_Wjets_Tag_lvqq_Res_binned	$1.2^{+0.0904}_{-0.0904}$

Table 11.7: Fitted background normalizations for $t\bar{t}$ and $W+jets$ backgrounds for the DY WZ analysis region.

Background	Fitted Normalization
XS_Top_LP_lvqq_Merg_binned	$0.79^{+0.0673}_{-0.0673}$
XS_Top_Merg	$0.888^{+0.061}_{-0.061}$
XS_Top_Res	$1.01^{+0.0311}_{-0.0311}$
XS_Wjets_LP_lvqq_Merg_binned	$0.88^{+0.0423}_{-0.0423}$
XS_Wjets_Merg	$0.881^{+0.0677}_{-0.0677}$
XS_Wjets_Res	$0.932^{+0.0202}_{-0.0202}$

Table 11.8: Fitted background normalizations for $t\bar{t}$ and $W+jets$ backgrounds for the VBF WW analysis region.

Background	Fitted Normalization
XS_Top_LP_lvqq_Merg_binned	$0.708^{+0.064}_{-0.064}$
XS_Top_Merg	$0.958^{+0.0644}_{-0.0644}$
XS_Top_Res	$1.02^{+0.038}_{-0.038}$
XS_Wjets_LP_lvqq_Merg_binned	$0.9^{+0.0438}_{-0.0438}$
XS_Wjets_Merg	$0.883^{+0.0685}_{-0.0685}$
XS_Wjets_Res	$0.945^{+0.0219}_{-0.0219}$

Table 11.9: Fitted background normalizations for $t\bar{t}$ and $W+jets$ backgrounds for the VBF WZ analysis region.

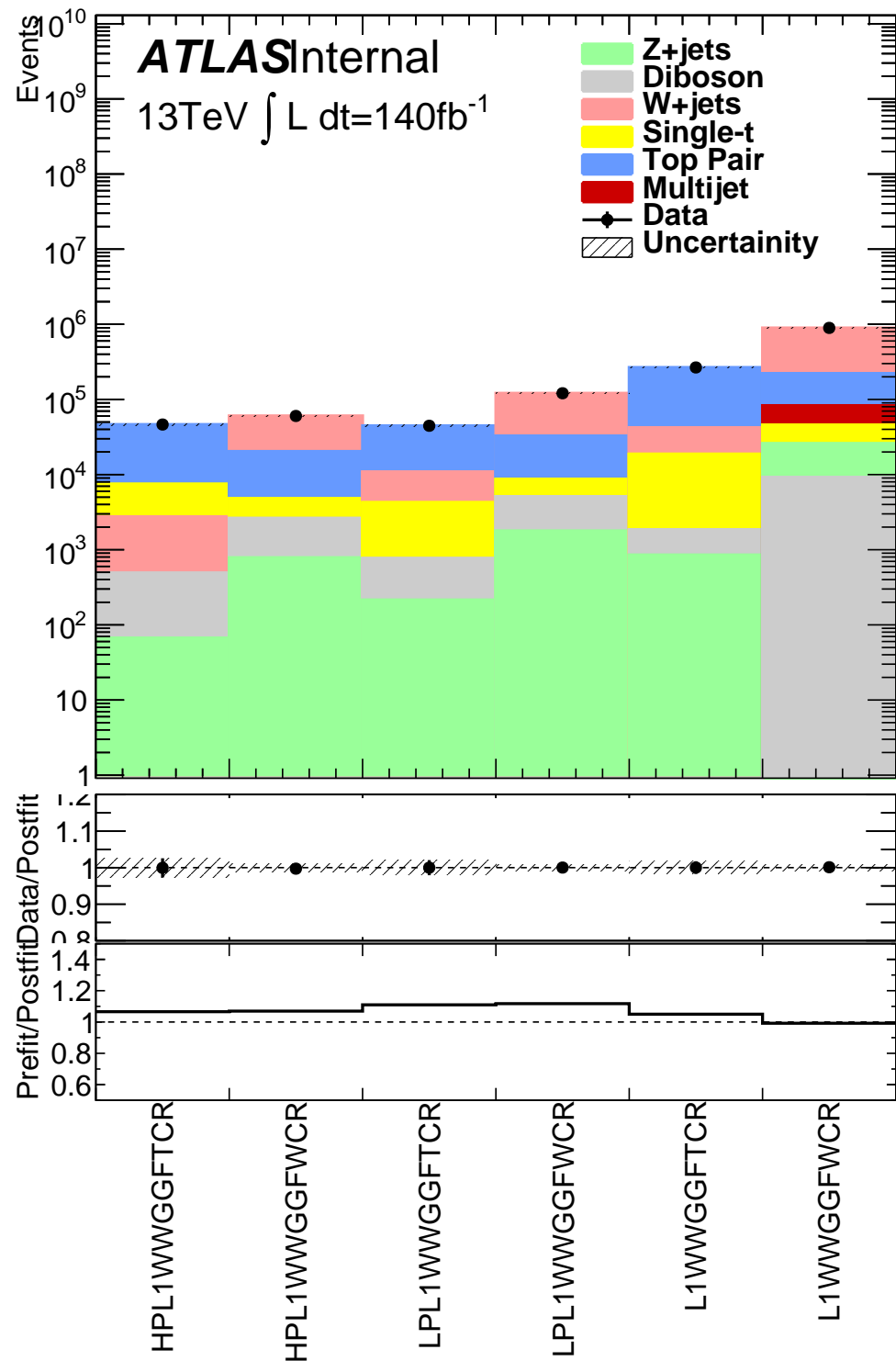


Figure 11.9: This figure shows the distribution of $m_{\ell\nu qq}$ in the DY WW control regions.

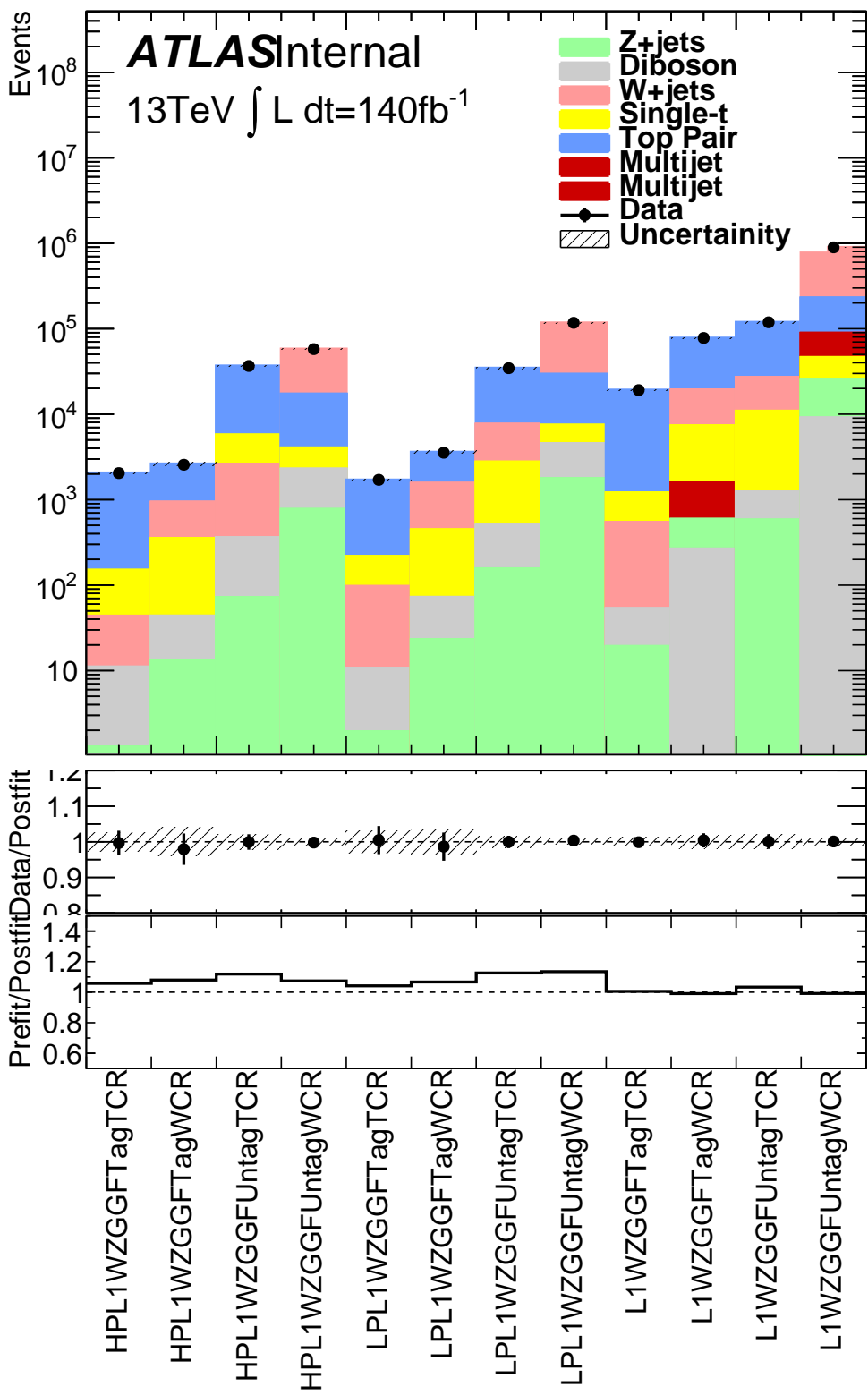


Figure 11.10: This figure shows the distribution of $m_{\ell\nu qq}$ in the DY WZ control regions.

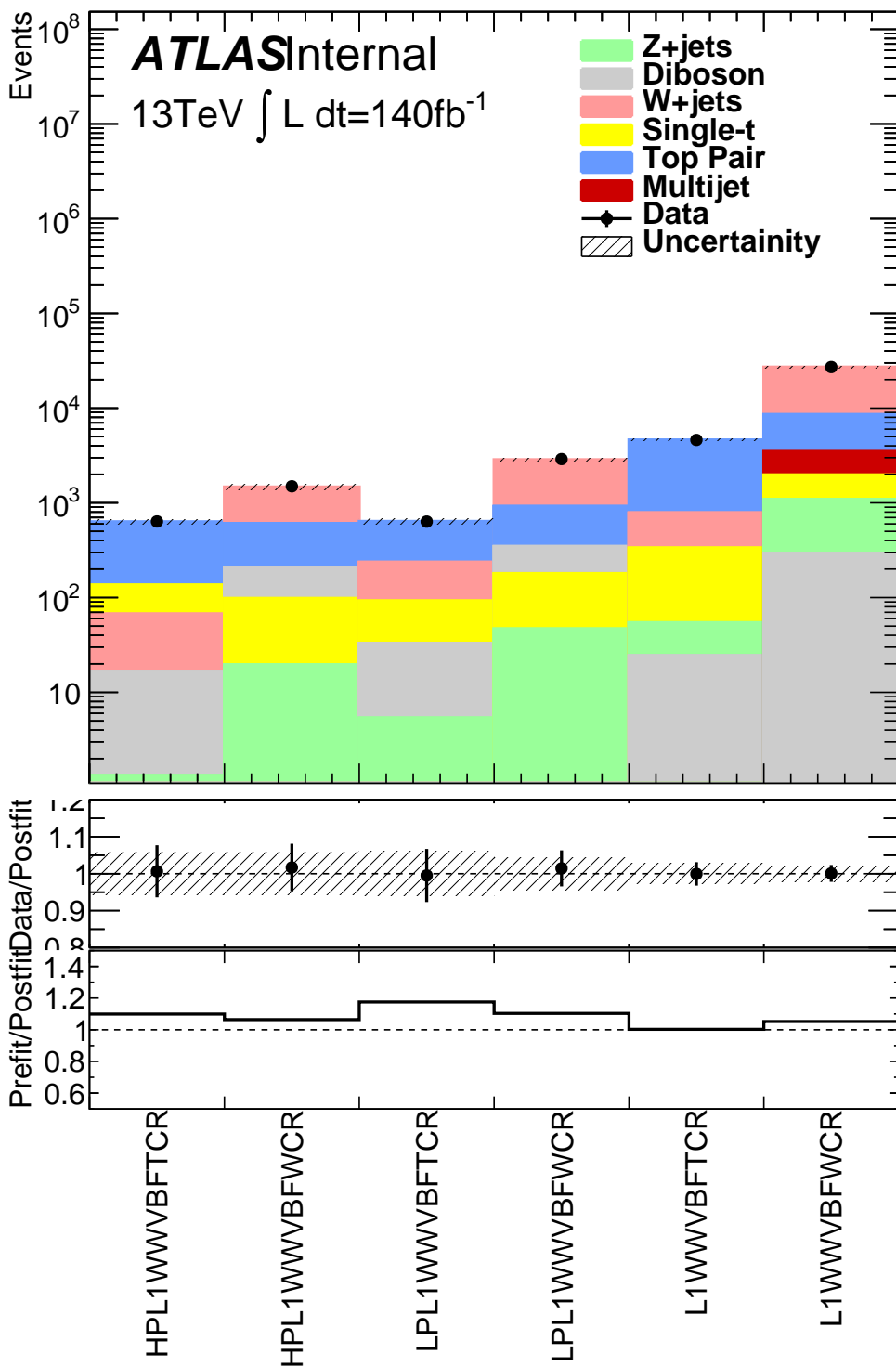


Figure 11.11: This figure shows the distribution of $m_{\ell\nu qq}$ in the VBF WW control regions.

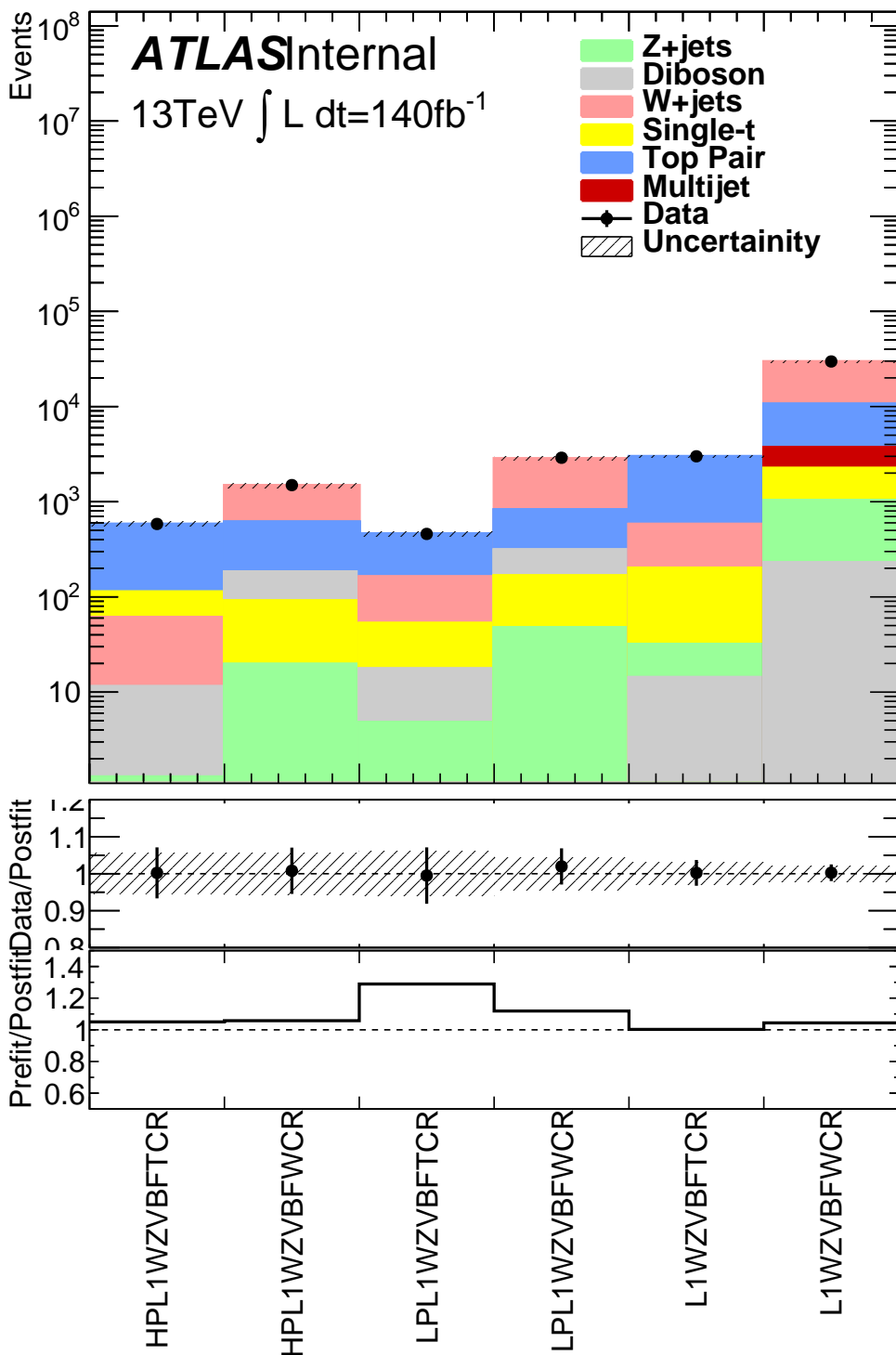


Figure 11.12: This figure shows the distribution of $m_{\ell\nu qq}$ in the VBF WZ control regions.

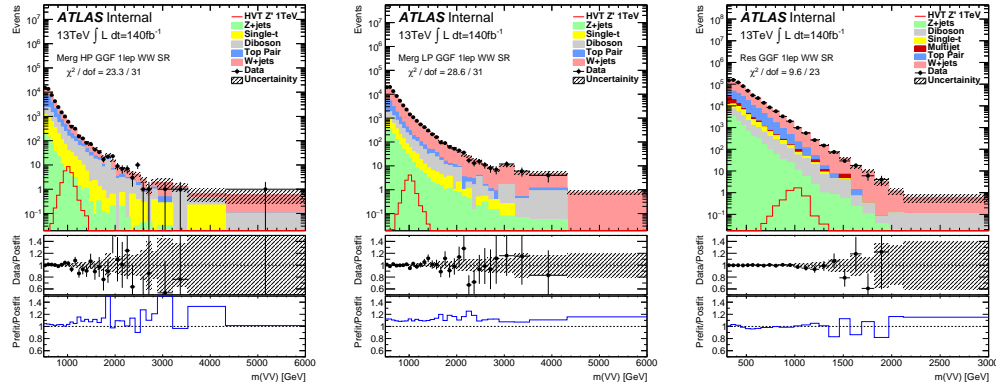


Figure 11.13: This figure shows the distribution of $m_{\ell\nu qq}$ in the GGF WW signal regions.

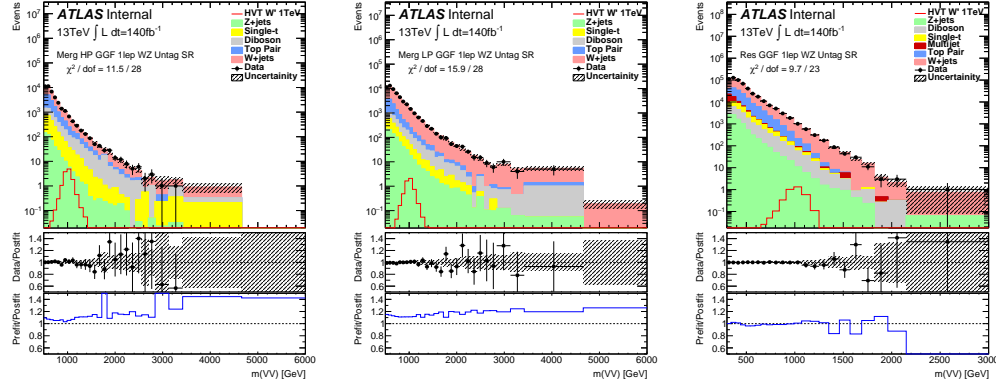


Figure 11.14: This figure shows the distribution of $m_{\ell\nu qq}$ in the GGF WZ Untag signal regions.

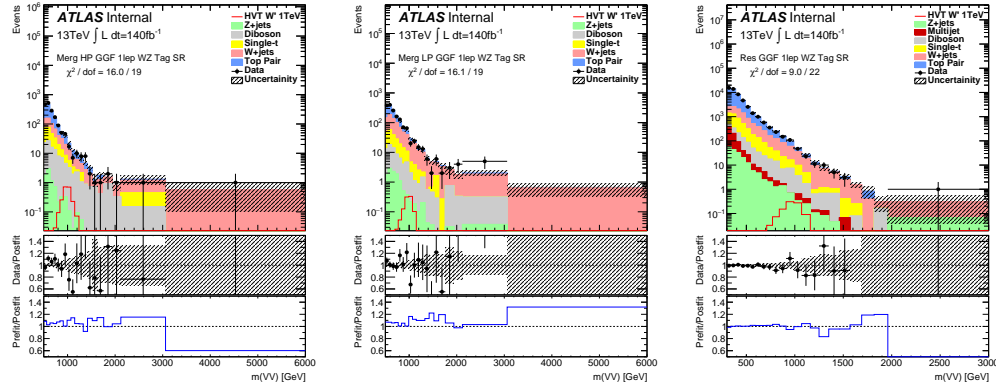


Figure 11.15: This figure shows the distribution of $m_{\ell\nu qq}$ in the GGF WZ Tag signal regions.

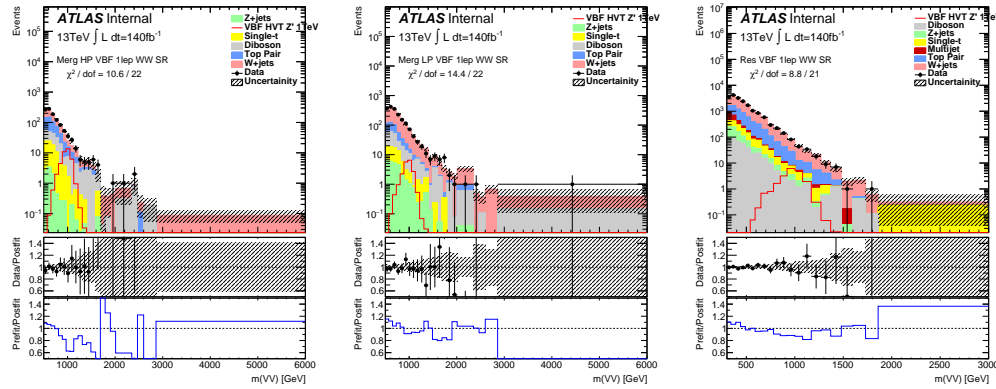


Figure 11.16: This figure shows the distribution of $m_{\ell\nu qq}$ in the VBF WZ Tag signal regions.

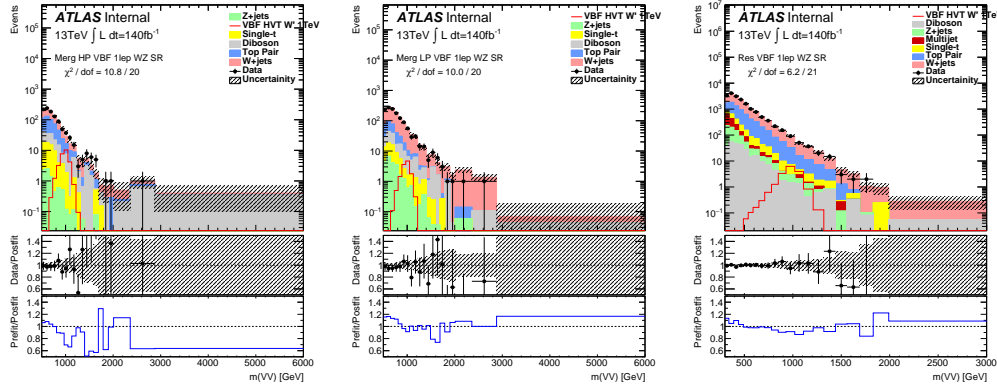


Figure 11.17: This figure shows the distribution of $m_{\ell\nu qq}$ in the VBF WZ Tag signal regions.

1248 11.4 Limits

1249 Using the exclusion limits tests discussed previously, exclusion limits are set
 1250 on μ and consequently cross-sections for different signal models. Exclusion limits
 1251 for the models considered are shown in Figure 11.18 - 11.20. These limits exclude
 1252 HVT Model A $W' < 3.4$ TeV and $Z' < 3.3$ TeV and Model B $W' < 3.7$ TeV and
 1253 $Z' < 3.7$ TeV. Randall Sundrum Gravitons are excluded for masses below 1.6 TeV .

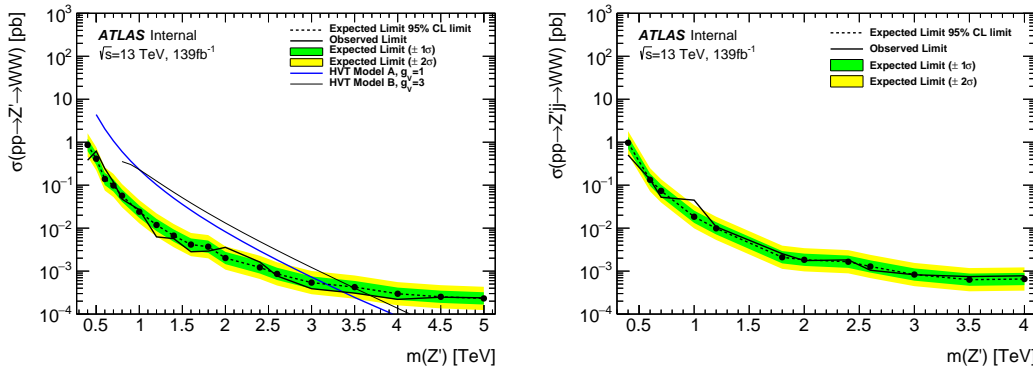


Figure 11.18: This figure shows theory, expected and observed limits for HVT W' DY (left) and VBF (right) production.

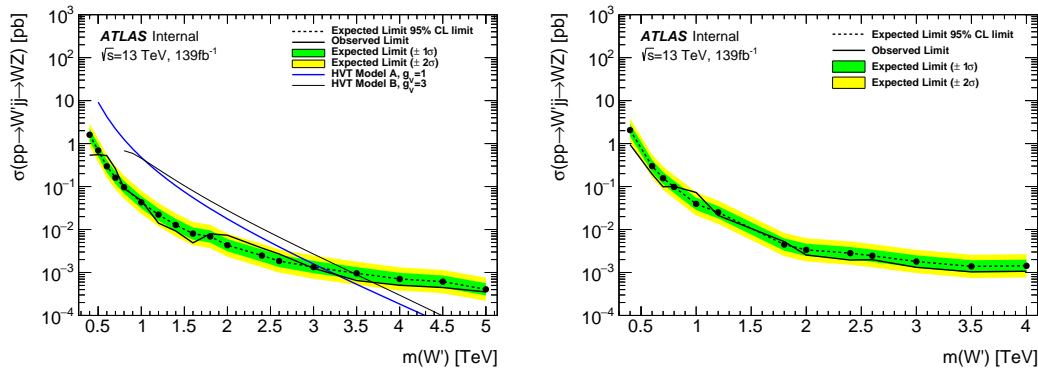


Figure 11.19: This figure shows theory, expected and observed limits for HVT Z' DY (left) and VBF (right) production.

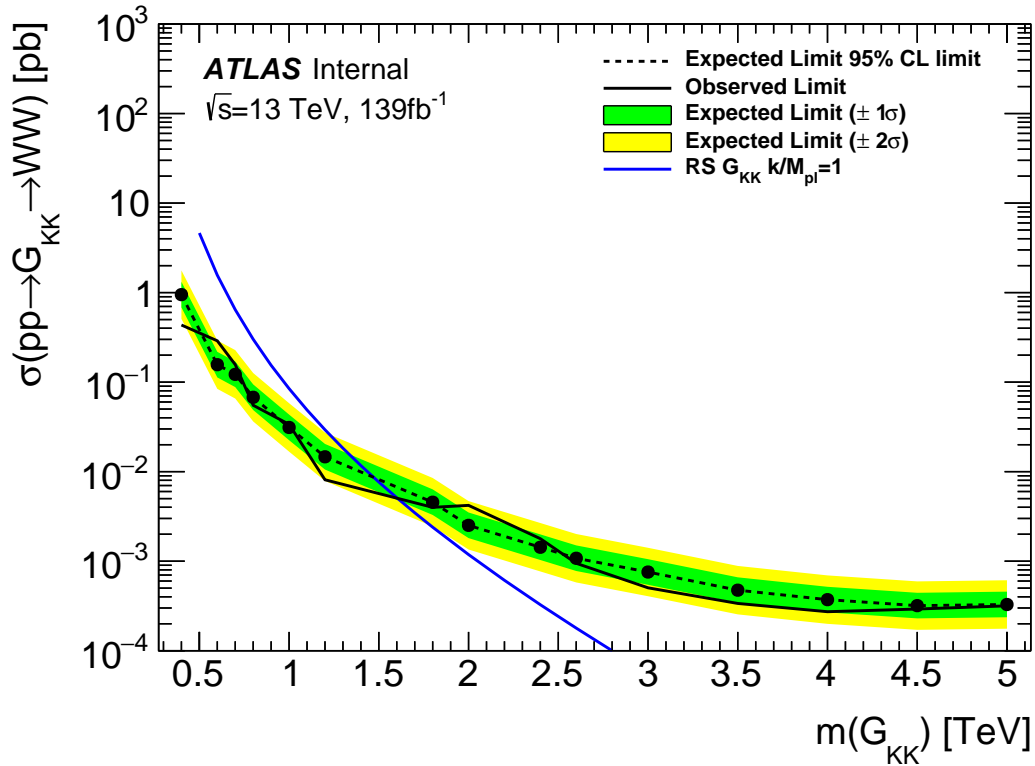


Figure 11.20: This figure shows theory, expected and observed limits for RS Gravitons via DY production.

1254

Part V

1255

Quark and Gluon Tagging

₁₂₅₆ **Chapter 12**

₁₂₅₇ **Prospects**

₁₂₅₈ For the resolved analysis, signal jets are quark enriched and background jets are
₁₂₅₉ gluon dominated. By classifying jets in the event as quark or gluon initiated, less
₁₂₆₀ background would contaminate the signal region. Figure 12.1 shows the PDGID
₁₂₆₁ for the truth parton matched to the jet (meaning the highest energy parton in
₁₂₆₂ the jet catchment area) in events passing the resolved signal region selections.
₁₂₆₃ PDGID = -1 corresponds to pileup jets, $0 < \text{PDGID} < 6$ correspond to quarks
₁₂₆₄ and $\text{PDGID} = 21$ corresponds to gluons. From this Figure, it is evident that a
₁₂₆₅ notable fraction of the background that contaminates the signal region contains
₁₂₆₆ gluon jets, especially for the sub-leading jet.

₁₂₆₇ As gluons jets have more constituents and therefore more tracks (n_{trk}), the
₁₂₆₈ background jets have more tracks than the signal jets. This is shown in Fig-
₁₂₆₉ ure 12.2. Therefore, by cutting on the number of tracks in a jet, quark and gluon
₁₂₇₀ jets may be distinguished (i.e. jets with less than a given number of tracks are
₁₂₇₁ classified as a quark, otherwise the jet is classified as a gluon.) Moreover, as the
₁₂₇₂ momentum of the jet increases the number of tracks also increases logarithmically
₁₂₇₃ [Cite nachman thesis Natasha]. Therefore by applying a cut on the number of
₁₂₇₄ tracks that scales with the $\ln(p_T)$ is more powerful than a threshold cut on the

1275 number of tracks. Figure 12.3-Figure 12.6 show normalized heat maps of $\ln(p_T)$
1276 vs the number of reconstructed tracks for the background and a 300 GeV Z' signal.
1277 In these plots it is evident that the number of tracks in the background jets grows
1278 more quickly with $\ln(p_T)$ than for the signal jets. This is expected given that the
1279 signal is quark dominated and the background is gluon dominated.

1280 In Figure 12.8 is the ROC Curve for quark gluon tagging with cut on the
1281 number of tracks in a jet that depends on $\ln(p_T)$. The sum of the backgrounds in
1282 the signal region were used for this curve. Here the quark tagging efficiency is the
1283 ratio of quarks tagged as quarks to the total number of quarks in the signal region.
1284 The gluon rejection is calculated as the reciprocal of the gluon tagging efficiency.
1285 Choosing a 90% efficient working point with a rejection of 1.4 corresponds to a
1286 slope of 4 and intercept of -5. Tagging both jets in this analysis would yield an
1287 efficiency of $90\%^{n_{jets}}$. Focusing on the background in Figure 12.9, this cut helps
1288 minimize gluon contamination in the signal region. Also, from these heat maps it
1289 is obvious that the number of tracks in gluon jets grows more quickly than those
1290 in quark jets.

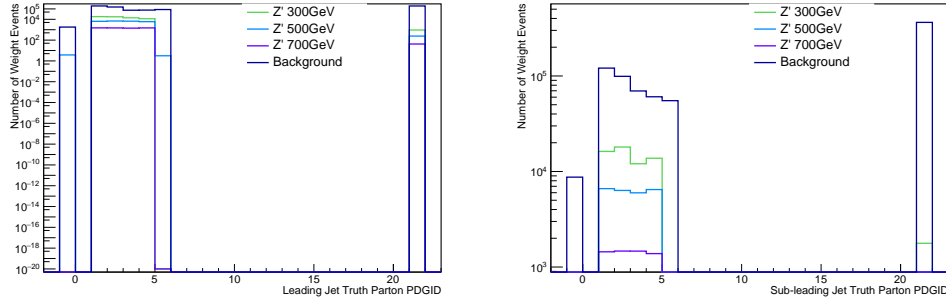


Figure 12.1: PDGID of the truth-level parton matched to the small-R jets passing the Resolved GGF WW Signal Region selections for the (a) Leading (b) Sub-Leading jets . These distributions are shown for 300, 500, and 700GeV Z' signals and the background.

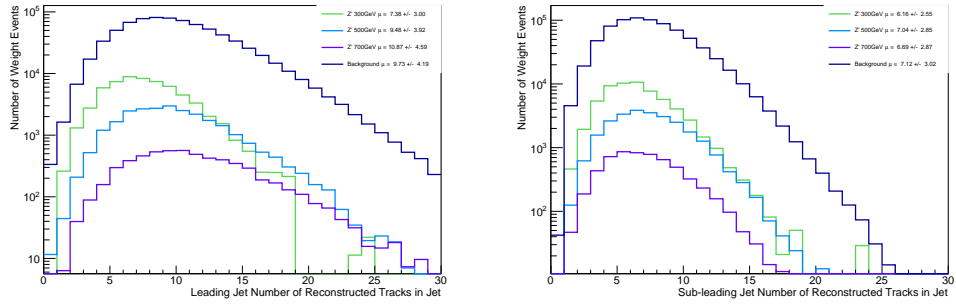


Figure 12.2: The number of tracks in small-R jets in events passing the Resolved GGF WW Signal Region selections for the (a) Leading (b) Sub-Leading jets. These distributions are shown for 300, 500, and 700GeV Z' signals and the background.

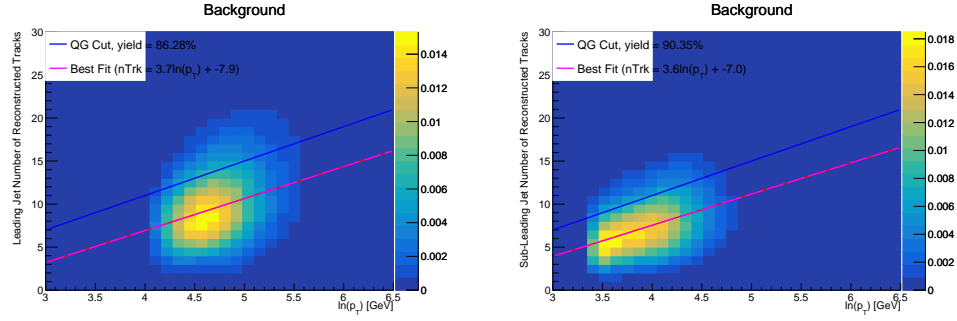


Figure 12.3: The number of tracks in background small-R jets in events passing the Resolved GGF WW Signal region selection vs. $\ln(p_T)$ for (a)Leading (b) Sub-Leading jets. The best fit line for the distribution is also shown, as well as the percentage of jets that pass a cut of number of tracks $< 4 \times \ln(p_T) - 5$. Note the number of total entries in these plots has been normalized to one.

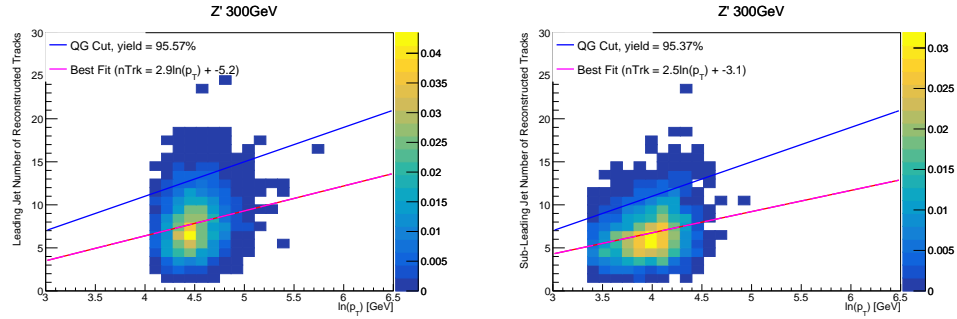


Figure 12.4: The number of tracks in small-R jets in 300GeV Z' events passing the Resolved GGF WW Signal region selection vs. $\ln(p_T)$ for (a)Leading (b) Sub-Leading jets. The best fit line for the distribution is also shown, as well as the percentage of jets that pass a cut of number of tracks $< 4 \times \ln(p_T) - 5$. Note the number of total entries in these plots has been normalized to one.

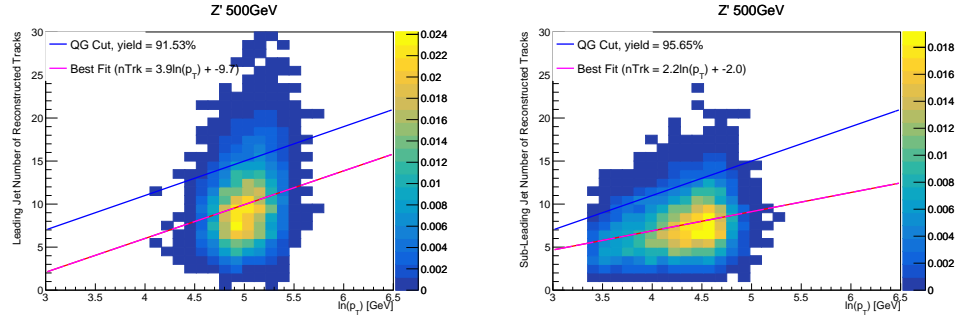


Figure 12.5: The number of tracks in small-R jets in 500GeV Z' events passing the Resolved GGF WW Signal region selection vs. $\ln(p_T)$ for (a)Leading (b) Sub-Leading jets. The best fit line for the distribution is also shown, as well as the percentage of jets that pass a cut of number of tracks $< 4 \times \ln(p_T) - 5$. Note the number of total entries in these plots has been normalized to one.

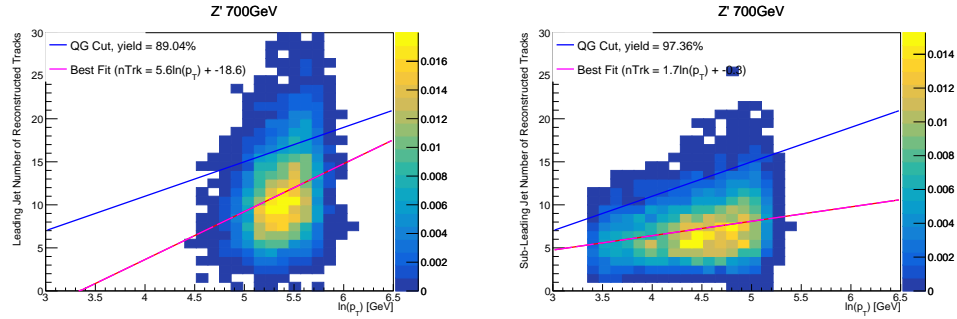


Figure 12.6: The number of tracks in small-R jets in 700GeV Z' events passing the Resolved GGF WW Signal region selection vs. $\ln(p_T)$ for (a)Leading (b) Sub-Leading jets. The best fit line for the distribution is also shown, as well as the percentage of jets that pass a cut of number of tracks $< 4 \times \ln(p_T) - 5$. Note the number of total entries in these plots has been normalized to one.

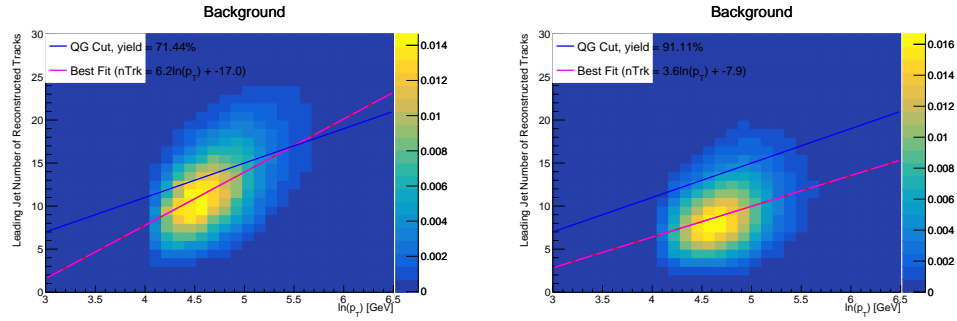


Figure 12.7: The number of tracks in leading small-R jets in background events passing the Resolved GGF WW Signal region selection vs. $\ln(p_T)$ for (a)Gluons (b) Quarks jets. The best fit line for the distribution is also shown, as well as the percentage of jets that pass a cut of number of tracks $< 4 \times \ln(p_T) - 5$.Note the number of total entries in these plots has been normalized to one.

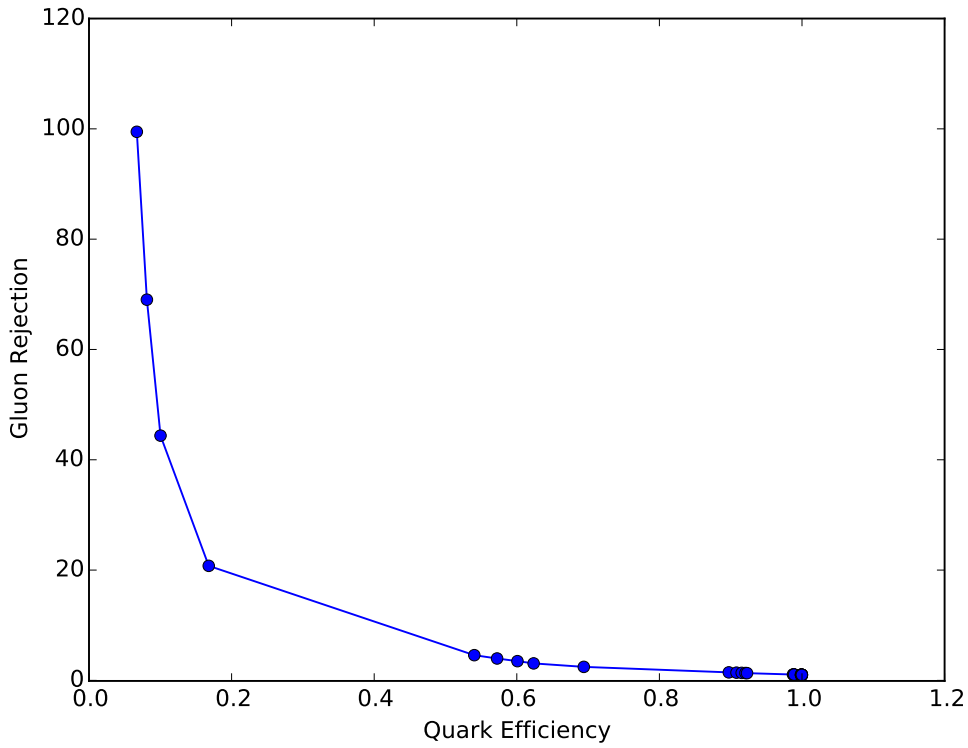


Figure 12.8: ROC Curve for Quark and Gluon Tagging with a cut on the number of tracks that depends on the $\ln(p_T)$.

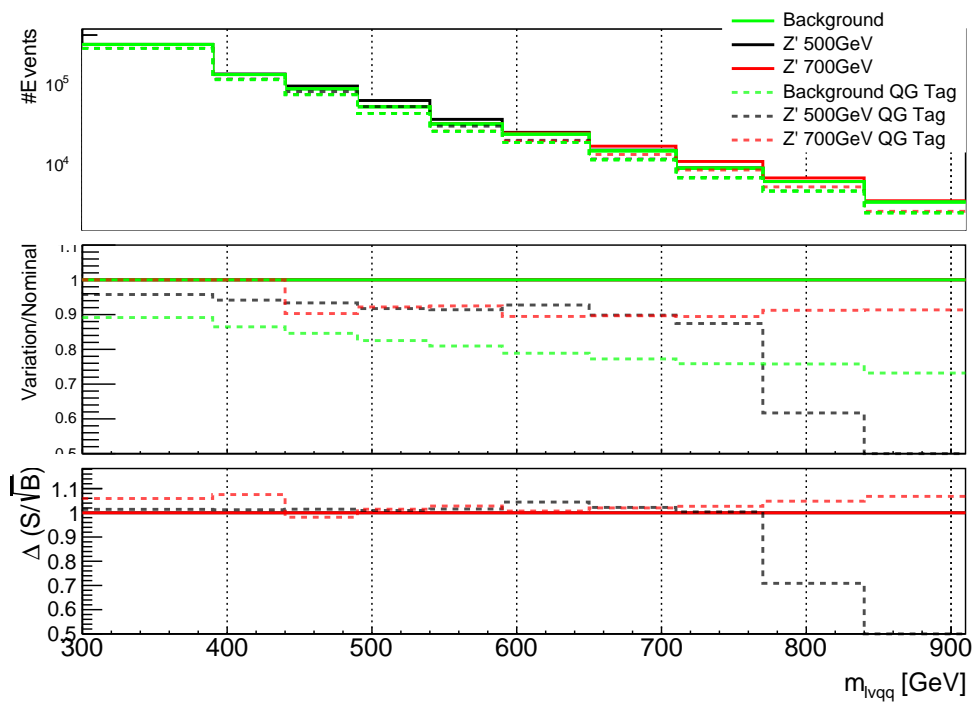


Figure 12.9: The top panel shows the distribution of m_{lvqq} with and without quark gluon tagging. The middle panel shows the ratio of the signals and backgrounds with and without quark gluon tagging. The bottom panel shows the change in S/\sqrt{B} with quark gluon tagging.

1291 Chapter 13

1292 n_{trk} Calibration

1293 As tagger based on nTrk cuts on the number of tracks in jets, a quantity that
1294 is not known with infinite precision, means that relevant systematic uncertainties
1295 must be evaluated. The sources of uncertainty in n_{trk} may be split into modeling
1296 and experimental uncertainties.

1297 Modeling uncertainties are obtained by assessing PDF and ME uncertainties
1298 on the number of charged particles in particle-level jets in dijet events. The
1299 number of charged particles as a function of jet p_T is calculated using an Iterative
1300 Bayesian (IB) technique [cite paper].

1301 This measurement ([8]) uses the ATLAS 2012 pp collision dataset, correspond-
1302 ing to $20.3/\text{fb}$ at center-of-mass energy $\sqrt{s} = 8\text{TeV}$. The number of charged con-
1303 stituents depends on fragmentation modeling and matrix elements, which do not
1304 depend on s . For this reason, it is safe to use these uncertainties for $\text{sqrt}(s)=13\text{TeV}$.
1305 Monte Carlo (MC) samples are used to determine the response matrix. The MC
1306 sample is a dijet sample generated with Pythia 8.175 using CT10 PDF and AU2
1307 tune. The anti- k_T algorithm is used to cluster jets with a radius parameter R
1308 $= 0.4$. Jets are required to have $|\eta| < 2.1$. Tracks in jets are required to have
1309 $p_T > 500\text{MeV}$, $|\eta| < 2.5$, track-fit $\chi^2 < 3.0$ and originate from the primary ver-

tex. Matching tracks to jets is accomplished using ghost-association [cite]. In this technique, jets are re-clustered with the track collection augmented with "ghost" versions of tracks. These "ghosts" tracks have the same direction as their parent track, but infinitesimal track p_T . This insures meta-jet properties (e.g. η , p_T , etc) are unchanged. A track is matched to a jet if it's ghost version remains in the jet after re-clustering. Further details of the data, object, and event selection may be found in [cite 35].

To select dijet topologies events are required to have at least two jets with $p_T > 50GeV$ that are relatively well-balanced ($p_T^{lead}/p_T^{sub-lead} < 1.5$).

In the IB technique, the prior distribution and number of iterations are the inputs [cite Bayesian paper]. The IB response matrix connects number of charged particles to the number of tracks in jets determined using the simulated samples. This response matrix is used to unfold data to extract the n_c . Before applying the response matrix a fake factor is applied. This accounts for jets that pass detector level selections, but not particle level selections. Following this, the IB method iteratively applies the response matrix using the nominal Pythia 8.175 sample as a prior. The number of IB iterations is chosen to minimize unfolding bias and statistical fluctuations. For this measurement four iterations was found to be optimal by minimizing the unfolding bias from pseudodata simulated with Herwig++ with a prior from Pythia 8 AU2. Finally, the inefficiency factor is applied to account for events passing particle level selection but not detector level, yielding the unfolded nCharged distribution.

This process is prone to three main sources of bias: response matrix, correction factor, and unfolding procedure uncertainties. The response matrix is sensitive to experimental uncertainties impacting jet track reconstruction and calorimeter jet p_T . Correction factors are also sensitive to experimental uncertainties (e.g. JES)

1336 as such uncertainties modify detector level acceptance. Sensitivity to particle
 1337 level acceptance is calculated by comparing Pythia and Herwig. Finally, the bias
 1338 from the IB prior choice is determined by reweighting the particle-level spectrum,
 1339 so the simulated detector level spectrum more closely matches the uncorrected
 1340 data. Unfolding this modified detector-level simulation and comparing it to the re-
 1341 weighted particle-level spectrum indicates bias from the prior distribution choice.
 1342

1343 A summary of all the systematic uncertainties associated with this unfolding
 1344 may be found in [ref paper]. Total uncertainties are < 7% for the number of
 1345 charged particles in jets. The unfolded distribution of the nCharged in jets from
 1346 data are further analyzed to extract the quark and gluon nCharged distributions.
 1347 In dijet events, the jet with a larger η is more energetic and therefore more likely
 1348 to be a quark. This is due to the quarks in protons generally having a larger
 1349 fraction of the total momentum of the proton constituents. The more central jet
 1350 is more likely to be a gluon-initiated jet. This correlation between jet η and flavor
 may then be used to extract nCharged in p_T bins using:
 1351

$$\langle n_c^f \rangle = f_q^f \langle n_c^q \rangle + f_g^f \langle n_c^g \rangle \quad (13.1)$$

$$\langle n_c^c \rangle = f_q^c \langle n_c^q \rangle + f_g^c \langle n_c^g \rangle \quad (13.2)$$

1352 In this equation the f and c subscripts denote the more forward and central
 1353 jets, respectively. The q and g subscripts denote quark and gluon. The fraction
 1354 of more forward jets that are say gluons is denoted by f_g^f . The other relevant jet
 1355 fractions are denoted with the same naming scheme. Finally, $\langle n_c \rangle$ is the average
 1356 number of charged particles in a jet in a given p_T bin. To show that Eq. (??) may
 1357 be used to extract quark and gluon n_c distributions the extracted distributions
 1358 are compared to n_c distributions determined using the jet flavor in simulation.
 1359 Figure [add figure natasha] shows that the extracted and true distributions differ

1360 by < 1% over the p_T range probed for this study. Moreover, this implies that n_c
1361 depends only on the flavor of the initiating parton and jet p_T .

1362 These extracted distributions are prone to PDF and ME biases. The bias from
1363 the choice of the CT10 PDF for the Pythia sample is accounted for by comparing
1364 quark/gluon fractions for the nominal CT10 sample with its eigenvector variations.
1365 Comparing the quark/gluon fractions from Pythia 8 and Herwig++ quantify the
1366 uncertainty from the ME calculation. These uncertainties are added in quadra-
1367 ture with the unfolding uncertainty to give the total modelling uncertainty on
1368 the extracted n_c distribution. This is shown in Figure 14.2.

1369 To apply these uncertainties in n_c distributions in data, per-jet event weights
1370 are associated with each uncertainty according to:

$$w_i(n_c) = \frac{P(n_c | n_c > \pm \sigma_{n_c}^i)}{P(n_c | n_c >)} \quad (13.3)$$

1371 In Eq. (??), i denotes the uncertainty considered, P is the Poisson probability,
1372 and $\sigma_{n_c}^i$ represents the average impact of the uncertainty on n_c .

1373 The previous uncertainties described accounted for modeling uncertainty as-
1374 sociated with the number of charged particles in a jet. However, n_c is not a
1375 measurable quantity. Instead the number of tracks in a jet is measured, which is
1376 a proxy for n_c . Therefore the uncertainties associated with the measurement of
1377 nTracks must also be considered ([10]). These uncertainties were calculated using
1378 a Pythia 8 dijet sample with NNPDF 23 and Run 2 data. Track reconstruction
1379 efficiency and fake rates are the dominant sources of nTrack uncertainties.

1380 The track reconstruction efficiency is affected by the uncertainty of the de-
1381 scription of the ID material in simulation and the modeling of charged-particle
1382 interactions with this material. These uncertainties are accounted for by varying
1383 the ID material by 5-25% (dependent on the region of the detector considered).

1384 The difference in the tracking efficiency between the nominal and varied simula-
1385 tion give the uncertainty on the track reconstruction efficiency. Another important
1386 source of track reconstruction inefficiency arises in the core of jets. The high den-
1387 sity of tracks in the jet cores can cause ID clusters to merge. The fraction of lost
1388 tracks due to merging is given by the fraction of tracks that have a charge of two
1389 minimum ionizing particles. This quantity is compared between data and simu-
1390 lation resulting in an uncertainty of 0.4% on tracks with $\Delta R < 0.1$. Combining
1391 these effects gives a total uncertainty as a function of p_T and η that is generally
1392 $< 2\%$ [references figure 44 from [10]).

1393 Fake tracks are the other dominant source of nTrk uncertainty. Fake tracks
1394 are tracks that cannot be associated to a single particle. Often these tracks are a
1395 result of random combinations of hits from charged particles that overlap in space.
1396 In dense environments, such as the core of jets or high-pileup environments, fake
1397 tracks are more likely. Fake tracks are estimated with a 'control region method'
1398 which is briefly summarized here [[9]]. By applying a series of track selections
1399 to enrich the fraction of fake tracks (e.g. $|d_0| > 0.1$, track $\chi^2 > 1.4$, etc) in
1400 simulation, templates for fake track parameters are calculated. These templates
1401 are then fit to data to determine the fraction of fake tracks. On average the fake
1402 rate is found to be 30% (independent of p_T and η).

1403 To assess the impact of these two detector level uncertainties, tracks are ran-
1404 domly dropped according to the rates described above. Reconstruction and fake
1405 uncertainties both lower the number of tracks, hence these uncertainties are one-
1406 sided. By dropping tracks in this way a varied nTrk distribution is calculated for
1407 both uncertainties. The associated per-jet event weights are then calculated in
1408 the same way as the modeling weights as:

$$w_i(n_c) = \frac{P(n_{trk} | < n_{trk} > \pm \sigma_{n_{trk}}^i)}{P(n_{trk} | < n_{trk} >)} \quad (13.4)$$

1409 Adding the modeling and detector level uncertainties in quadrature gives the
 1410 overall nTrack uncertainty. The effects of the individual uncertainties on the nTrk
 1411 distributions can be seen in Fig 14.4. Fig 14.3 shows the m_{lvqq} and nTrk distri-
 1412 butions for the W and Top control regions before likelihood fitting. In these plots
 1413 the nTrk uncertainties improve agreement between data and MC. The remaining
 1414 differences are likely covered by likelihood fitting and improving the analysis itself.

¹⁴¹⁵ **Chapter 14**

¹⁴¹⁶ **Application**

¹⁴¹⁷ Using the 90% WP of the n_{trk} tagger improves S/\sqrt{B} is $\sim 3\%$ as shown in
¹⁴¹⁸ Figure 12.9. Although, n_{trk} is the single most powerful discriminating variable
¹⁴¹⁹ for quark and gluon jets, the addition of other jet variables would improve the
¹⁴²⁰ classification efficiency. Figure 14.1 shows the possible improvement of 10%
¹⁴²¹ in jet classification using the truth label of the jets to classify jets. This type of
¹⁴²² improvement is possible by using variables such as jet width, and energy correlata-
¹⁴²³ tors. Figure [add BDT figure/use 1612.01551.pdf] shows for a 90% quark tagging
¹⁴²⁴ efficiency for a 100 GeV jet, a BDT improve the gluon rejection by 0.4. Once this
¹⁴²⁵ tagger is calibrated it would improve the analysis sensitivity of this channel.

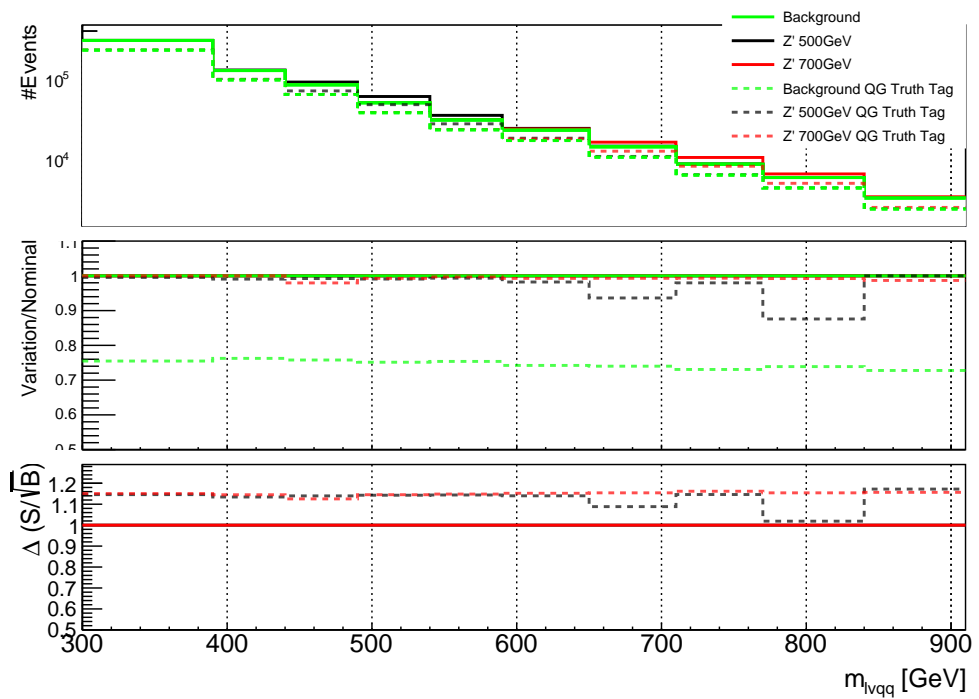


Figure 14.1: The top panel shows the distribution of m_{lvqq} with and without requiring jets to be true quarks. The middle panel shows the ratio of the signals and backgrounds with and without requiring jets to be true quarks. The bottom panel shows the change in S/\sqrt{B} when requiring jets to be true quarks..

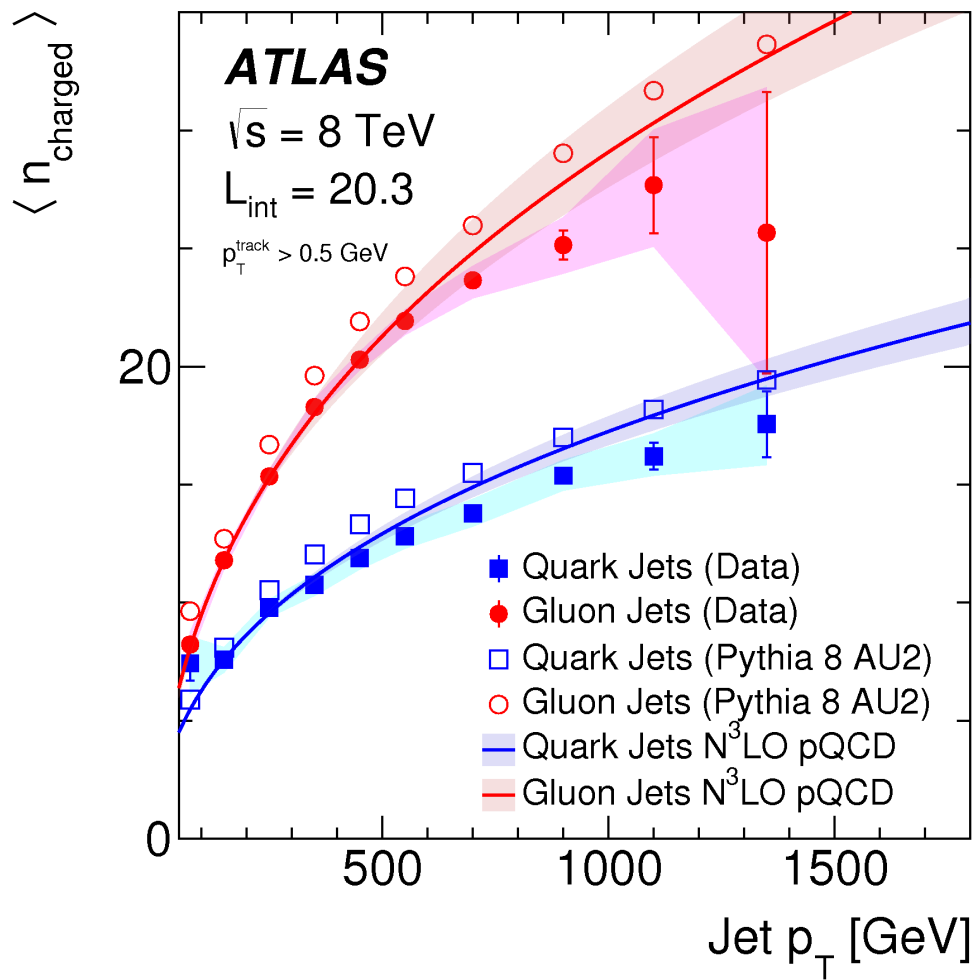


Figure 14.2: Unfolded and extracted n_C qg dstbs..

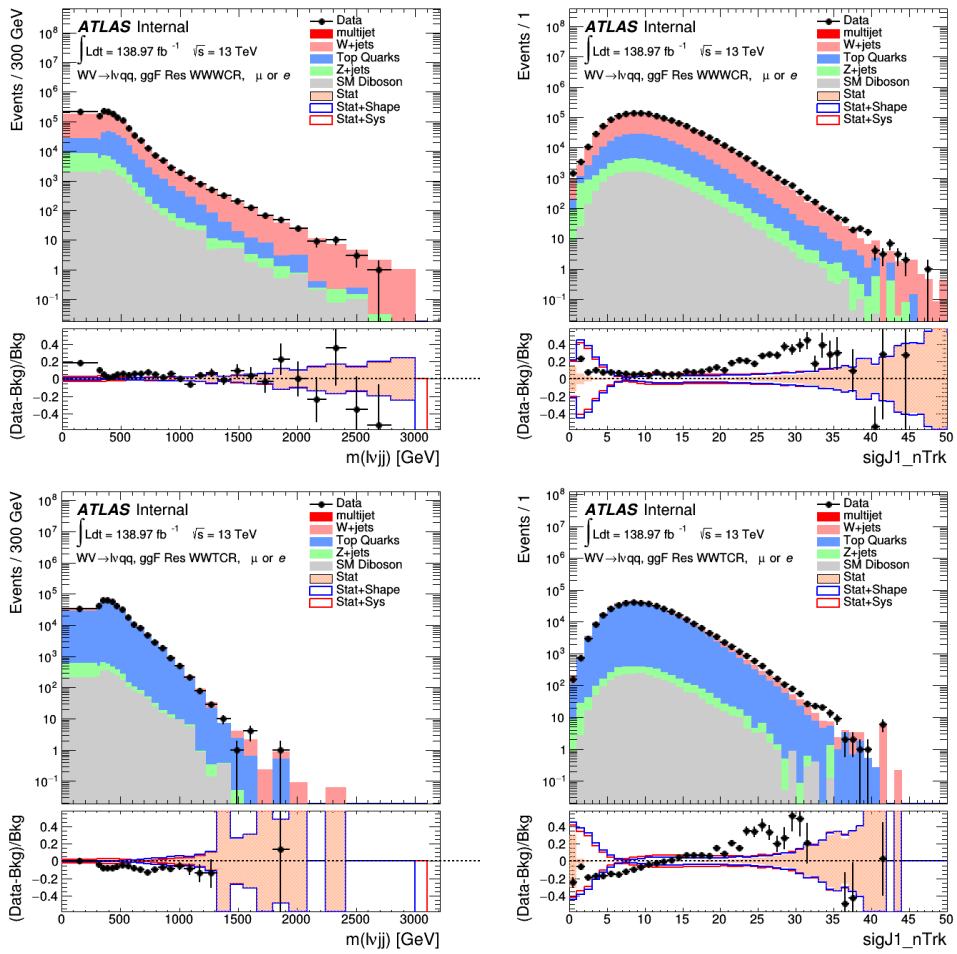


Figure 14.3: PDGID of the truth-level parton matched to the small-R jets passing the Resolved GGF WW Signal Region selections for the (a) Leading (b) Sub-Leading jets . These distributions are shown for 300, 500, and 700GeV Z' signals and the background.

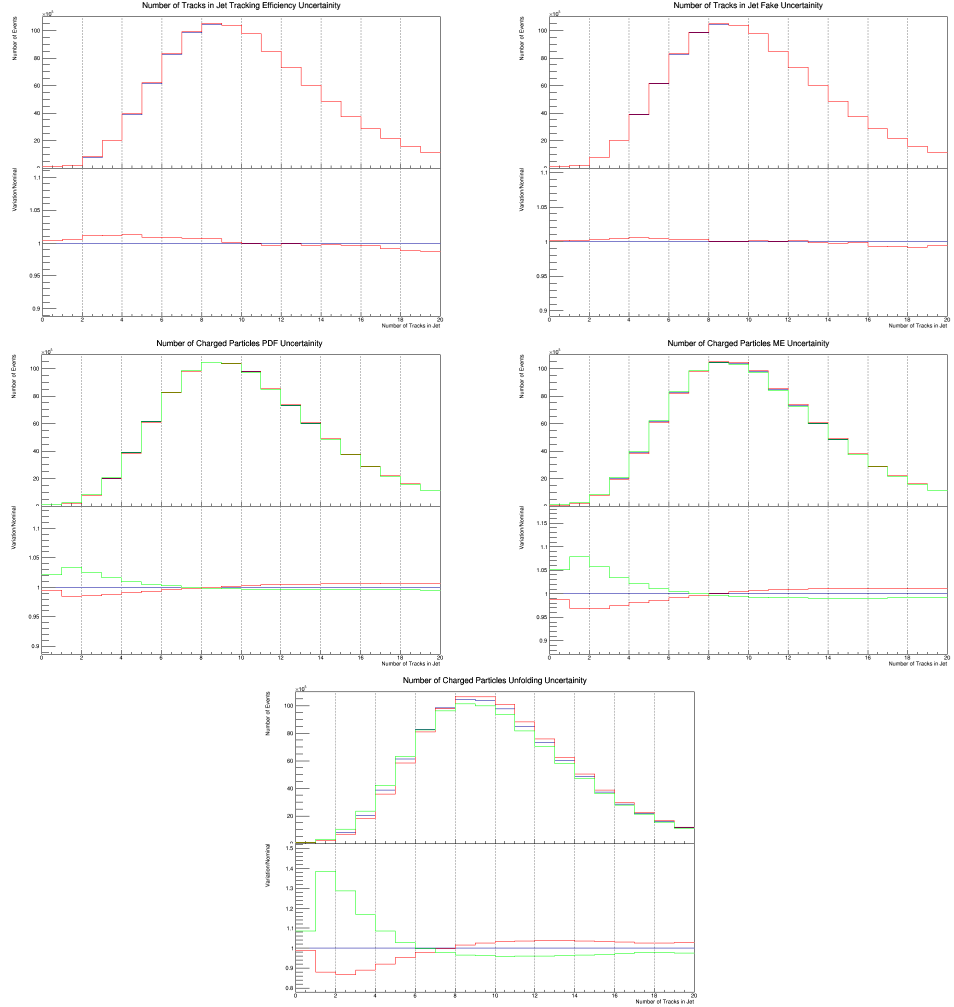


Figure 14.4: These figures show the impact of the uncertainties on the number of tracks in the leading jet in the sum of the background sample in the Resolved GGF WW SR (a) tracking efficiency (b) fake (c) PDF (d) ME (e) unfolding uncertainties.

Part VI

1426

Conclusion

1427

1428 **Chapter 15**

1429 **Conclusions**

1430 A search for WW and WZ diboson resonance production in $\ell\nu qq$ final states
1431 was performed using 139fb^{-1} of pp collision data collected at a center-of-mass
1432 energy of $\sqrt{s} = 13\text{TeV}$ by that ATLAS detector at the LHC between 2015 and
1433 2018. No excess of events above the background-only expectation was observed.
1434 The largest local excess is approximately 2.7σ , which is not significant. Limits
1435 on the production cross section are obtained for the HVT W' and Z' and RS
1436 Gravitons. Signal masses below 3.4 (3.7) TeV are excluded for HVT W' Model
1437 A(B). Signal masses below 3.3 (3.7) TeV are excluded for HVT Z' Model A(B).
1438 Randall Sundrum Gravitons are excluded for masses below 1.6 TeV. Going forward,
1439 improving the classification of jets in events would improve analysis sensitivity.
1440 To distinguish quark from gluon jets a jet tagger based on the number of tracks in
1441 jets is studied in the context of this search. Finally, the calibration of the number
1442 of tracks in jets is discussed.

¹⁴⁴³ Bibliography

- ¹⁴⁴⁴ [1] Lecture notes particle physics ii.
- ¹⁴⁴⁵ [2] Kaustubh Agashe, Hooman Davoudiasl, Gilad Perez, and Amarjit Soni.
¹⁴⁴⁶ Warped Gravitons at the LHC and Beyond. *Phys. Rev.*, D76:036006, 2007.
- ¹⁴⁴⁷ [3] G. Altarelli and G. Parisi. Asymptotic freedom in parton language. *Nuclear Physics B*, 126(2):298 – 318, 1977.
- ¹⁴⁴⁸
- ¹⁴⁴⁹ [4] ATLAS Collaboration. Atlas muon reconstruction performance in lhc run 2.
- ¹⁴⁵⁰ [5] ATLAS Collaboration. Summary plots from the atlas standard model physics
¹⁴⁵¹ group.
- ¹⁴⁵² [6] ATLAS Collaboration. Tagging and suppression of pileup jets with the atlas
¹⁴⁵³ detector.
- ¹⁴⁵⁴ [7] ATLAS Collaboration. Jet energy scale measurements and their systematic
¹⁴⁵⁵ uncer- tainties in proton–proton collisions at $\sqrt{s} = 13$ tev with the atlas
¹⁴⁵⁶ detector. arXiv: 1703.09665 [hep-ex].
- ¹⁴⁵⁷ [8] ATLAS Collaboration. Measurement of the charged-particle multiplicity
¹⁴⁵⁸ inside jets from $s=\sqrt{8}$ tev pp collisions with the atlas detector.
¹⁴⁵⁹ arXiv:1602.00988 [hep-ex].
- ¹⁴⁶⁰ [9] ATLAS Collaboration. Performance of the atlas track reconstruction algo-
¹⁴⁶¹ rithms in dense environments in lhc run 2. arXiv:1704.07983 [hep-ex].
- ¹⁴⁶² [10] ATLAS Collaboration. Properties of jet fragmentation using charged par-
¹⁴⁶³ ticles measured with the atlas detector in pp collisions at $\sqrt{s} = 13$ tev.
¹⁴⁶⁴ arXiv:1906.09254 [hep-ex].
- ¹⁴⁶⁵ [11] Alex Dias and V. Pleitez. Grand unification and proton stability near the
¹⁴⁶⁶ peccei-quinn scale. *Physical Review D*, 70, 07 2004.
- ¹⁴⁶⁷ [12] Stefan Höche, Frank Krauss, Marek Schönherr, and Frank Siegert. Qcd ma-
¹⁴⁶⁸ trix elements + parton showers. the nlo case. *Journal of High Energy Physics*,
¹⁴⁶⁹ 2013(4), Apr 2013.

- 1470 [13] David Krohn, Jesse Thaler, and Lian-Tao Wang. Jets with variable r. *Journal*
1471 *of High Energy Physics*, 2009(06):059–059, Jun 2009.
- 1472 [14] Gregory Soyez Matteo Cacciari, Gavin P. Salam. The anti- k_T jet clustering
1473 algorithm. arXiv:0802.1189 [hep-ph].
- 1474 [15] Duccio Pappadopulo, Andrea Thamm, Riccardo Torre, and Andrea Wulzer.
1475 Heavy vector triplets: bridging theory and data. *Journal of High Energy*
1476 *Physics*, 2014(9), Sep 2014.
- 1477 [16] Antonio Pich. The Standard Model of Electroweak Interactions. In *Proceedings, High-energy Physics. Proceedings, 18th European School (ESHEP 2010): Raseborg, Finland, June 20 - July 3, 2010*, pages 1–50, 2012. [,1(2012)].
- 1480 [17] Lisa Randall and Raman Sundrum. A Large mass hierarchy from a small
1481 extra dimension. *Phys. Rev. Lett.*, 83:3370–3373, 1999.
- 1482 [18] Tania Robens and Tim Stefaniak. Lhc benchmark scenarios for the real higgs
1483 singlet extension of the standard model. *The European Physical Journal C*,
1484 76(5), May 2016.
- 1485 [19] Alex Sherstinsky. Fundamentals of recurrent neural network (RNN) and long
1486 short-term memory (LSTM) network. *CoRR*, abs/1808.03314, 2018.